

Investigating Kinesin-based Mitotic Spindle Assembly Backup Mechanisms Using Single
Molecule Methods

By

Dana Nicole Reinemann

Dissertation

Submitted to the Faculty of the
Graduate School of Vanderbilt University
in partial fulfillment of the requirements

for the degree of

DOCTOR OF PHILOSOPHY

in

Chemical Engineering

May 11, 2018

Nashville, Tennessee

Approved:

Matthew J. Lang, Ph.D.

G. Kane Jennings, Ph.D.

Rizia Bardhan, Ph.D.

Ryoma Ohi, Ph.D.

To my son, Will, for being the ray of sunshine I needed throughout this process.

ACKNOWLEDGMENTS

Obtaining a Ph.D. has been quite a journey over the last five years. There have certainly been ups and downs along the way, but I am a stronger person and scientist because of them. I could not have completed such a task without support from the following people.

First of all, I would like to thank my advisor, Matt Lang, for being an example of a great scientist, as well as a great person. Not only have I had the opportunity to work on exciting projects, but he has pushed and challenged me along the way to become the scientist I am today. Also, I very much appreciate his understanding regarding work-family balance. Raising a young son on my own has had its challenges, especially when school was out or he was sick. Knowing that I could take care of my family without stressing about work has been a Godsend, and I am truly grateful.

I would also like to thank the rest of my Ph.D. committee: Rizia Bardhan, Kane Jennings, and Puck Ohi. Thank you for your advice and insight over the years. Puck, collaborating with your lab has been such a great opportunity. Not only have I learned more biology than I ever thought I would and worked on fulfilling projects, but I have gained a mentor and friend.

I have worked with some amazing individuals while in the Lang lab. Thank you Yongdae, Dev, and JC for teaching me the foundational knowledge I needed to get my projects off the ground. Thank you Harris, Andy, and Mark for being great friends and a source of support throughout the years. Sonia, thank you for your help, support, and friendship while in Nashville. I would also like to thank the undergrads and rotation students I have had the opportunity to work with in the lab: Dan, Charles, Sophie, Zane, Nikki, and Jason. I enjoyed working with you all, and you were a great help on various projects.

To the ChBE staff: Mark, Mary, Rae, Julie, Angie, Felisha, and Brandon, thank you for all that you do for this department. Your help with orders, trips, getting paid, and just being a source of encouragement have been greatly appreciated.

I have made some lifelong ChBE friends over the last five years. Lara, Anne, Sonia, Holly, Ali, and May, you all have been such a great source of support. Thank for all of the talks, lunches, girls' nights, and just being an outlet to blow off steam in general. Also, thank you for the many times you would babysit Will for me. I cannot express how helpful you guys have been!

I would also like to thank Westwood Baptist Church in Nashville and Pilgrims Rest Baptist Church back home for being sources of guidance and encouragement throughout this process. Westwood has taken my son and me in as one of their own, and their friendship has been invaluable.

I could not have completed this process without my family and friends back home. Dad, thank you for your strong example, and I wish you were here to see this accomplishment. Mom, Kelley, Waylon, Ava, David, and Jewell, thank you for being an unwavering source of support and prayers. Annah, Andrea, Elizabeth, and Jenny, thank you for always being there. To the love of my life, Tim, thank you for constantly reminding me to have faith and for your love and support. Last, but certainly not least, I would like to thank my Will Bennett. Many wondered how I would live on my own with him, support him, love him, and still be successful at pursuing at Ph.D. On the contrary, I could not have done it without him. He has been my light in some pretty dark times. He was also a reason to step away from the stress of work and focus on playing trains or snuggling while watching Cars or Thomas for the millionth time. Thank you, buddy!

TABLE OF CONTENTS

	Page
DEDICATION	ii
ACKNOWLEDGMENTS	iii
LIST OF TABLES	vii
LIST OF FIGURES	viii
Chapter	
1. INTRODUCTION	1
1.1. Cancer and the Cell Cycle	1
1.2. The Mitotic Spindle	3
1.3. Biological Motors	5
1.4. Spindle Assembly by Motor Proteins	7
1.5. Single Molecule Methods	12
1.6. Bibliography	17
2. COLLECTIVE FORCE REGULATION IN ANTI-PARALLEL MICROTUBULE GLIDING BY DIMERIC KIF15 KINESIN MOTORS	26
2.1. Summary	26
2.2. Introduction	27
2.3. Results	29
2.4. Discussion	44
2.5. Materials and Methods	48
2.6. Acknowledgements	58
2.7. Bibliography	59
3. THE COVER-NECK BUNDLE OF KIF15: A THERAPEUTIC TARGET	65
3.1. Summary	65
3.2. Introduction	65
3.3. Materials and Methods	68
3.4. Results and Discussion	70
3.5. Acknowledgements	72
3.6. Bibliography	74
4. PROGRESSIVE KINESIN-14 HSET EXHIBITS DIRECTIONAL FLEXIBILITY DEPENDING ON MOTOR TRAFFIC	75
4.1. Summary	75

4.2.	Introduction	76
4.3.	Results	78
4.4.	Discussion	90
4.5.	Conclusions	93
4.6.	Materials and Methods	93
4.7.	Acknowledgements	100
4.8.	Bibliography	101
5.	BIOCONJUGATED CORE-SHELL MICROPARTICLES FOR HIGH FORCE OPTICAL TRAPPING	107
5.1.	Summary	107
5.2.	Introduction	107
5.3.	Materials and Methods	109
5.4.	Results and Discussion	117
5.5.	Conclusions	125
5.6.	Acknowledgements	125
5.7.	Bibliography	126
6.	CONCLUSIONS AND FUTURE WORK	132
Appendix		
A.	PROTOCOLS	136
A.1.	Buffer Recipes	136
A.2.	Microtubule Preparation	143
A.3.	E-hook Cleaved Microtubule Preparation by Subtilisin Digestion	144
A.4.	Polarity-Marked Microtubule Preparation	145
A.5.	Kinesin Optical Trap Motility Assay	146
A.6.	Kinesin Bundle Assay for Optical Trap	149
A.7.	Microtubule Gliding Assay for Optical Trap	150
A.8.	anti-DIG Functionalized Beads	151
A.9.	Conjugation of anti-His to Amine on DNA Linker	153
A.10.	Amyloid Fiber Preparation	155
A.11.	Conjugation of NM monomer to SH-Core Shell Beads	157
A.12.	Amyloid Pulling Assay for Optical Trap	159
A.13.	TiO ₂ Core Shell Microsphere Synthesis	160
A.14.	Biotinylated Actin Filaments	164
A.15.	Actin Rupture Assay	165

LIST OF TABLES

Table	Page
2.1. Three-State Kinetic Model for Kif15	33
3.1. Coverstrand Sequences of Kinesins.	67
3.2. Loop 13 Sequences of Kinesins.	67
3.3. Neck Linker Sequences of Kinesins.	67
4.1. Boltzmann Model Parameters for Kinesin-14	80
4.2. Force Generation Parameters in Eg5/HSET Bundles.	89

LIST OF FIGURES

Figure	Page
1.1. Cell Cycle.	2
1.2. The Mitotic Spindle.	4
1.3. The Biological Motor Kinesin.	6
1.4. Kif15 Rescues Spindle Assembly in Eg5-independent Cells.	9
1.5. HSET Opposes Eg5 Force Generation in the Spindle.	11
1.6. Optical Trapping Ray Optic Schematic.	14
2.1. Oligomerization State of FL-Kif15.	30
2.2. N700 Motility Assay.	31
2.3. Kif15 Motility Assay.	34
2.4. Coil-1 Binding Assay.	35
2.5. Structured Movement of Coil-1 Under Force.	36
2.6. Microtubule Binding Assay.	38
2.7. N700 Binding Assay.	40
2.8. Coil-1/E-hook Interaction Needed for Bundling.	41
2.9. Combined Microtubule Gliding/Optical Tweezer Assay.	42
2.10. N700 Combined Microtubule Gliding/Optical Tweezer Assay.	43
2.11. Model for Kif15 Function in Microtubule Bundles.	45
3.1. Cover-Neck Bundle Force Generation Mechanism.	66
3.2. Kif15 Motility with Bead on Motor Head.	68
3.3. Western Blot of Antibody Pre-Bleeds.	70
3.4. ELISA Scores of CS Antibodies.	71
4.1. FL-HSET is Weakly Processive in Loaded Assay.	79

4.2.	HSET is Bidirectional in Unloaded Assay.	82
4.3.	HSET Tail Domain Required for Processivity.	84
4.4.	HSET Tail Domain Interacts with E-hooks.	86
4.5.	HSET Acts as a Force Brake Against Eg5 in Bundles.	88
5.1.	Synthetic Strategy for the Production of Anatase-Titania Core-Shell Particles Functionalized with Proteins or Nucleic Acid Structures.	111
5.2.	Synthesis and Characterization of Core-Shell Particles.	118
5.3.	Temperature Dependence of Core-Shell Particles.	120
5.4.	Fluorophore Addition to Core-Shell Particles.	122
5.5.	Amyloid Pulling Assay using Core-Shell Particles.	123
5.6.	Actin Rupture Assay.	124

CHAPTER 1

INTRODUCTION

1.1 Cancer and the Cell Cycle

Cancer is a disease that affects millions of people every year and is defined as having defects in regulatory signaling that governs normal cell growth, in other words, uncontrolled growth of cells. This year, approximately 1.7 million new cases of cancer will be diagnosed in the United States, and about 600,000 people will die from the disease [1]. Cancer research over the last few decades has been focused on understanding the underlying complicated and diverse mechanisms that manifest into devastating phenotypes that often times result in death. Better comprehension of these mechanisms allows for more targeted and efficient therapeutic approaches to best treat a patient in the clinic.

Hanahan and Weinberg outlined the categories in which cell physiology goes awry causing cancer, terming them the hallmarks of cancer [2, 3]. These include evasion of programmed cell death (apoptosis), self-sufficiency in growth signals, insensitivity to anti-growth signals, tissue invasion and metastasis, limitless replicative potential, and sustained angiogenesis. These changes are acquired during tumor development and nurture an environment that promotes “breaching of an anticancer defense mechanism”. The hallmarks get programmed into the cells and tissues, laying the foundation for cancer progression.

In order to understand the pathology associated with cancer cell growth, we need to understand how cells grow normally [4, 5, 6]. Somatic cells grow in two major steps: interphase and mitosis (Figure 1.1). During interphase, the cell grows and makes a copy of its DNA through G1, S, and G2 stages. The G1 phase, or first gap phase, involves the cell getting physically larger, copying organelles, and making the building blocks needed in later stages. In S phase, the cell synthesizes a second copy of the genome and centrosome, or microtubule organizing center (MTOC). In the second gap phase, G2, the cell further

grows, making proteins and organelles and also begins to prepare the cellular environment for mitosis.

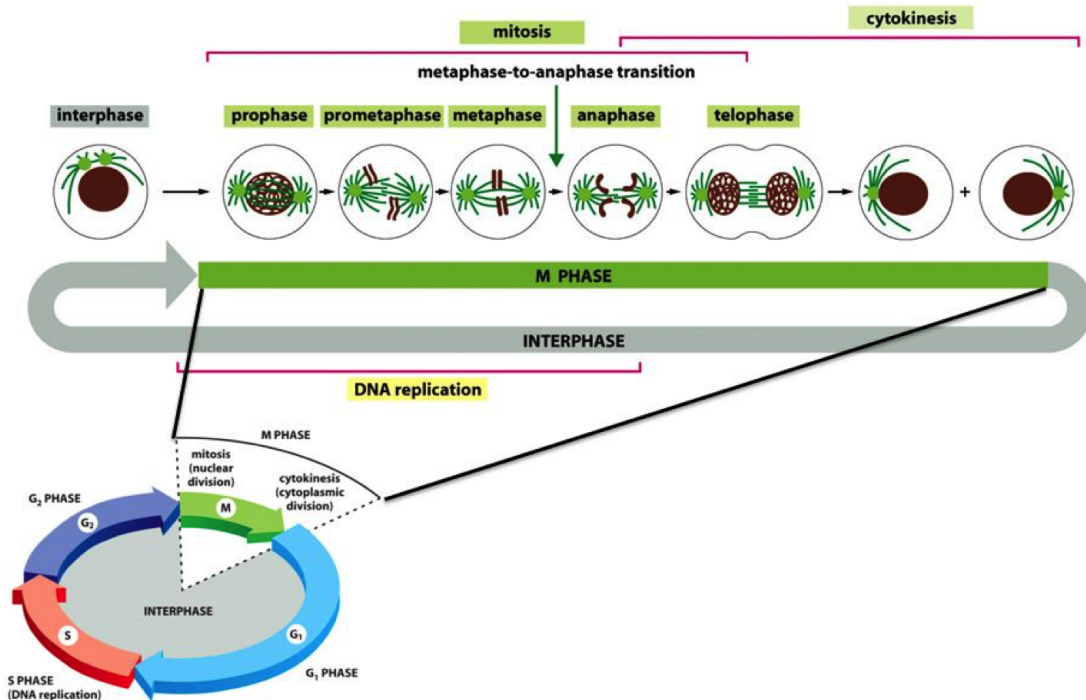


Figure 1.1: **Cell Cycle.** Phases of the cell cycle, including interphase and mitosis. Mitosis consists of prophase, metaphase, anaphase, telophase, and cytokinesis. See the text for details. Adapted from Alberts, *et al.*, Molecular Biology of the Cell, 5th Edition. [4] Reproduced with permission from the Taylor and Francis Group. License number: 4238331223952.

M phase involves the active division of the cell to produce two identical daughter cells. It is comprised of mitosis and cytokinesis. Mitosis involves the active reorganization and division of the cell through four stages named prophase, metaphase, anaphase, and telophase [5, 6, 4]. In prophase, DNA starts to condense into chromosomes in the nucleus, and the mitotic spindle begins to form in the cytoplasm. The mitotic spindle, dynamic machinery made of cytoskeletal elements, organizes the genetic material and ensures the integrity of their alignment before final division takes place. The nuclear envelope then breaks down, and the mitotic spindle begins to search for and capture the chromosomes. During metaphase, the chromosomes become aligned at the center of the cell, ready for division, so that each daughter cell gets an exact copy of the genetic material. Before entering the

next phase, anaphase, the spindle will go through a checkpoint process to make sure the chromosomes are properly aligned and attached. If the cell divided with improper attachments, the daughter cells would not be identical and would manifest disease states or cell death. Therefore, normally, cell division will halt at this checkpoint until problems are resolved. During anaphase, the chromosomes separate and are pulled toward the cell poles. Telophase consists of the cell starting to reorganize into its normal structure as cytokinesis, or the dividing of the cell contents, takes place.

As mentioned earlier, proper formation of the mitotic spindle is imperative to ensure that each daughter cell gets an exact copy of the genome. Because its formation is vital to cell proliferation, spindle formation and its associated machinery have been the target of cancer therapies [6, 7]. If the uncontrolled, rapid growth of cells can be stopped through these mitotic drugs, then it is possible to suppress the cancerous disease.

1.2 The Mitotic Spindle

The mitotic spindle is a dynamic macromolecular machine composed of microtubules (MTs) and microtubule associated proteins (MAPs) that is formed during prophase and metaphase (Figure 1.2) [5, 8, 9]. MTs consist of tubulin dimers made of α and β subunits that polymerize into filaments after hydrolysis of guanosine triphosphate (GTP) [10]. They also have negatively-charged carboxyl-terminal tails, or E-hooks [11, 12, 13, 14]. MTs have polarity based on their rate of polymerization from its nucleation point; they grow much more rapidly in one direction (toward the plus end) than the other (minus end). MAPs are proteins that interact with MTs to either build higher order structures (crosslinkers) or transport the MT substrate for spindle assembly or division (biological motors).

Proper centrosome separation and spindle assembly is required for accurate chromosome segregation during cell division. Centrosomes act as microtubule-organizing centers (MTOCs) that move to opposite ends of the cell just before nuclear envelope breakdown (NEB), giving the spindle its bipolar structure [15]. The centrosomes serve as nucleation

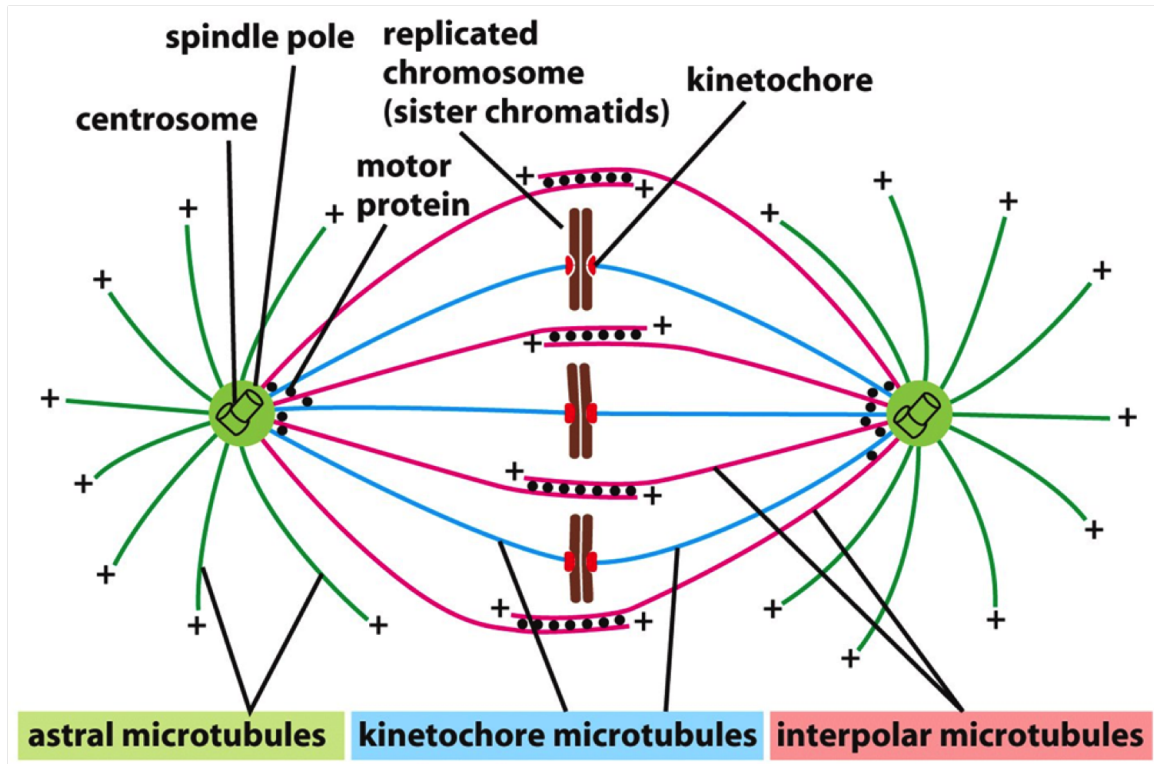


Figure 1.2: **The Mitotic Spindle.** Proper formation of the mitotic spindle is essential for correct chromosome alignment so that upon segregation, each daughter cell gets an exact copy of the genome. The spindle is bipolar in nature with organelles called centrosomes as the focal points. Three different kinds of microtubules are found throughout the spindle: astral MTs, interpolar MTs that are mostly anti-parallel in orientation, and kinetochore MTs (K-MTs) that are bundles of parallel MTs attached to the kinetochore of chromosomes. Molecular motors are pervasive throughout the spindle to aid in separating the centrosomes, MT polymerization and depolymerization, and balancing forces within the spindle. Adapted from Alberts, *et al.*, *Molecular Biology of the Cell*, 5th Edition. [4] Reproduced with permission from the Taylor and Francis Group. License number: 4238331223952.

sites for the minus ends of the MTs. The plus ends either aid in holding spindle orientation (astral MTs), interact with the kinetochore of the chromosome (kinetochore MTs, K-MTs, parallel MT bundles), or overlap and interact through various MAPs (interpolar MTs, anti-parallel MTs) [15]. A combination of MT depolymerization and motor movement causes force to be produced within the spindle to separate the poles, segregate chromosomes, and ultimately create two genetically identical daughter cells [15, 9].

1.3 Biological Motors

Biological motors are essential to sustain life [16]. These proteins convert chemical energy into mechanical work through conformational changes from ATP hydrolysis [17, 18, 19, 20, 21]. The kinesin family of motors uses this mechanical energy to walk hand-over-hand along highly conserved MT tracks to transport cargo through the cell and aid in cell division [16, 18, 19, 21, 22]. The myosin family of motors associate with actin to transport cargo and generate the forces necessary for muscle contraction. Deficiencies in these instrumental proteins have been linked to many diseases, such as but not limited to Alzheimer's disease in the case of transport kinesin in neurons and hypertrophic cardiomyopathy with myosin that causes heart hypercontractility [16, 23]. They are also the target of cancer therapies to aid in halting uncontrolled cell growth [7].

Kinesins are generally dimers of heavy chain and light chain monomers that twist together to form the enzyme (Figure 1.3) [17, 24, 25, 26]. The heavy chains contain the motor heads and the neck linker, and the light chains include a long α -helical stalk, important for oligomerization, and a globular cargo binding domain. This family of motors transports cargo within the cell by moving along MT substrates [16, 21, 27, 28]. Most kinesins are plus-end directed, meaning that they walk toward the end of the MT that polymerizes the fastest and ends with a β subunit. The mechanism by which it walks involves an asymmetric hand-over-hand motion, similar to the way humans walk putting one foot in front of the other [29, 30]. ATP binds to the catalytic site of the motor head, which pulls the trailing head on the MT to an advanced position. ADP release to a nucleotide free state then leads to tight binding to the MT. In the now trailing head, ATP hydrolysis and release of inorganic phosphate facilitates detachment from the MT, finishing the step. Single molecule optical trapping studies of kinesin revealed this mechanism, showing that these motors take 8 nm steps along MTs, noting that tubulin dimers are 8 nm apart, for every ATP that it hydrolyzes [22, 31]. These studies also revealed characteristics such as processivity, velocity, and stall force. Processivity refers to how far an unloaded motor can travel along its track

before dissociating. Kinesin-1 was found to take over one hundred steps without dissociating from the MT through gliding assays [32] and unloaded beads with one motor attached [18]. The velocity of kinesin-1 was found to be approximately 650 nm/sec [33]. When walking against load, such as in an optical trap, velocity decreased linearly with increasing force, and kinesin-1 moved against applied loads of up to 5-6 pN (stall force).

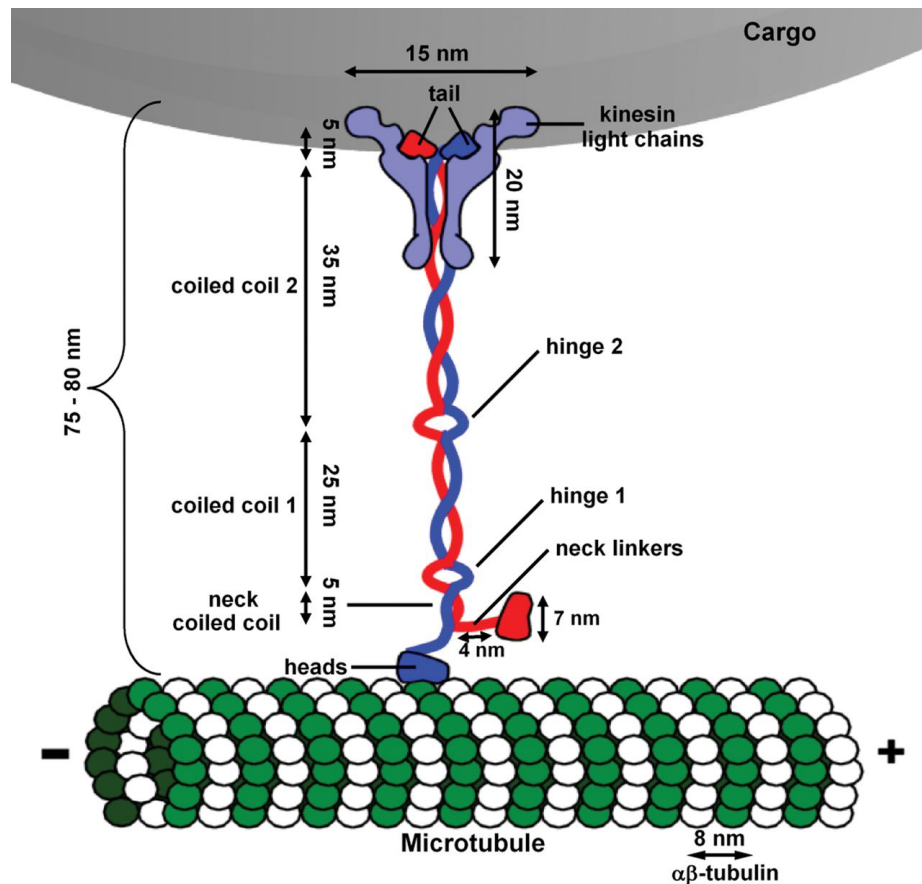


Figure 1.3: **The Biological Motor Kinesin.** Kinesins are molecular motors that use ATP hydrolysis to perform mechanical work. Kinesin-1, or conventional kinesin, is shown here. It has two motor heads that walk hand-over-hand along a MT lattice in 8 nm steps. Following the motor domains is a coiled-coil stalk, which is then followed by a globular cargo-binding domain. Adapted from Jeppesen, *et al.*, (2012) Biochemical Society Transactions. [34] Reproduced with permission from Portland Press Ltd. License number: 4238341042406.

1.4 Spindle Assembly by Motor Proteins

Kinesins play instrumental roles during mitosis [8, 35]. One of the main players in spindle assembly is the homotetrameric kinesin-5 Eg5 [36, 37]. It has been shown *in vitro* that Eg5 is capable of crosslinking anti-parallel MTs and sliding them apart by walking toward the plus end of the MTs with each set of motor heads [38]. It has a maximal stepping rate of 100 nm/sec, which is significantly slower than kinesin-1 [39]. Eg5 is also much less processive, taking about 8 steps at saturating ATP and zero load [39]. Eg5 inactivity has been shown to halt centrosome separation, arresting the cells in mitosis with a monopolar spindle [37, 40, 41, 42]. However, more recent studies have shown that there are other mechanisms that exist for spindle assembly in the absence of Eg5 activity [43, 44]. Simultaneous inhibition of Eg5 and dynein caused spindle formation to be rescued [45]. Another study showed that bipolar spindles did not collapse when Eg5 was inhibited [43, 44, 40]. Also, *Dictyostelium* and *C. elegans* do not require Eg5 to form a bipolar spindle [46, 47]. These results indicate that there must be some redundant backup mechanism to rescue bipolar spindle formation in Eg5-independent cells. The kinesin-12 Kif15 is thought to be a major player in this mechanism [43, 44, 48, 45, 49, 50, 51].

1.4.1 Kinesin-12, Kif15

The kinesin-12 Kif15, originally found in *Xenopus* oocytes, was found to be plus-end directed and localized to centrosomes and spindle MTs [52]. *In vitro* studies showed that a truncated version of *Xenopus* Kif15 without the N-terminal motor domain blocked centrosome separation and caused atypical spindle formation [53]. This study also showed that the C-terminal domain of *Xenopus* Kif15 was able to localize to the spindle poles without the motor domain, indicating that it contained a non-motor MT targeting domain. The structure of human Kif15 contains an N-terminal kinesin motor domain and a long C-terminal coiled coil with two conserved leucine zippers [54].

Some studies have indicated that Kif15 is not required for spindle assembly in *Xenopus* egg extracts or human cells [55]. This suggested that Kif15 involvement in spindle assembly is redundant to that of Eg5 or is not significant for bipolar spindle assembly. This was addressed through studies by Tanenbaum *et al.* and Vanneste *et al.* [43, 44]. Kif15 was depleted in human cells, and they became strongly sensitized to partial Eg5 inhibition. Also, maintenance of the bipolar spindle was dependent on Kif15 in Eg5-independent cells. This also suggests that Kif15 works redundantly to Eg5. While inhibition of Eg5 prevents bipolar spindle formation, meaning endogenous levels of Kif15 are not sufficient to form the spindle, over-expression of Kif15 in Eg5-independent cells rescued bipolar spindle formation. Since upregulation of Kif15 is sufficient to form the spindle, this indicates that Kif15 must act similarly to Eg5, containing the ability to produce outward forces to separate the poles.

Sturgill *et al.* suggested that Kif15 preferentially targets K-MTs and relies on them for force generation at physiological levels, antagonizing the efforts of Eg5 [48]. The Ohi lab produced an Eg5-independent cell line that utilized over-expression of Kif15 for survival [48, 50]. They found that Kif15 over-expression in the Eg5-independent line caused relocation of Kif15 from K-MTs to interpolar MTs, where it can generate force to separate poles (Figure 1.4). This indicates that Kif15 acts similarly to Eg5 in that it is able to crosslink and slide anti-parallel MTs apart.

To understand how a dimeric motor can replace the function of a tetramer, the mechanical properties and force generation capabilities of Kif15 were investigated using optical tweezers [51]. Measurements of motor subdomains, single motors, and motor-microtubule bundles paired with stochastic simulations unveiled a mechanism for how Kif15 can rescue Eg5 function under chemotherapeutic conditions. It was found that Kif15's non-motor MT binding domain was stronger than the stall force of the motor, revealing that this motor has the ability to build up mechanical strain and slide MTs apart. However, single motor interactions on single MTs do not fully reflect the complex spindle structure in which

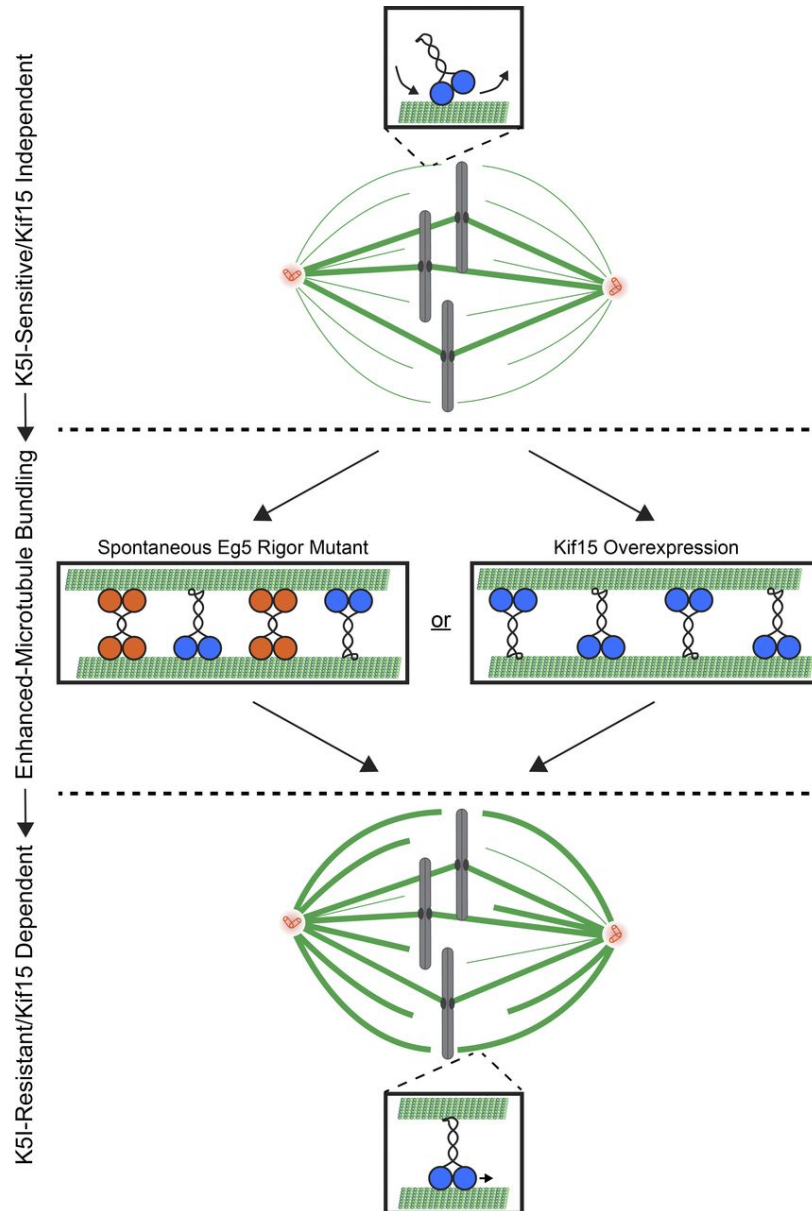


Figure 1.4: **Kif15 Rescues Spindle Assembly in Eg5-independent Cells.** Upon Eg5 inhibition, rigor mutants can act as crosslinkers to enhance MT bundling. Kif15 overexpression due to Eg5 inactivity can enhance bundling as well. This forms a substrate on which Kif15 can act, as it targets already bundled MTs. Kif15 proceeds to slide MTs apart to form the spindle when Eg5 has been inhibited. Adapted from Sturgill, *et al.*, (2016) *Journal of Cell Biology*. [50] Reproduced with permission from The Rockefeller University Press. License number: 4238320650581.

Kif15 works. In order to reconstitute a more native environment, a new and novel assay was developed to evaluate Kif15 function in bundled assemblies. It was determined that

Kif15 slides anti-parallel MTs apart while parallel bundles remain stationary (Figure 2). This is reflective of the location-specific roles that Kif15 plays in the spindle: static MT crosslinker/force regulator under physiological conditions (parallel kinetochore MTs) and active MT slider under drugged conditions (anti-parallel interpolar MTs). These studies illuminate the therapeutic importance of Kif15, whose inhibition in tandem with an Eg5 poison could prove to be more effective at halting cancer in the clinic. See Chapter 2 for details.

1.4.2 Kinesin-14, HSET

The human analog of kinesin-14 is termed human spleen, embryo, and testes protein, or HSET (also known as KifC1). Other family members include Ncd (*Drosophila*), CHO2 (hamster), and Kar3 (budding yeast). The kinesin-14 family of motors differs from other kinesins functionally and structurally [56, 57, 58, 59]. Dimeric kinesin-14s have C-terminal motor domains (as opposed to being at the N-terminus for other kinesins), and they walk toward the minus end of MTs. The motor domains are followed by a coiled-coil stalk and N-terminal globular domain. The globular domain contains an ATP-independent MT binding site which allows for crosslinking and sliding of MTs, similarly to Kif15.

Previous studies have shown kinesin-14 Ncd to be non-processive, or it cannot walk along a MT without dissociating. Kinetic and three-bead trapping studies have suggested that Ncd has little to no chemical processivity [60, 61]. Since kinesin-14 was defined as non-processive, it was assumed that it worked together as members of a group to perform functions within the spindle [62, 63].

In spite of the apparent lack of processivity, during spindle assembly, kinesin-14s have been proposed to regulate spindle dynamics by opposing outward forces generated by motors such as Eg5 (Figure 1.5). As HSET is minus end directed and has its non-motor MT binding domain, it can act to crosslink and focus MT minus ends, constructing the bipolar structure necessary for proper chromosome segregation. However, in human somatic cells,

HSET is not necessary for pole focusing as the two centrosomes act as the primary microtubule organizing centers (MTOC). In meiotic cells, kinesin-14 acts to focus the minus ends of the MTs to form a MTOC in lieu of centrosomes [64].

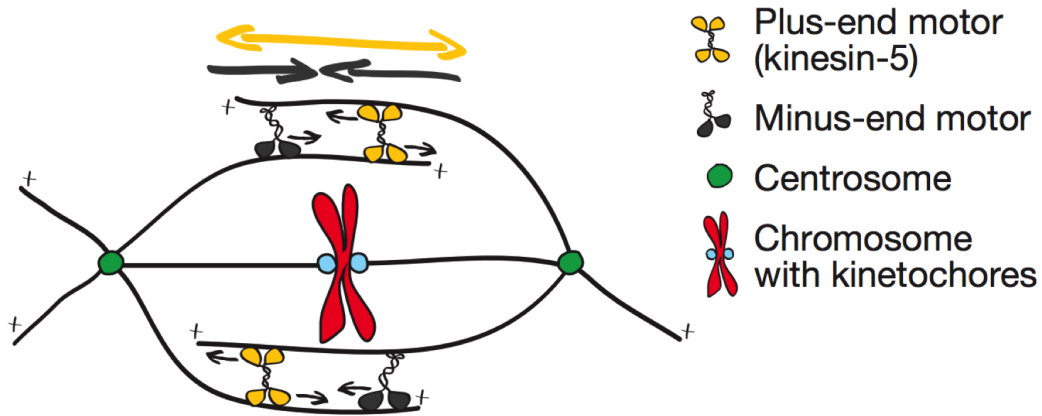


Figure 1.5: **HSET Opposes Eg5 Force Generation in the Spindle.** Even though kinesin-14 has previously been found to be non-processive at the single molecule level, it has been found to significantly oppose Eg5 forces in the spindle by creating an inward force. Adapted from Kapitein, *et al.*, (2005) Nature. [38] Reproduced with permission from Nature Publishing Group. License number: 4238320993563.

On the other hand, cancer cells with supernumerary, or more than two, centrosomes need kinesin-14 to focus the spindle into two poles and allow proper mitosis to continue [65]. Kleylein-Sohn *et al.* demonstrated that HSET was essential for proper spindle assembly in acentrosomal and centrosomal human cancer cells, regardless of normal or supernumerary centrosome number [65]. However, kinesin-14 depletion in normal cells has little to no effect, suggesting that it is acting as a backup mechanism for pole focusing [65, 64]. This makes HSET an attractive cancer therapy target, as its inhibition would ideally only attack cancerous cells while having minimal effect on healthy cells containing two centrosomes.

The single molecule mechanics of HSET were investigated using optical trapping to give insight about how a previously defined non-processive motor could accomplish macroscopic force generation during mitosis. Constructs containing various sub-components of the motor were utilized to determine the role of each domain, and step size, dwell times, and

stall forces were measured. Rupture assays were also performed on the ATP-independent tail domain to determine the strength of the interaction with MTs. We showed that HSET has a processive nature with the ability to complete multiple steps along a MT before release. Moreover, the tail binding domain of HSET and its interaction with the negatively charged E-hook tail of tubulin is necessary for long-range processivity. To further investigate the role of HSET in spindle mechanics and force balance, an optical tweezer assay was utilized to evaluate HSET force generation in MT bundles (alone and with Eg5), and we found that it acts as a force brake against Eg5, the main MT slider, in vitro. The motor's ability to crosslink and slide MTs, as well as its processive nature, suggest that HSET is able to discriminate between different cellular environments. This reflects its conditional ability to be physiologically relevant when centrosome number is not two, making it an attractive cancer therapy target. See Chapter 4 for details.

1.5 Single Molecule Methods

Single molecule studies have been essential in evaluating the mechanistic behavior of molecular motors, including conventional kinesin and myosin, as well as many other biophysical phenomena, at high resolution [18, 19, 20, 22, 33, 29, 30]. These intricate assays are able to evaluate the optical behavior of subpopulations of molecules that would normally be overshadowed in bulk experiments. Force dependent processes, such as motor motility, protein unfolding, and cell rheology, can be probed using magnetic tweezers, optical tweezers, or atomic force microscopy (AFM). Each technique has its advantages and disadvantages that can be applied to experiments requiring different levels of force and spatial resolution. The spatial resolution for magnetic tweezers, optical tweezers, and AFM are 5-10 nm, 0.1-2 nm, and 0.5-1 nm, respectively [66]. The force capacity of the same techniques are $0.01-10^4$ pN, 0.1-100 pN, and $10-10^4$ pN, respectively. Magnetic tweezers can be used with multiplexed assays, obtaining a larger amount of data per experiment, but it is usually performed through indirect manipulation. Optical tweezers feature a low-

noise and low-drift environment for pN and nm resolution measurements but is limited to a relatively low force capacity. AFM can be utilized in high-force pulling and interaction assays, as well as imaging, but it typically has a large minimal force. Therefore, the proper technique must be carefully chosen for any certain biophysical experiment.

Single molecule techniques require forms of functionalization or fluorophore labeling to probe mechanistic questions. Measurements can provide information such as bond lifetimes, dissociation kinetics, step sizes, dwell times, and stall forces, among others. Fluorescence microscopy techniques, such as total internal reflection fluorescence (TIRF) and Forster resonance energy transfer (FRET), are also extremely useful for tracking proteins of interest as well as probing short distance interactions or conformational changes through characteristic emission of the fluorophores. Interlaced single molecule optical trapping and fluorescence has also been developed to monitor conformational and mechanical changes simultaneously [67, 68].

1.5.1 Optical Trapping

The main tool used throughout this dissertation is optical trapping. Ashkin *et al.* first demonstrated the technique, which involves using a highly focused laser beam with a Gaussian intensity profile to trap and maneuver micron sized dielectric objects (normally beads) [69, 70, 71]. When light interacts with a dielectric object of a different refractive index than its surrounding medium, the light changes direction, causing a change in momentum and concomitantly generates a scattering force along the axis of propagation. An overfilled high numerical aperture objective is used to create a highly focused laser beam, and therein a strong gradient force, causing the object to be pulled toward the center of the Gaussian photon distribution. These forces are illustrated in a simplified ray optic schematic in Figure 1.6. The laser trap acts as a Hookean spring within ~ 200 nm of the trap center and has an intrinsic trap stiffness. Therefore, as the object is displaced from the trap center, force is generated ($F = -k_{\text{trap}}x$) [72].

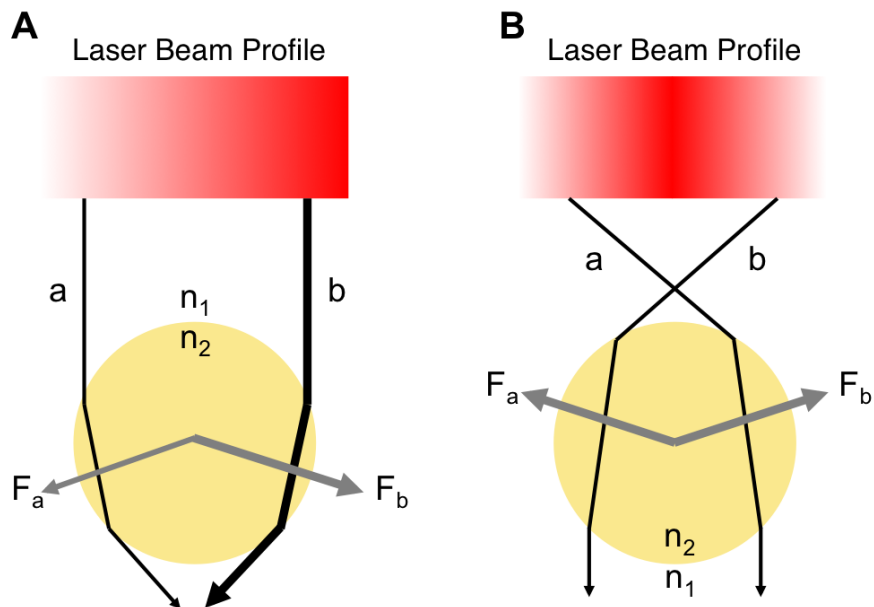


Figure 1.6: **Optical Trapping Ray Optic Schematic.** (A) Here, the beam becomes more intense from left to right. Refraction through a dielectric object where $n_2 > n_1$ will create a larger gradient force with more intense light (F_b) than with less intense light (F_a). This gradient force will push the bead down and to the right. (B) A tightly focused laser beam, as with an optical trap, has a Gaussian intensity profile. As the photon flux is highest at the center, gradient forces will pull the bead toward the beam focus, thus forming a trap. Scattering forces will cause the bead to be trapped slightly above the focus. Image based on Neuman, *et al.*, (2004) Review of Scientific Instruments.[72]

As mentioned before, the trapping handle has to have an index of refraction larger than that of the surrounding medium (normally buffer or water for this dissertation) but must also be close to the size of the laser beam, usually within 0.1-10x the wavelength. Even though the size of many biological systems of interest are within this range, objects smaller than the diffraction limit (~ 200 nm) are difficult to observe and manipulate. Therefore, beads approximately one micron in diameter (1000 nm bead in an infrared laser beam, ~ 1000 nm) are generally used as physical handles for the object of interest. The beads can be functionalized to bind a dilute concentration of protein, motor, etc. and then be used to indirectly apply and measure forces and displacements. Infrared wavelengths are normally used as trapping lasers because absorption of light by water, buffer, and proteins

is minimized in this range, reducing the risk of protein photodamage and sample heating [20]. This also allows for combining trapping and fluorescence experiments (demonstrated in Chapters 2 and 3) as the visible spectrum is left available for probing and measurement by a separate laser system.

Experiments performed in this dissertation were on a custom-built instrument described previously [73, 74, 75]. The optical trapping setup has separate trapping and detection systems [76, 72, 77]. A low power detection laser is used to track the bead position from its scattered light collected by a quadrant photodiode (QPD). The detection laser power is about one tenth lower than the trapping laser and is at 975 nm to differentiate between signals.

The position signal obtained from the detection laser and calibration routines are used to determine the trap stiffness and yield force measurements. Calibration methods for both position and trap stiffness are reviewed in Neuman *et al.* [72]. In this setup, acousto-optic deflectors (AODs) are used to control and manipulate the trapping beam via a computer and LabView algorithms. Position is manipulated by a piezostage with nanometer resolution that can be controlled by hand or through LabView. Position is calibrated by moving the trap a known distance with the computer-controlled AODs through the detection zone. Trap stiffness is calibrated using the equipartition method, which measures the statistical variance of a trapped particle. Assuming the particle is trapped in a harmonic potential, similar to a mass on a Hookean spring, it has an energy of $\frac{1}{2}k_{\text{trap}}x^2$. This energy is equal to the fluctuation of the position of the particle due to Brownian motion imparted by the surrounding medium at a known temperature, $\frac{1}{2}\kappa_B T$. Therefore, knowing viscosity or size of the sample is not required, as it would with measuring Stokes' drag [72]. As all of the previously mentioned parameters are known minus k_{trap} , it can be calculated. The trap stiffness can then be multiplied by the instantaneous displacement of the trapped object to calculate force.

1.5.2 Core-Shell Microparticles

The particles used in optical trapping experiments are often polystyrene beads, as it is a dielectric material and easily synthesized. These beads are functionalized through a variety of methods so that specific biological interactions can be interrogated. Some of the commercially available functionalizations include primary amines, carboxylates, and hydroxyls. However, the vast majority of trapping experiments using polystyrene beads measure low forces (10s of pN), such as motor motility or binding strength of proteins to their substrate.

To faithfully investigate high force biological phenomena, such as the strength of bio-fibers and rheological measurements, the trapping handle, or bead, must be modified. The refractive index change between the surrounding medium (water) and polystyrene is not enough to generate the forces necessary to probe these interactions, and the Schaeffer lab pioneered the synthesis of core-shell particles for high force optical trapping [78]. Using a custom protocol, we synthesized microparticles with a higher refractive index core, but also bioconjugated them, to increase the trap stiffness and thus be able to perform experiments at previously unattainable forces. See Chapter 5 for synthesis and bioconjugation details.

1.6 Bibliography

- [1] American Cancer Society. *Cancer facts and figures*. The Society, 2008.
- [2] Douglas Hanahan and Robert A Weinberg. The hallmarks of cancer. *cell*, 100(1):57–70, 2000.
- [3] Douglas Hanahan and Robert A Weinberg. Hallmarks of cancer: the next generation. *cell*, 144(5):646–674, 2011.
- [4] B Alberts, A Johnson, J Lewis, M Raff, K Roberts, and P Walter. *Molecular biology of the cell*, 5th edn, garland science, new york, 2007. ISBN, 1174808063:1392.
- [5] Rebecca Heald. Motor function in the mitotic spindle minireview. *Cell*, 102(4):399–402, 2000.
- [6] Rebecca Heald and Alexey Khodjakov. Thirty years of search and capture: The complex simplicity of mitotic spindle assembly. *J Cell Biol*, 211(6):1103–1111, 2015.
- [7] Oliver Rath and Frank Kozielski. Kinesins and cancer. *Nature reviews cancer*, 12(8):527–539, 2012.
- [8] David J Sharp, Gregory C Rogers, and Jonathan M Scholey. Microtubule motors in mitosis. *Nature*, 407(6800):41–47, 2000.
- [9] E Karsenti and I Vernos. The mitotic spindle: a self-made machine. *Science*, 294(5542):543–547, 2001.
- [10] Carla Tucker and Lawrence SB Goldstein. Probing the kinesin-microtubule interaction. *Journal of Biological Chemistry*, 272(14):9481–9488, 1997.
- [11] Luis Serrano, Javier De La Torre, Ricardo B Maccioni, and JESStS Avila. Involvement of the carboxyl-terminal domain of tubulin in the regulation of its assembly. *Proceedings of the National Academy of Sciences*, 81(19):5989–5993, 1984.

- [12] Yasushi Okada and Nobutaka Hirokawa. Mechanism of the single-headed processivity: diffusional anchoring between the k-loop of kinesin and the c terminus of tubulin. *Proceedings of the National Academy of Sciences*, 97(2):640–645, 2000.
- [13] Zhaohui Wang and Michael P Sheetz. The c-terminus of tubulin increases cytoplasmic dynein and kinesin processivity. *Biophysical Journal*, 78(4):1955–1964, 2000.
- [14] Stefan Lakämper and Edgar Meyhöfer. The e-hook of tubulin interacts with kinesin’s head to increase processivity and speed. *Biophysical journal*, 89(5):3223–3234, 2005.
- [15] Sharat Gadde and Rebecca Heald. Mechanisms and molecules of the mitotic spindle. *Current Biology*, 14(18):R797–R805, 2004.
- [16] Lawrence SB Goldstein. Kinesin molecular motors: transport pathways, receptors, and human disease. *Proceedings of the National Academy of Sciences*, 98(13):6999–7003, 2001.
- [17] Ronald D Vale, Thomas S Reese, and Michael P Sheetz. Identification of a novel force-generating protein, kinesin, involved in microtubule-based motility. *Cell*, 42(1):39–50, 1985.
- [18] Steven M Block, Lawrence SB Goldstein, and Bruce J Schnapp. Bead movement by single kinesin molecules studied with optical tweezers. *Nature*, 348(6299):348–352, 1990.
- [19] Karel Svoboda, Christoph F Schmidt, Bruce J Schnapp, and Steven M Block. Direct observation of kinesin stepping by optical trapping interferometry. *Nature*, 365(6448):721–727, 1993.
- [20] Karel Svoboda and Steven M Block. Force and velocity measured for single kinesin molecules. *Cell*, 77(5):773–784, 1994.

- [21] Ronald D Vale, Takashi Funatsu, Daniel W Pierce, Laura Romberg, Yoshie Harada, and Toshio Yanagida. Direct observation of single kinesin molecules moving along microtubules. *Nature*, 380(6573):451, 1996.
- [22] Mark J Schnitzer and Steven M Block. Kinesin hydrolyses one atp per 8-nm step. *Nature*, 388(6640):386–390, 1997.
- [23] Suman Nag, Darshan V Trivedi, Saswata S Sarkar, Shirley Sutton, Kathleen M Ruppel, and James A Spudich. Beyond the myosin mesa: a potential unifying hypothesis on the underlying molecular basis of hyper-contractility caused by a majority of hypertrophic cardiomyopathy mutations. *bioRxiv*, page 065508, 2016.
- [24] David M Roof, Pamela B Meluh, and Mark D Rose. Kinesin-related proteins required for assembly of the mitotic spindle. *The Journal of cell biology*, 118(1):95–108, 1992.
- [25] Ronald D Vale and Robert J Fletterick. The design plan of kinesin motors. *Annual review of cell and developmental biology*, 13(1):745–777, 1997.
- [26] David D Hackney. Highly processive microtubule-stimulated atp hydrolysis by dimeric kinesin head domains. *Nature*, 377(6548):448–450, 1995.
- [27] Nobutaka Hirokawa. Kinesin and dynein superfamily proteins and the mechanism of organelle transport. *Science*, 279(5350):519–526, 1998.
- [28] Nobutaka Hirokawa, Yasuko Noda, Yosuke Tanaka, and Shinsuke Niwa. Kinesin superfamily motor proteins and intracellular transport. *Nature reviews Molecular cell biology*, 10(10):682–696, 2009.
- [29] Charles L Asbury, Adrian N Fehr, and Steven M Block. Kinesin moves by an asymmetric hand-over-hand mechanism. *Science*, 302(5653):2130–2134, 2003.
- [30] Ahmet Yildiz, Michio Tomishige, Ronald D Vale, and Paul R Selvin. Kinesin walks hand-over-hand. *Science*, 303(5658):676–678, 2004.

- [31] David L Coy, Michael Wagenbach, and Jonathon Howard. Kinesin takes one 8-nm step for each atp that it hydrolyzes. *Journal of Biological Chemistry*, 274(6):3667–3671, 1999.
- [32] J Howard, AJ Hudspeth, and RD Vale. Movement of microtubules by single kinesin molecules. *Nature*, 342(6246):154–158, 1989.
- [33] Steven M Block, Charles L Asbury, Joshua W Shaevitz, and Matthew J Lang. Probing the kinesin reaction cycle with a 2d optical force clamp. *Proceedings of the National Academy of Sciences*, 100(5):2351–2356, 2003.
- [34] George M Jeppesen and JK Heinrich Hoerber. The mechanical properties of kinesin-1: a holistic approach, 2012.
- [35] Linda Wordeman. How kinesin motor proteins drive mitotic spindle function: Lessons from molecular assays. In *Seminars in cell & developmental biology*, volume 21, pages 260–268. Elsevier, 2010.
- [36] Kenneth E Sawin, Katherine LeGuellec, Michel Philippe, and Timothy J Mitchison. Mitotic spindle organization by a plus-end-directed microtubule motor. *Nature*, 359(6395):540–543, 1992.
- [37] Kenneth E Sawin and Timothy J Mitchison. Mutations in the kinesin-like protein eg5 disrupting localization to the mitotic spindle. *Proceedings of the National Academy of Sciences*, 92(10):4289–4293, 1995.
- [38] Lukas C Kapitein, Erwin JG Peterman, Benjamin H Kwok, Jeffrey H Kim, Tarun M Kapoor, and Christoph F Schmidt. The bipolar mitotic kinesin eg5 moves on both microtubules that it crosslinks. *Nature*, 435(7038):114–118, 2005.
- [39] Megan T Valentine, Polly M Fordyce, and Steven M Block. Eg5 steps it up! *Cell Division*, 1(1):31, 2006.

- [40] Tarun M Kapoor, Thomas U Mayer, Margaret L Coughlin, and Timothy J Mitchison. Probing spindle assembly mechanisms with monastrol, a small molecule inhibitor of the mitotic kinesin, eg5. *The Journal of cell biology*, 150(5):975–988, 2000.
- [41] Tarun M Kapoor and Timothy J Mitchison. Eg5 is static in bipolar spindles relative to tubulin. *The Journal of cell biology*, 154(6):1125–1134, 2001.
- [42] Zoltan Maliga, Tarun M Kapoor, and Timothy J Mitchison. Evidence that monastrol is an allosteric inhibitor of the mitotic kinesin eg5. *Chemistry & biology*, 9(9):989–996, 2002.
- [43] Marvin E Tanenbaum, Libor Macurek, Aniek Janssen, Erica F Geers, Mónica Alvarez-Fernández, and René H Medema. Kif15 cooperates with eg5 to promote bipolar spindle assembly. *Current biology*, 19(20):1703–1711, 2009.
- [44] David Vanneste, Masatoshi Takagi, Naoko Imamoto, and Isabelle Vernos. The role of hklp2 in the stabilization and maintenance of spindle bipolarity. *Current Biology*, 19(20):1712–1717, 2009.
- [45] Roy GHP van Heesbeen, Marvin E Tanenbaum, and René H Medema. Balanced activity of three mitotic motors is required for bipolar spindle assembly and chromosome segregation. *Cell reports*, 8(4):948–956, 2014.
- [46] John D Bishop, Zhenbo Han, and Jill M Schumacher. The caenorhabditis elegans aurora b kinase air-2 phosphorylates and is required for the localization of a bim kinesin to meiotic and mitotic spindles. *Molecular biology of the cell*, 16(2):742–756, 2005.
- [47] Irina Tikhonenko, Dilip K Nag, Nora Martin, and Michael P Koonce. Kinesin-5 is not essential for mitotic spindle elongation in dictyostelium. *Cytoskeleton*, 65(11):853–862, 2008.

- [48] Emma G Sturgill and Ryoma Ohi. Kinesin-12 differentially affects spindle assembly depending on its microtubule substrate. *Current Biology*, 23(14):1280–1290, 2013.
- [49] Emma G Sturgill, Dibyendu Kumar Das, Yoshimasa Takizawa, Yongdae Shin, Scott E Collier, Melanie D Ohi, Wonmuk Hwang, Matthew J Lang, and Ryoma Ohi. Kinesin-12 kif15 targets kinetochore fibers through an intrinsic two-step mechanism. *Current Biology*, 24(19):2307–2313, 2014.
- [50] Emma G Sturgill, Stephen R Norris, Yan Guo, and Ryoma Ohi. Kinesin-5 inhibitor resistance is driven by kinesin-12. *J Cell Biol*, 213(2):213–227, 2016.
- [51] Dana N Reinemann, Emma G Sturgill, Dibyendu Kumar Das, Miriam Steiner Degen, Zsuzsanna Vörös, Wonmuk Hwang, Ryoma Ohi, and Matthew J Lang. Collective force regulation in anti-parallel microtubule gliding by dimeric kif15 kinesin motors. *Current Biology*, 27(18):2810–2820, 2017.
- [52] Isabelle Vernos, Janet Heasman, and Chris Wylie. Multiple kinesin-like transcripts in xenopus oocytes. *Developmental biology*, 157(1):232–239, 1993.
- [53] Haralabia Boleti, Eric Karsenti, and Isabelle Vernos. Xklp2, a novel xenopus centrosomal kinesin-like protein required for centrosome separation during mitosis. *Cell*, 84(1):49–59, 1996.
- [54] Torsten Wittmann, Haralabia Boleti, Claude Antony, Eric Karsenti, and Isabelle Vernos. Localization of the kinesin-like protein xklp2 to spindle poles requires a leucine zipper, a microtubule-associated protein, and dynein. *The Journal of cell biology*, 143(3):673–685, 1998.
- [55] Claire E Walczak, Isabelle Vernos, Timothy J Mitchison, Eric Karsenti, and Rebecca Heald. A model for the proposed roles of different microtubule-based motor proteins in establishing spindle bipolarity. *Current biology*, 8(16):903–913, 1998.

- [56] Rashmi Chandra, Edward D Salmon, Harold P Erickson, Andrew Lockhart, and Sharyn A Endow. Structural and functional domains of the drosophila ncd microtubule motor protein. *Journal of Biological Chemistry*, 268(12):9005–9013, 1993.
- [57] RA Walker. Ncd and kinesin motor domains interact with both alpha-and beta-tubulin. *Proceedings of the National Academy of Sciences*, 92(13):5960–5964, 1995.
- [58] Claire E Walczak, Suzie Verma, and Timothy J Mitchison. Xctk2: a kinesin-related protein that promotes mitotic spindle assembly in xenopus laevis egg extracts. *The Journal of cell biology*, 136(4):859–870, 1997.
- [59] A Karabay and RA Walker. The ncd tail domain promotes microtubule assembly and stability. *Biochemical and biophysical research communications*, 258(1):39–43, 1999.
- [60] IM-TC Crevel, A Lockhart, and RA Cross. Kinetic evidence for low chemical processivity in ncd and eg511 edited by j. karn. *Journal of molecular biology*, 273(1):160–170, 1997.
- [61] Michael J DeCastro, Chih-Hu Ho, and Russell J Stewart. Motility of dimeric ncd on a metal-chelating surfactant: evidence that ncd is not processive. *Biochemistry*, 38(16):5076–5081, 1999.
- [62] Marcus Braun, Douglas R Drummond, Robert A Cross, and Andrew D McAinsh. The kinesin-14 klp2 organizes microtubules into parallel bundles by an atp-dependent sorting mechanism. *Nature cell biology*, 11(6):724–730, 2009.
- [63] Gero Fink, Lukasz Hajdo, Krzysztof J Skowronek, Cordula Reuther, Andrzej A Kasprzak, and Stefan Diez. The mitotic kinesin-14 ncd drives directional microtubule–microtubule sliding. *Nature cell biology*, 11(6):717–723, 2009.

- [64] Vicki Mountain, Calvin Simerly, Louisa Howard, Asako Ando, Gerald Schatten, and Duane A Compton. The kinesin-related protein, hset, opposes the activity of eg5 and cross-links microtubules in the mammalian mitotic spindle. *The Journal of cell biology*, 147(2):351–366, 1999.
- [65] Julia Kleylein-Sohn, Bernadette Pöllinger, Michaela Ohmer, Francesco Hofmann, Erich A Nigg, Brian A Hemmings, and Markus Wartmann. Acentrosomal spindle organization renders cancer cells dependent on the kinesin hset. *J Cell Sci*, 125(22):5391–5402, 2012.
- [66] Keir C Neuman and Attila Nagy. Single-molecule force spectroscopy: optical tweezers, magnetic tweezers and atomic force microscopy. *Nature methods*, 5(6):491–505, 2008.
- [67] Matthew J Lang, Polly M Fordyce, and Steven M Block. Combined optical trapping and single-molecule fluorescence. *Journal of biology*, 2(1):6, 2003.
- [68] Matthew J Lang, Polly M Fordyce, Anita M Engh, Keir C Neuman, and Steven M Block. Simultaneous, coincident optical trapping and single-molecule fluorescence. *Nature methods*, 1(2):133–139, 2004.
- [69] Arthur Ashkin. Acceleration and trapping of particles by radiation pressure. *Physical review letters*, 24(4):156, 1970.
- [70] Arthur Ashkin and JM Dziedzic. Optical levitation by radiation pressure. *Applied Physics Letters*, 19(8):283–285, 1971.
- [71] Arthur Ashkin, James M Dziedzic, JE Bjorkholm, and Steven Chu. Observation of a single-beam gradient force optical trap for dielectric particles. *Optics letters*, 11(5):288–290, 1986.

- [72] Keir C Neuman and Steven M Block. Optical trapping. *Review of scientific instruments*, 75(9):2787–2809, 2004.
- [73] Marie-Eve Aubin-Tam, Adrian O Olivares, Robert T Sauer, Tania A Baker, and Matthew J Lang. Single-molecule protein unfolding and translocation by an atp-fueled proteolytic machine. *Cell*, 145(2):257–267, 2011.
- [74] Yongdae Shin, Yaqing Du, Scott E Collier, Melanie D Ohi, Matthew J Lang, and Ryoma Ohi. Biased brownian motion as a mechanism to facilitate nanometer-scale exploration of the microtubule plus end by a kinesin-8. *Proceedings of the National Academy of Sciences*, 112(29):E3826–E3835, 2015.
- [75] Ahmad S Khalil, David C Appleyard, Anna K Labno, Adrien Georges, Martin Karplus, Angela M Belcher, Wonmuk Hwang, and Matthew J Lang. Kinesin’s cover-neck bundle folds forward to generate force. *Proceedings of the National Academy of Sciences*, 105(49):19247–19252, 2008.
- [76] Matthew J Lang, Charles L Asbury, Joshua W Shaevitz, and Steven M Block. An automated two-dimensional optical force clamp for single molecule studies. *Biophysical journal*, 83(1):491–501, 2002.
- [77] Thomas T Perkins. Optical traps for single molecule biophysics: a primer. *Laser & Photonics Reviews*, 3(1-2):203–220, 2009.
- [78] Anita Jannasch, Ahmet F Demirörs, Peter DJ Van Oostrum, Alfons Van Blaaderen, and Erik Schäffer. Nanonewton optical force trap employing anti-reflection coated, high-refractive-index titania microspheres. *Nature Photonics*, 6(7):469–473, 2012.

CHAPTER 2

COLLECTIVE FORCE REGULATION IN ANTI-PARALLEL MICROTUBULE GLIDING BY DIMERIC KIF15 KINESIN MOTORS

*This chapter is adapted from Reinemann *et al.*, “Collective Force Regulation in Anti-Parallel Microtubule Gliding by Dimeric Kif15 Kinesin Motors” *Current Biology*, 27, 2810-2820 (2017) by permission granted under the Elsevier license policy.

2.1 Summary

During cell division, the mitotic kinesin-5 Eg5 generates most of the force required to separate centrosomes during spindle assembly. However, Kif15, another mitotic kinesin, can replace Eg5 function permitting mammalian cells to acquire resistance to Eg5 poisons. Unlike Eg5, the mechanism by which Kif15 generates centrosome separation forces is unknown. Here, we investigated the mechanical properties and force generation capacity of Kif15 at the single molecule level using optical tweezers. We found that the non-motor microtubule-binding tail domain interacts with the microtubule's E-hook tail with a rupture force higher than the stall force of the motor. This allows Kif15 dimers to productively and efficiently generate forces that could potentially slide microtubules apart. Using an *in vitro* optical trapping and fluorescence assay, we found that Kif15 slides anti-parallel microtubules apart with gradual force build-up while parallel microtubule bundles remain stationary with a small amount of antagonizing force generated. A stochastic simulation shows the essential role of Kif15's tail domain for load storage within the Kif15-microtubule system. These results suggest a mechanism for how Kif15 rescues bipolar spindle assembly.

2.2 Introduction

A hallmark of the G2/M transition is the conversion of an interphase microtubule cytoskeleton into a bipolar spindle. Bipolarity is essential for spindle function and is established by many microtubule-associated proteins that collectively move centrosomes to opposite cell poles [1]. One factor central to spindle assembly is the homotetrameric kinesin-5, Eg5, that crosslinks and slides anti-parallel microtubules apart [2]. Eg5 inactivation blocks centrosome separation, resulting in a monopolar spindle [3, 4, 5, 6, 7, 8, 9, 10]. However, several lines of evidence indicate that kinesin-12s also generate forces relevant for spindle assembly. In *C. elegans*, a kinesin-12 (KLP-18) rather than kinesin-5 (BMK-1) is essential for spindle formation [11, 12]. In humans, kinesin-12 Kif15 prevents [13] or slows [14] kinesin-5 inhibitor (K5I)-triggered collapse of the metaphase spindle. Kif15 overexpression can nullify the cytotoxic effects of K5Is by driving spindle assembly [13, 15] and is essential for HeLa cells to acquire K5I resistance [16]. These results suggest that kinesin-5s and kinesin-12s share strong functional homology, but the biophysical underpinnings are unclear because the motors differ in their cell biological and biochemical properties.

In mammalian cells, the mitotic localizations of Kif15 and Eg5 are significantly different. Kif15 enriches on kinetochore microtubules in prometaphase and then distributes uniformly along spindle microtubules at metaphase [17]. In contrast, Eg5 binds microtubules early during spindle assembly irrespective of whether they are attached to kinetochores [3, 17] and concentrates near spindle poles at metaphase [3, 10, 18]. In K5I-resistant cell lines (KIRCs), Kif15 redistributes to non-kinetochore microtubules while microtubule-bound levels of active Eg5 are reduced [16, 17]. These localization patterns may indicate that Kif15 can only produce forces sufficient to drive spindle assembly when it is bound to non-kinetochore microtubules in an orientation-dependent manner. Kinetochore microtubules are predominantly parallel-oriented [19], whereas interpolar microtubules are of mixed polarity [20]. Redistribution of Kif15 to non-kinetochore microtubules may lead to significant force production when microtubules are anti-parallel, similar to Eg5.

Elegant biophysical studies have demonstrated that tetrameric Eg5 is optimally designed to drive spindle assembly [2, 21, 22, 23, 24, 25]. Eg5 only slides anti-parallel microtubules apart [2]. Single molecule and stopped flow experiments have shown that Eg5 resides primarily in a two-head bound state [21], and its catalytic cycle is limited by ATP hydrolysis rather than product release [22]. These features and a second non-motor microtubule-binding site bias Eg5 to remain attached to microtubules [24]. Furthermore, Eg5's mechanochemical cycle makes force generation scale linearly with motor number within an anti-parallel microtubule overlap [25].

By comparison, our understanding of Kif15 is limited. Some work suggests that Kif15 is tetrameric [26], leading to speculation that Kif15 promotes spindle assembly through a mechanism similar to Eg5, while our previous studies indicate that Kif15 is dimeric [16, 27]. As a homodimer, Kif15 can crosslink two microtubules through its motor domains and a second microtubule-binding site (Coil-1) within its coiled-coil stalk [27]. This crosslinking activity enables Kif15 to slide microtubules apart in vitro [27], although the microtubule orientation requirement for this activity is unknown.

Here, we investigate the activity of Kif15 on single microtubules and within microtubule bundles of different filament arrangements. We analyze constructs including full Kif15, a truncated Kif15 motor that does not include the Coil-2 inhibitory domain but includes the non-motor microtubule binding domain Coil-1 (N700), and the isolated microtubule binding domain (Coil-1) (Figure 2.2A). Single molecule optical tweezers and fluorescence experiments confirm that Kif15 acts as a dimer, takes a large percentage of backward steps, and that Coil-1 sustains forces higher than motor stall. These properties permit build-up of mechanical strain in the microtubule system through forward progress of the motor heads and concomitant resistance or relaxation by Coil-1 rupturing and back stepping. We further show that concerted movement occurs exclusively in anti-parallel microtubules. A stochastic simulation of microtubule sliding by Kif15 reveals the mechanism by which Coil-1 regulates strain build-up. Our work provides insight into how Kif15 gener-

ates forces that drive spindle assembly and has implications for the interplay between Eg5 and Kif15 within the spindle.

2.3 Results

2.3.1 Oligomerization state of Kif15

We used the baculovirus expression system to produce and purify Kif15 motor constructs (Kif15 and N700) with a C-terminal GFP-His6-tag (Figure 2.2B, inset) [27]. Confirmation of the motor's oligomerization state was necessary to form the foundation of a mechanism regarding Kif15's ability to generate force during spindle assembly. Single molecule photobleaching of individual motors occurred in two steps (Methods; Figure 2.1). This indicates that our construct is a dimer, which agrees with previous rigorous analysis in solution and when expressed in cells [16, 27, 28].

2.3.2 N700 Generates Force at Single Molecule Level

To evaluate the force generation capabilities of Kif15 and N700, single molecule bead motility assays using optical tweezers were performed (Figure 2.2B; Methods) [29]. N700, which includes the motor, stalk, and Coil-1 [27], moved robustly, permitting evaluation of motor characteristics such as stall force, step size, backward step probability, and dwell times. Full length Kif15, containing a C-terminal inhibitory domain (Coil-2) [27], moved much less frequently, prompting rigorous analysis of N700.

N700 exhibited a higher frequency of motility events compared to kinesin-1, and traces did not reach a plateauing stall but rather fell off abruptly, similar to sawtooth patterns generated by Eg5 [23]. Its stall force was $3.0 \text{ pN} \pm 0.6 \text{ pN}$ (avg \pm std, N=102; Figure 2.2C), which is similar to that of Kif15 (see below). N700 took approximately 8 nm steps (size of a tubulin dimer), though some variability was observed (Figure 2.2D). Backward stepping was observed with a 32% frequency, well above that of kinesin-1 [29, 30, 31].

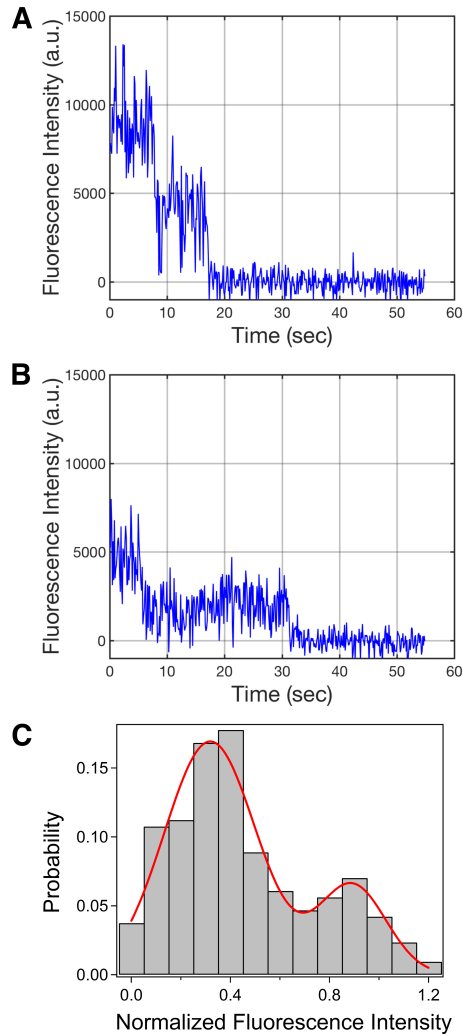


Figure 2.1: Oligomerization State of FL-Kif15. The oligomerization state of FL-Kif15-GFP was confirmed to be a dimer through single molecule photobleaching. (A) and (B) are representative fluorescence intensity traces versus time in seconds of a single FL-Kif15-GFP molecule non-specifically adsorbed to an etched coverslip showing sequential photobleaching in two steps. (C) shows a normalized fluorescence intensity distribution of the single FL-Kif15-GFP molecules. The two peaks indicate there are primarily two steps of photobleaching, which coincides with the construct being a dimer.

While the vast majority of step sizes are 8 nm, a small population (20%) of 16 nm forward steps were recorded (blue and green constrained fits in Figure 2.2D) that are likely to be unresolvable rapid 8 nm steps in succession. N700 had 2.7 s dwell times (Figure 2.2E).

N700 (attached to a bead) moved readily in an unloaded motility assay. Its velocity was $75.8 \text{ nm s}^{-1} \pm 41 \text{ nm s}^{-1}$ (N=67; Figure 2.2F), which is similar to previous measurements

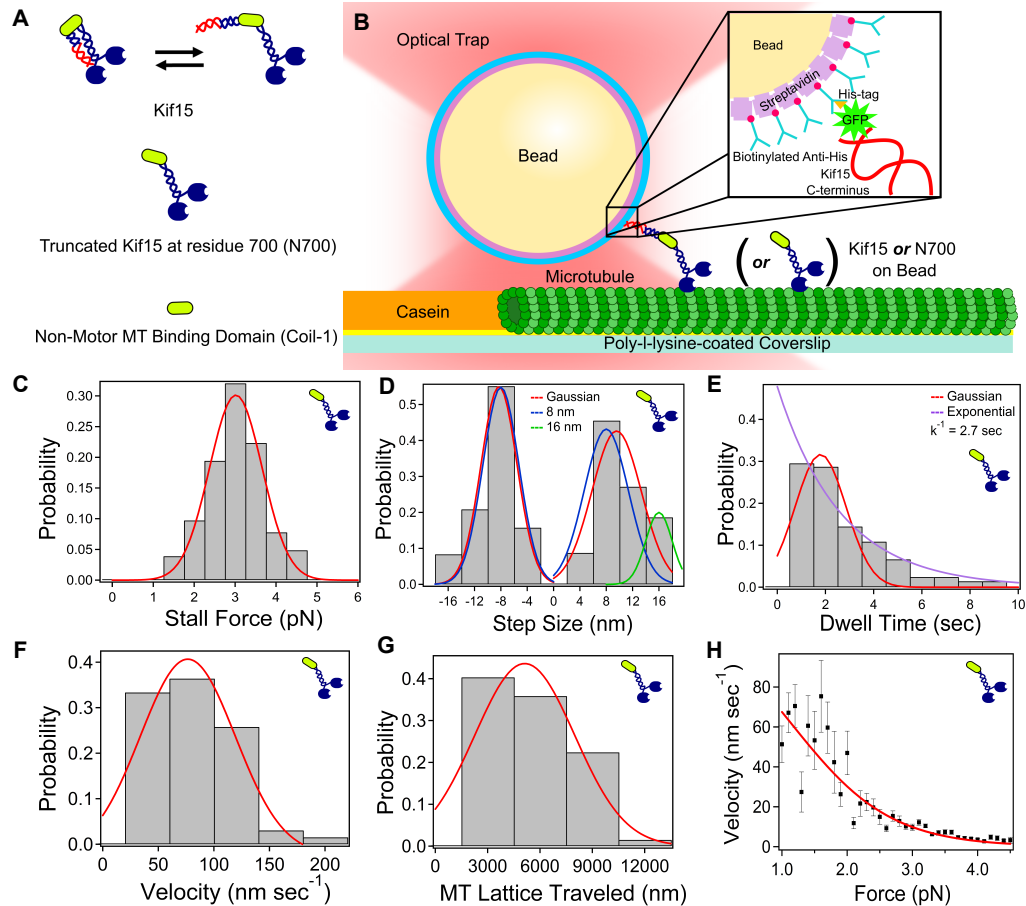


Figure 2.2: N700 Motility Assay. (A) Constructs studied: Kif15, N700, Coil-1. (B) Single molecule motility assay (Methods). (C) N700 stall force, averaging $3.0 \text{ pN} \pm 0.6 \text{ pN}$ ($N=102$), which is very similar to Kif15. (D) Step size distribution, averaging $9.6 \text{ nm} \pm 3.8 \text{ nm}$ ($N=473$, forward) and $8.3 \text{ nm} \pm 2.7 \text{ nm}$ ($N=230$, backward). Blue and green: 8 nm and 16 nm constrained fits. (E) Dwell time between steps averaged $1.8 \text{ sec} \pm 1.1 \text{ sec}$. Decay constant (exponential fit, red) is 2.7 sec. (F) Unloaded velocity measured via video tracking was found to be $75.8 \text{ nm s}^{-1} \pm 41 \text{ nm s}^{-1}$ ($N=67$). (G) N700 processivity was measured via video tracking the run length as $5120 \text{ nm} \pm 2900 \text{ nm}$, which is limited by microtubule length ($N=67$). (H) Force-velocity curve. Solid line: fit with a three-state kinetic model (Table 2.1). Error bars: SEM.

of Eg5 [23] and fluorescence velocity measurements of N700 and Kif15 [26, 27]. The average run length was $5120 \text{ nm} \pm 2900 \text{ nm}$ ($N=67$, Figure 2.2G). The spread is due to the underlying microtubule length, and values up to $12 \mu\text{m}$ were measured. Long commitments of Kif15 to motility have been observed previously [26, 27]. Upon reaching the end of the microtubule, N700 released 64% of the time. It also has the ability to switch microtubule

tracks, as shown previously, but the proposed structure was a tetramer [26]. Instead, N700 can switch tracks likely via its ability to rapidly recommit to motility, as shown by its high run frequency, along with Coil-1 that facilitates attachment and can keep an unbound motor from diffusing away (see below).

2.3.3 Force-Velocity Analysis of N700

To parameterize the mechanistic underpinnings of Kif15 behavior, a force-velocity curve was generated for N700 (Figure 2.2H; Methods) [32, 33, 34], and was fit with a three-state kinetic model of the form [23, 34]

$$v(F) = \frac{\delta_1 k_1 k_2 k_3 [ATP]}{k_1(k_2 + k_3)[ATP] + k_3(k_2 + k_{-1})} \quad (2.1)$$

with the force-dependent rate of the mechanochemical cycle

$$k_2 = k_2^0 e^{-F \delta_2 / (k_B T)}. \quad (2.2)$$

Here, v is the motor velocity under an applied force F ; $\delta_1 = 8.2$ nm is the average kinesin step size; k_1 and k_{-1} are ATP binding and unbinding rates (globally fit from [23]); k_2^0 is the unloaded mechanical rate; k_3 is the ATP hydrolysis rate; $k_B T$ ($T = 300$ K) is thermal energy; and δ_2 represents the force sensitivity of the three-state model, where larger values indicate a more force-sensitive motor [34]. The measured and fitted parameters for kinesin-1 [34], Eg5 [23], N700, and Kif15 are shown in Table 2.1, where δ_1 , k_1 , and k_{-1} were held constant. Eg5 and N700 unloaded velocities are similar, but N700 is more processive than Eg5, potentially due to the N700's ability to recommit to motility upon unbinding from the microtubule. The force sensitivity δ_2 is smaller for Eg5 (1.9 nm) than kinesin-1, N700, and Kif15 (4-6 nm). Eg5 has a proline in the middle of the neck linker, resulting in a shorter cover-neck bundle (force generating element) compared to kinesin-1 or Kif15, agreeing with its shorter δ_2 [34]. These parameters dictate Kif15's single molecule and ensemble-

level force generation capacity (see modeling results).

Construct	Unloaded Velocity (nm s ⁻¹)	Run Length (nm)	Stall Force (pN)	Three-State Model					
				k ₁ (μM ⁻¹ s ⁻¹)	k ₋₁ (s ⁻¹)	k ₂ ⁰ (s ⁻¹)	k ₃ (s ⁻¹)	δ ₂ (nm)	v _{max} (nm s ⁻¹)
Kinesin-1[34]	671 ± 21	1370 ± 287	4.92 ± 0.08	2	120	12,900	76.86	5.50	630
Eg5[23, 24]	96 ± 2	67 ± 7	1.5-7*	0.89	10	86	13.5	1.9	94
N700	76 ± 41	5120 ± 2900	3.0 ± 0.6	2	120	72.2	15.1	5.4	101
Kif15	n/m	n/m	2.7 ± 1.0	2	120	88.1	16.2	4.1	111

Table 2.1: **Three-State Kinetic Model for Kif15**. Kinesin-1 and Eg5 values were added for comparison. n/m: not measured. *Range of values reported.

2.3.4 Kif15 and N700 Stall at 3 pN

Interestingly, Kif15 is much slower than N700 and has a lower run frequency, or number of run events (walk until maximum force is reached before returning to the trap center) per time, on average 1.2 and 10 runs per 100 sec for Kif15 and N700, respectively (based on run events from raw force/displacement data). This suggests that Coil-2 in Kif15 plays a regulatory role, a feature not fully replicated in the trapped bead assay. Kif15 also shows step size variability in the distribution but shows 8 nm steps near the stall force (Figure 2.3). Kif15's stall force is very similar to N700 (Figure 2.3C). Step size distributions (Figure 2.3D) also contain 8 nm (blue) and 16 nm (green; 10% of forward and 20% of backward steps) constrained fits.

Unlike N700, Kif15 unloaded motility on single microtubules was rare. Although Kif15 coated beads bound microtubules, they did not readily move, making it difficult to obtain unloaded measurements. This may be because both Coil-1 and the motor domains bind to the microtubule simultaneously, making motility dependent on whether the motor heads could produce enough force to displace Coil-1 (see below). When motile, traces resembled those of N700 and Eg5. Notably, Kif15 moves processively even with the inhibitory Coil-2 domain present. This could be an effect of the GFP-tag or close association of the C-terminus to the bead, both of which could sequester Coil-2 from association with the motor heads.

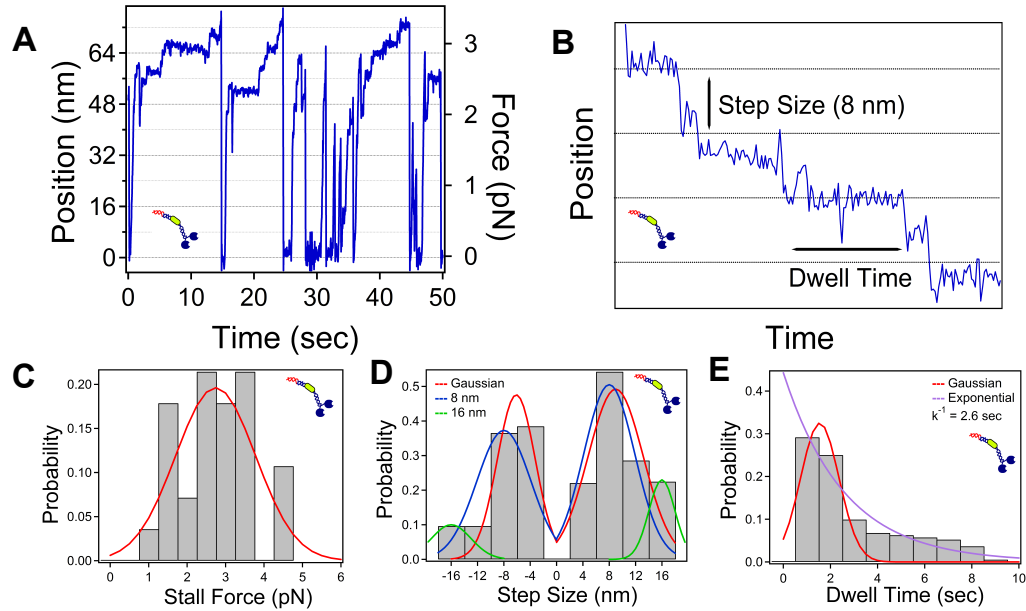


Figure 2.3: **Kif15 Motility Assay.** (A) Example Kif15 motility trace. (B) Example of 8 nm stepping used for step size and dwell time analysis. (C) Stall force histogram, averaging $2.7 \text{ pN} \pm 1.0 \text{ pN}$ ($N=27$). (D) Step size, averaging $8.9 \text{ nm} \pm 4.1 \text{ nm}$ ($N=118$, forward) and $6.1 \text{ nm} \pm 2.9 \text{ nm}$ ($N=52$, backward). 8 nm (blue) and 16 nm (green) constrained fits. (E) Dwell time, averaging $1.5 \text{ sec} \pm 0.8 \text{ sec}$. Decay constant (exponential fit, purple) is 2.6 sec.

2.3.5 Coil-1 Resists Forces Greater than Stall

We investigated the Coil-1/microtubule interaction, which would be critical in defining motor function. A Coil-1 rupture force below the stall force implies that motor heads walking along a microtubule would easily rupture Coil-1 bound to an adjacent microtubule, facilitating isolated motor movement with little resistance. A rupture force higher than stall would anchor Coil-1 to the microtubule while the crosslinked motor heads walk along the other, permitting productive, efficient, and collective force build-up within the bundle and concomitant microtubule transport.

We evaluated the strength of the Coil-1/microtubule interaction by measuring the time for the bond to rupture at a load determined by the necessary displacement to fully elongate the DNA tether (Figure 2.4; Methods). The lifetime distribution was bimodal, which averaged $5.6 \text{ sec} \pm 1.6 \text{ sec}$ and $24.8 \text{ sec} \pm 7.9 \text{ sec}$, respectively ($N=109$; Figure 2.4B). This

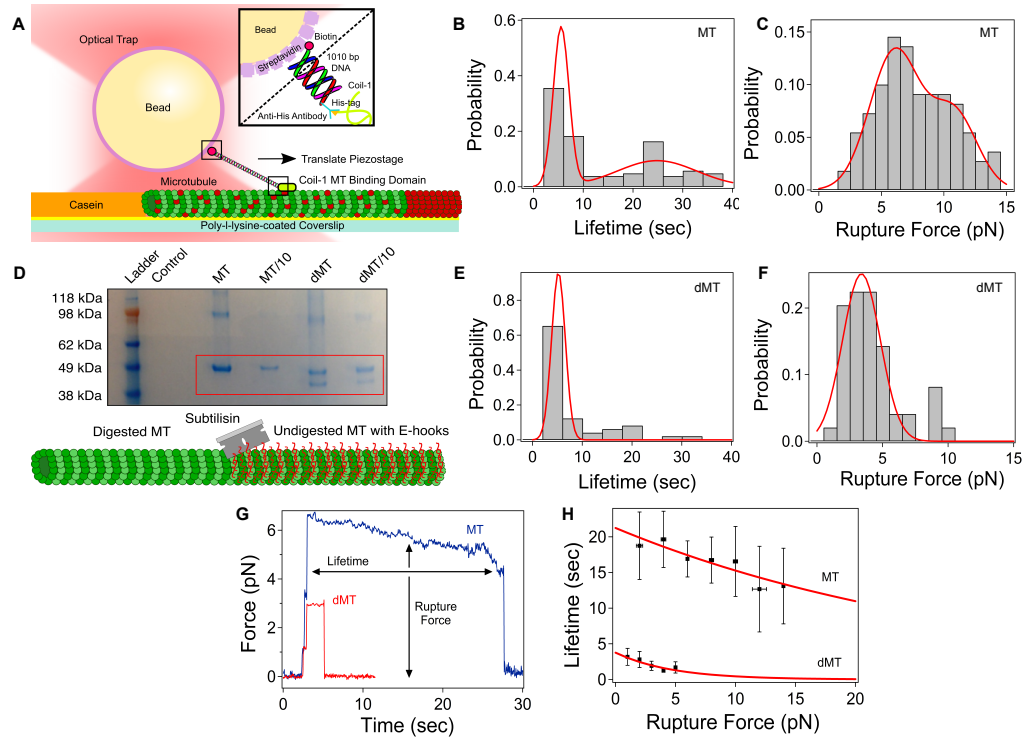


Figure 2.4: Coil-1 Binding Assay. (A) Assay design (Methods). (B) Coil-1/microtubule lifetime distribution, averaging $5.6 \text{ sec} \pm 1.6 \text{ sec}$ and $24.8 \pm 7.9 \text{ sec}$ ($N=109$) (C) Force at rapture, averaging $6.1 \text{ pN} \pm 2.0 \text{ pN}$ and $10.81 \text{ pN} \pm 1.8 \text{ pN}$ ($N=109$). (D) E-hook digestion confirmation using SDS-PAGE through separation of alpha and beta tubulin bands (ladder, control (sample buffer and water), microtubules (stock and 10x diluted), digested microtubules (stock and 10x diluted)). (E) Coil-1/digested microtubule lifetime, averaging $5.2 \text{ sec} \pm 1.4 \text{ sec}$ ($N=49$), is comparable to the lower value for normal microtubule (panel B). (F) Digested microtubule rapture force, averaging $3.4 \text{ pN} \pm 1.4 \text{ pN}$ ($N=49$). (G) Example raptures on normal (blue) and digested microtubules (red) (H) Coil-1 lifetime versus rapture force on normal ($R^2 = 0.77$) and digested microtubule ($R^2 = 0.68$). Error bars: SEM.

potentially reflects binding of Coil-1 to the microtubule's C-terminal tail (termed E-hook) or to the microtubule lattice. In both cases, the rapture forces are higher than the 3 pN stall force (Figure 2.4C). The average lifetime is long relative to the dwell times measured for Kif15, suggesting that Kif15 may be able to generate force in microtubule bundles. Interestingly, a significant number of rapture traces show structured motion toward the trap center before rapture (Figure 2.4G blue and Figure 2.5). The transitions appear discrete with dwells in between (Figure 2.5, insets). This structure suggests that Coil-1 may jump to the next available E-hook to readjust its position and maintain the high level of resistance

necessary for force generation.

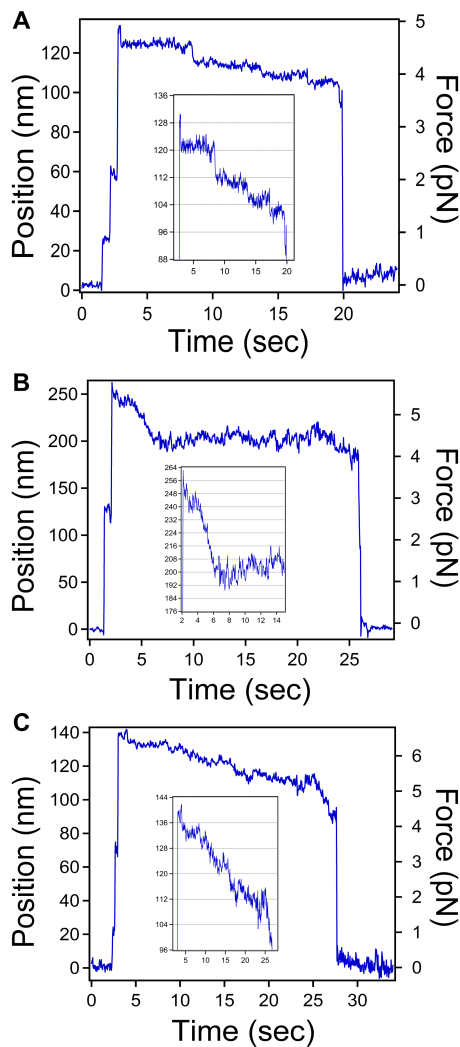


Figure 2.5: **Structured Movement of Coil-1 Under Force.** Figures A-C are examples of Coil-1 rupture traces that exhibit structured movement while Coil-1 is under tension. The insets reveal discrete transitions while Coil-1 is being pulled, which may potentially be due to the ability of Coil-1 to readjust its position and accommodate for the induced force by binding to the next sequential E-hook position. Lines at 8 nm periodicity are provided as a guide.

We further investigated the role of the negatively-charged E-hook by cleaving it from microtubules with subtilisin. Digested microtubules were confirmed by fractionation of α - and β -tubulin bands in SDS-PAGE (Figure 2.4D) [35]. Rupture measurements with digested microtubules revealed a reduced lifetime ($5.2 \text{ sec} \pm 1.4 \text{ sec}$, $N=49$; Figure 2.4E), and rupture force ($3.4 \text{ pN} \pm 1.4 \text{ pN}$, $N=49$; Figure 2.4F). The rupture trace on a digested

microtubule (Figure 3G, red) was also noticeably flat compared to normal microtubules (Figure 2.4G, blue). The difference may be due to the lack of available E-hooks to rescue binding once the first binding event fails. The marked lifetime decrease under a given rupture force (Figure 2.4H) also supports that the E-hook plays a substantial, likely electrostatic, role in binding Coil-1 to microtubules. The dependence on lifetime for Coil-1 on microtubules and digested microtubules was fit to an exponential based on the Bell model [36], which describes the force dependence of bond reaction rates (Figure 2.4H). Coil-1 lifetime on digested microtubules falls off quickly with increased force in contrast to the relatively flat dependence for native microtubules, revealing the E-hook's significance in the interaction.

Under physiological conditions, Kif15 targets kinetochore microtubules that contain parallel microtubules [17]. However, in KIRCs, Kif15 also binds interpolar microtubules that are oriented in anti-parallel [16, 17]. Thus, Kif15 may somehow discriminate and perform differently between bundle orientations. For example, if Kif15, being a plus end directed motor, can slide anti-parallel microtubules apart, then the Coil-1/microtubule interaction should be strong enough to sustain load as the motor walks. Conversely, if Kif15 transits through parallel bundles, then a weaker Coil-1/microtubule would be advantageous in facilitating motor transport towards the plus end.

To test Coil-1's orientation sensing ability, a directional pulling assay was performed, similar to the assay in Figure 2.4A, except using polarity-marked microtubules (Methods) [37]. After the tether was formed in DIC mode, fluorescence visualization unambiguously determined the microtubule orientation. The piezostage was then moved towards the desired microtubule end, and the system was held at a fixed force. The average rupture forces for pulling toward the plus end ($7.7 \text{ pN} \pm 2.6 \text{ pN}$, $N=26$), and the minus end ($7.8 \text{ pN} \pm 3.8 \text{ pN}$, $N=30$) were similar, likely due to the E-hook's flexibility and reorientation ability. Thus, Coil-1 should respond similarly when Kif15s walk between microtubules in parallel or anti-parallel.

2.3.6 Kif15 Generates Force in Anti-Parallel Microtubule Bundles

An *in vitro* optical trapping assay was developed to observe Kif15 behavior in microtubule bundles, a more native environment compared to the bead assay (Figure 2.6A; Methods, adopted from Shimamoto *et al.* [25]). After finding a bundle, its orientation (parallel vs. anti-parallel) was determined through fluorescence visualization relative to the known fixed trap position. Since the streptavidin bead only binds the biotinylated tubulin contained in the minus end microtubule seed, the trap center is located at the cargo microtubule minus end (Figure 2.6B).

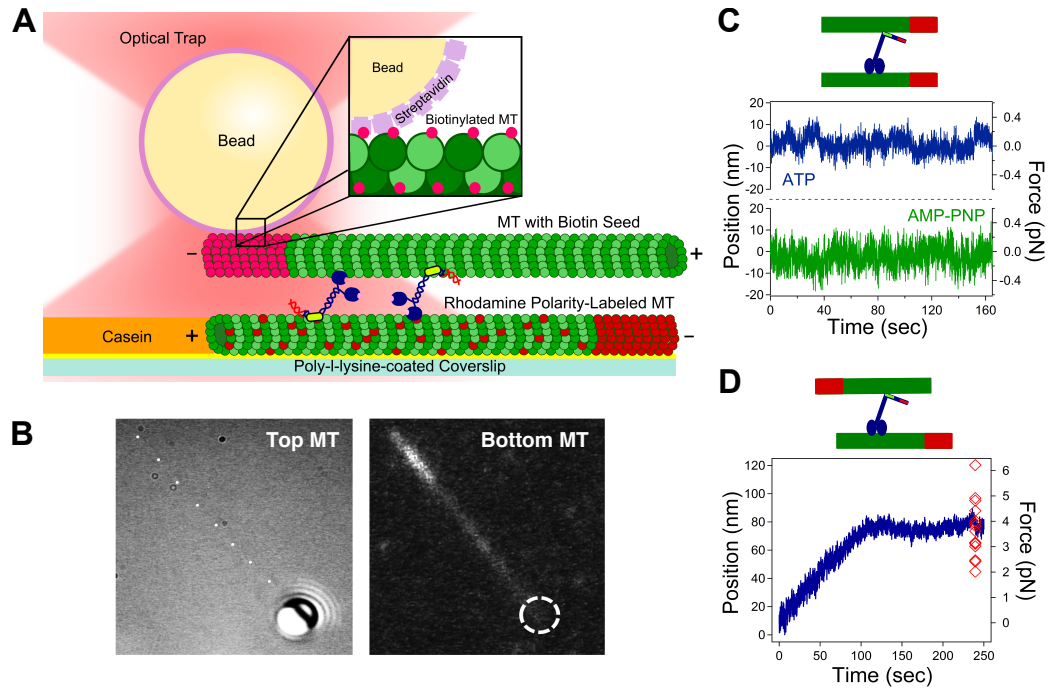


Figure 2.6: **Microtubule Binding Assay.** (A) Assay schematic (Methods). (B) Top microtubule (DIC) with streptavidin bead bound to the biotinylated minus end, bundled to the bottom microtubule (fluorescence). Dashed circle denotes bead location. (C) Parallel bundles yielded baseline force generation. With AMPPNP, only thermal noise is present. Kif15 has a 72% parallel bundle bias (N=43). (D) Anti-parallel bundles yielded a force ramp and plateau at a stall force similar to a single motor (N=17). Red diamonds: individual stall forces.

Bundles were generated in the presence of ~ 20 nM Kif15. Parallel bundle traces do not show much force generation but rather exhibit wandering along the baseline with motors

antagonizing each other (N=43, Figure 2.6C). To determine whether this baseline displacement was due to the motors or thermal fluctuations, a control was performed with AMPPNP that locks the motors in place. The trace with ATP present shows distinctive motion in comparison to the AMPPNP trace, revealing that this frustrated motion is due to antagonizing motors (Figure 2.6C). Anti-parallel bundle traces exhibit a ramp where the motors begin generating force until they stall out against the trap and plateau (Figure 2.6D). This is similar to Eg5 in microtubule overlaps [25], except the plateau force here remains close to stall forces for individual motors ($3.7 \text{ pN} \pm 1.0 \text{ pN}$, N=17). The corresponding translation velocity is $0.44 \text{ nm s}^{-1} \pm 0.19 \text{ nm s}^{-1}$ (N=17). Also, only 28% of the bundles were anti-parallel in orientation, while the other 72% were parallel. This observation is consistent with Drechsler *et al.* who showed that Kif15 has a 70% bundling bias for parallel microtubules in the presence of ATP [38].

The same bundling experiment was performed with N700 (Figure 2.7), behaving similarly to Kif15. There is a 69% bundling bias for the parallel orientation that lacks force generation, whereas in anti-parallel bundles, the force profile shows a ramp followed by a plateau, as with Kif15. Since Kif15 and N700 exhibit similar capabilities, Coil-1's microtubule bundling role was further investigated through two experiments: (1) bundling with a construct lacking Coil-1 (N420) and (2) with N700 (including Coil-1) but with digested microtubules (Figure 2.8). Microtubules did not bundle in both cases. Therefore, the Coil-1/E-hook interaction is necessary for bundle formation by Kif15. Together, these results reveal that Kif15 can generate force between anti-parallel microtubules while net progress in parallel microtubules is minimal with frustrated oscillations around baseline.

2.3.7 Kif15 Contains a Force-Feedback Mechanism

The low plateau force in anti-parallel bundles indicates that Kif15 may have a self-governing mechanism that limits its force generating capabilities in large numbers. To test this idea, a combined microtubule gliding/optical tweezers assay was developed (see Meth-

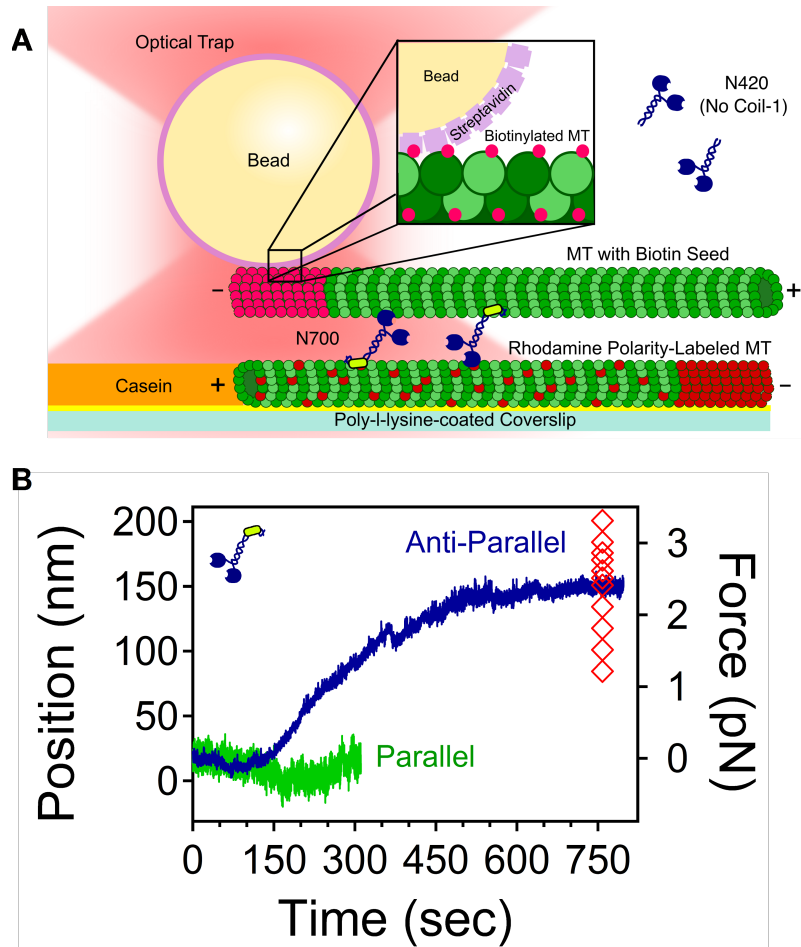


Figure 2.7: **N700 Binding Assay.** (A) Schematic of N700 bundle assay that is assembled in the same manner as the Kif15 bundle assay in Figure 2.6. This assay was also performed with N420 with results shown in Figure 2.8. (B) N700 exhibits a ramp/plateau pattern (representative trace in blue) when sliding anti-parallel bundles with an average plateau force of $2.4 \text{ pN} \pm 0.6 \text{ pN}$ (red diamonds are individual plateau forces, $N=11$). N700 does not generate force in parallel bundles (representative trace, green, $N=25$) yet exhibits a 69% bundling bias for this orientation. These results are consistent with Kif15 in bundles.

ods) to compare Kif15, Eg5 (Figure 2.9) and N700 (Figure 2.10). Eg5 behaves similarly to what was found previously, where many motors generate a large amount of force (Figure 2.9B, blue) [25]. Force plateaus of 20-30 pN were observed ($N=8$), where some traces reach the stall, fall back briefly with jagged trajectories, and continue to glide persistently. In contrast, Kif15 ($N=8$) behaves similarly as at very low concentration in the bundle assay. There is a slow and smooth force ramp that finally plateaus minutes later at 5-6 pN. N700

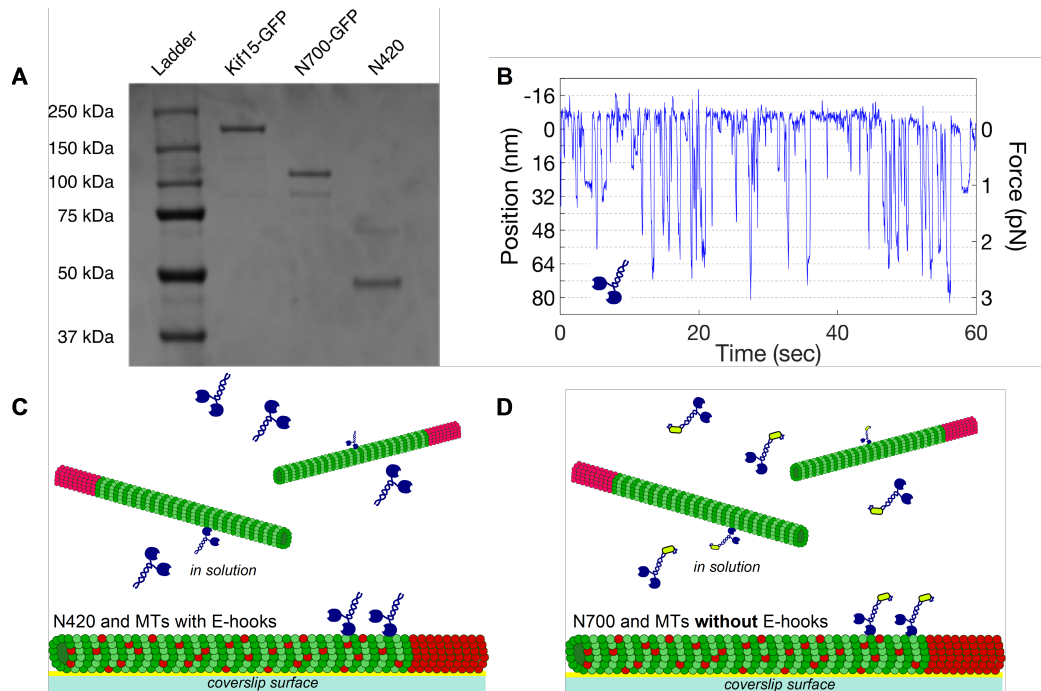


Figure 2.8: Coil-1/E-hook Interaction Needed for Bundling. The bundle assay was repeated with N420 which lacks Coil-1. (A) SDS-PAGE gel of insect purified Kif15-GFP, insect purified N700-GFP, and bacterially purified N420. Sizes of Kif15 and N700 with GFP at the C-terminus are consistent with [27]. (B) Control experiment to show that N420 is active at the single molecule level attached to a bead. The motor reaches a maximum force of 3pN before detaching from the microtubule, returning to the trap center, and starting to walking again. (C) No bundles were formed when N420 was present as 0/100 streptavidin beads bound biotinylated microtubules near the surface. (D) The bundle experiment was repeated with N700 but with digested polarity marked microtubules (rhodamine and biotin seed microtubules). As with N420, no bundles were formed as 0/100 streptavidin beads bound biotinylated microtubules near the surface. These experiments show that the Coil-1/E-hook interaction is necessary for microtubule bundling by Kif15.

behaved similarly to Kif15 (Figure 2.9B).

Due to the non-specific nature of motor binding to the glass surface, both the motor heads and Coil-1 can help recruit microtubules to the surface to subsequently glide. The same trace patterns between this gliding assay and the bundle assay reveal that the distributions of motor orientations are likely similar.

To better understand the plateauing behavior, we developed a stochastic model of microtubule gliding by Kif15 (Methods). The trap stiffness, 3-state force-velocity relation,

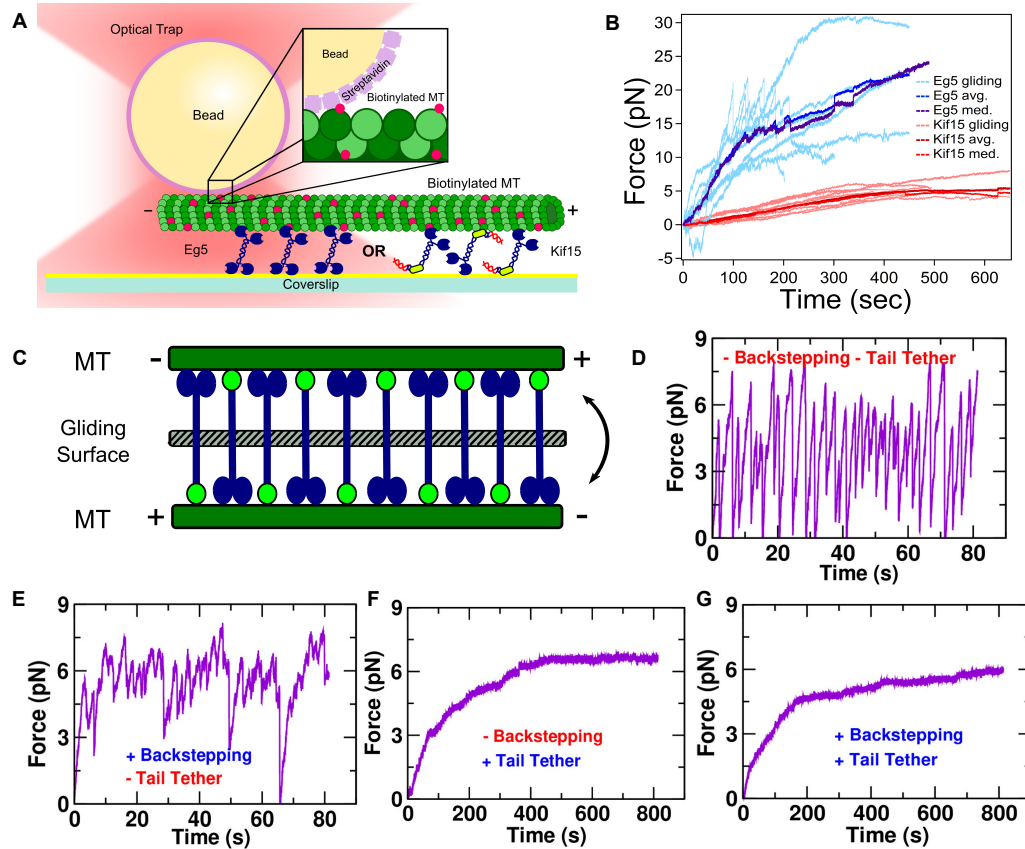


Figure 2.9: **Combined Microtubule Gliding/Optical Tweezer Assay.** (A) Assay schematic (Methods). (B) Loading traces of gliding microtubules on Eg5 (blue, $N=8$) and Kif15 (red, $N=8$). Eg5 generates force, sliding faster ($0.1 \text{ pN/sec} \pm 0.02 \text{ pN/sec}$) than Kif15 ($0.01 \text{ pN/sec} \pm 0.006 \text{ pN/sec}$). Kif15 behaves similarly as in anti-parallel bundles (Figure 4D). (C) Model schematic. Simulation results can be interpreted as a gliding microtubule or anti-parallel bundle (Results). (D-G) Simulated sliding with different model components (Methods). Simulated system contains 5 Kif15 motors. In (F,G), 5 tethers are present with Coil-1 binding to the microtubule at 6.1 pN rupture force while the other end is stationary. Only with tethers are slow ramping and reduced force fluctuation observed.

Kif15 stall force, backstep probability, and tail (Coil-1) rupture force were adopted from experimental values. Model parameters unavailable from experiment were adjusted so that resulting behaviors match semi-quantitatively with experiment. We also incorporated “tethered tails” whose opposite motor domain is attached to the substrate and immobile. This mimics the situation where Coil-1 is bound to the microtubule in the gliding assay (Figure 2.9A). Such scenarios may also arise in microtubule bundles as motor domains waiting for ATP binding are in rigor states (Figure 2.9C).

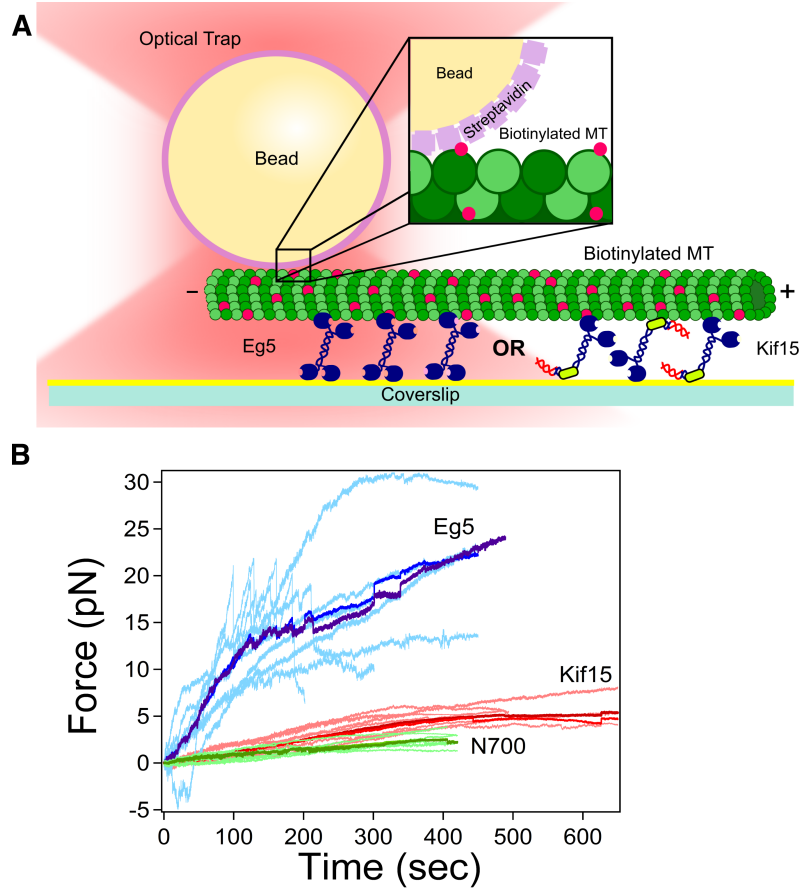


Figure 2.10: **N700 Combined Microtubule Gliding/Optical Tweezer Assay.** (A) Schematic of gliding assay that is assembled in the same manner as the Kif15 and Eg5 gliding assay in Figure 2.9. (B) N700 exhibits a ramp/plateau pattern (green, N=7) in the same manner as Kif15 (red). The plateau force is somewhat smaller than that of Kif15; however, it is consistent with the N700 bundle plateau force in Figure 2.7. In the same way, the plateau force of Kif15 in this gliding assay is also consistent with its bundle assay plateau force in Figure 2.6. It is possible that the GFP on the C-terminus is interfering with Coil-1 binding and not allowing for as much force generation as Kif15. The median of the traces is shown in dark green.

We first ran the simulation without backstepping and tail rupturing. The microtubule trajectory followed a sawtooth pattern caused by walking until stall, detachment, and return to the origin (Figure 2.9D). With backstepping, the force rapidly plateaued, indicating a balance between forward and backward steps was established (Figure 2.9E). The rapid rise and noisy force trace qualitatively correspond to Eg5 where both ends of the motor walk (hence low chance of forming a tether), which also can backstep (Figure 2.9B) [24]. On

the other hand, when tail rupturing was activated, the force ramped more slowly, and the profile became smoother (Figure 2.9F,G). For this, backstepping was not essential, but it lowered the plateau force slightly due to the additional force relaxation (Figure 2.9F,G).

These results provide evidence for Kif15 having a force-feedback mechanism that limits force generation and fluctuation. Tethering by Coil-1 is essential for this feedback. Coil-1 provides support as motor domains walk and transport microtubules. For motor domains awaiting ATP, the corresponding Coil-1, with its high rupture force, serves as a tether that limits microtubule gliding, manifesting a force plateau on the bead.

2.4 Discussion

In human cells, it is unknown how Kif15 generates centrosome separation forces necessary to drive spindle assembly [13, 17]. Since Eg5 promotes spindle assembly through anti-parallel microtubule-microtubule sliding [2], the prevailing hypothesis is that Kif15 produces outward force through a similar mechanism, prompting several models [13, 26, 27]. One model posits that Kif15 may exist as a tetramer in solution, and thus is Eg5-like [26]. However, our measurements reported here (Figure 2.1) and in our previous works [16, 27] show that our Kif15 constructs are homodimers in solution and in cells. A recent study from Brouwers *et al.* supports that Kif15 is a dimer in solution [28]. A second model suggests that Kif15 may complex with TPX2, enabling microtubule-microtubule crosslinking and sliding [13]. Recognizing that Kif15 contains Coil-1, we previously proposed a third model wherein Kif15 dimers drive microtubule-microtubule sliding [27] similarly to fly kinesin-14 (Ncd) [39] and yeast kinesin-8 (Kip3) [40]. This is consistent with the finding that a minimal Kif15 construct (N700) drives microtubule-microtubule sliding [27]. Here, we show that non-truncated Kif15 also catalyzes microtubule-microtubule sliding when anti-parallel. In conjunction with our optical trapping data, our observations provide a biochemical explanation for how Kif15 promotes spindle assembly and yields insight into the functional relationship between Kif15 and Eg5 within the spindle.

In contrast to a single Eg5 tetramer that walks on both anti-parallel microtubules, Kif15 likely “runs in place” between two microtubules, based on Coil-1 having a rupture force at least two-fold greater than Kif15’s stall. Strong Coil-1/microtubule binding is likely electrostatic, as E-hook removal significantly reduces the strength of the interaction. In an anti-parallel bundle, Kif15 exerts force directed toward the minus end of each microtubule, regardless of whether its motor or Coil-1 domain is bound, causing the microtubules to slide apart (Figure 2.11). In the parallel case, a Kif15 motor head pushes a microtubule towards its minus end whereas Coil-1 pushes it to the plus end as its motor domain on the other microtubule walks, causing both microtubules to become locked (Figure 6). This model also mirrors the mechanism proposed for fly kinesin-14, a dimeric motor with a non-motor microtubule binding site on its tail [39, 41].

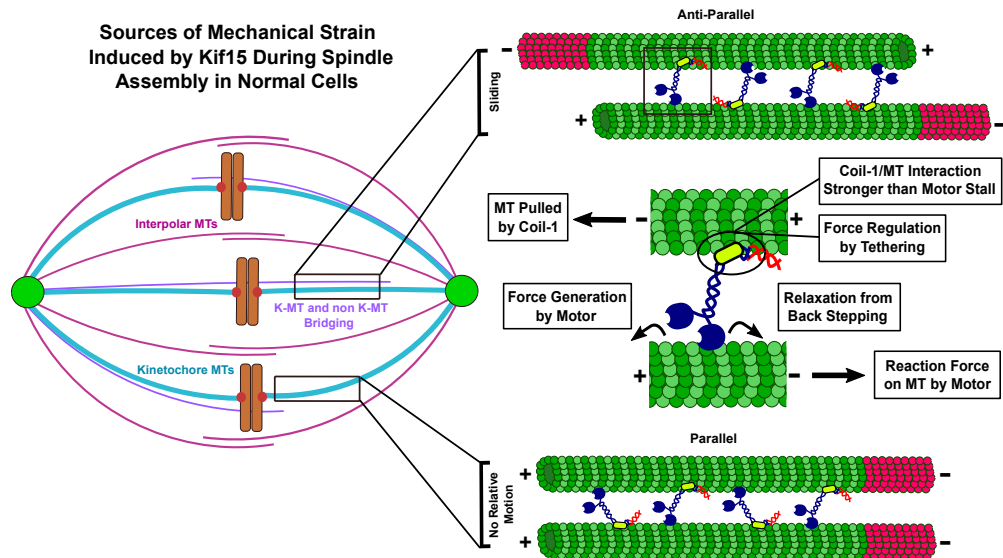


Figure 2.11: **Model for Kif15 Function in Microtubule Bundles.** Force generated by Kif15 transmits between microtubule bundles via Coil-1 and the motor head. In the anti-parallel case, the motors collectively slide microtubules apart. In the parallel case, motors yield no relative movement (Discussion).

We also found distinct regulation of force generation between anti-parallel microtubule bundles by Kif15. Force ramps gradually over a period that is much longer than individual motor dwell times to a plateau not significantly larger than the motor’s stall force. Further-

more, force fluctuation is much smaller than observed for Eg5 (Figure 2.9). Our simulation shows that force regulation by an ensemble of Kif15s is determined mainly by the tethering effect of Coil-1. Although backstepping contributes to force relaxation, its time scale is comparable to the forward stepping time; force fluctuates over a time scale comparable to the motility of individual motors (several seconds). Also, the force fluctuation amplitude is large since it is determined essentially by the motility and detachment of individual motors (Figure 2.9E). This is the case even with tail rupturing since unbinding of the motor domain occurs more quickly and at lower force. On the other hand, if the motor unbinds from the microtubule mainly via tail rupturing (a tethered case), the tethered tails serve as transient crosslinks between two microtubules, slowing down microtubule sliding and suppressing force fluctuation (Figure 2.9F,G). A modest level of rupture force is crucial since a very high tether rupture force would correspond to a static crosslink that prevents microtubule sliding.

Force regulation by an ensemble of Kif15 differs significantly from Eg5 [25]. Having motor domains on both ends, force regulation by an Eg5 ensemble occurs on a time scale comparable to that of individual motors. It is, perhaps, for this reason, that Eg5 and Kif15 differ in spindle assembly efficiency. In contrast to Eg5, Kif15 is poor at driving centrosome separation, even under conditions where the motor is overexpressed; spindles remain monopolar for long periods of time, potentially storing energy, and “pop open” when reaching a force threshold [13, 17]. The difference in force-producing behaviors of Eg5 and Kif15 also has implications for how the motors distribute within the metaphase spindle. Under normal conditions, Kif15 concentrates on kinetochore microtubules, whereas Eg5 accumulates on spindle microtubules indiscriminately. Ensembles of Eg5 can easily produce forces in excess of 6 pN within anti-parallel overlaps, with single molecules each generating ~ 1.5 pN [25]. Linear scaling of motors with force implies that small numbers (~ 4) of Eg5 motors can displace Kif15 molecules from the anti-parallel overlap, a force-feedback mechanism that may cause Eg5 and Kif15 to associate with distinct spindle

microtubule geometries [17].

What is the function(s) of Kif15 on kinetochore microtubules? In HeLa cells, Kif15 is required for spindles to remain bipolar at metaphase [13, 15]. Similarly, Kif15 slows K5I-triggered collapse of metaphase spindles in RPE-1 cells [42]. These data strongly suggest that Kif15 not only helps bundle microtubules but also somehow generates an outward-directed force within the spindle, even while restricted to kinetochore microtubules. Since Kif15 cannot generate net sliding forces within parallel bundles, we propose that Kif15 motors mechanically link non-kinetochore-microtubules to kinetochore microtubules and slide them apart only when anti-parallel (Figure 2.11). Near the centromere, such microtubules constitute “bridging fibers”, which link sister kinetochore-fibers and balance inter-kinetochore tension [43]. We speculate that mechanical coupling of non-kinetochore and kinetochore microtubules is more pervasive throughout the spindle, as Kif15 is uniformly distributed along kinetochore microtubules [17]. The distinct function of Kif15 in parallel kinetochore microtubules, its structural and mechanical differences from Eg5, and the jack-knifing effect [17] upon rescuing spindle assembly, demonstrate that Kif15 contributes uniquely to spindle dynamics.

In summary, dimeric Kif15 regulates force generation differently depending on microtubule orientation. Essential to its force-regulating capability is the fine physical balance between the motor head motility properties and the Coil-1/microtubule interaction. Physiologically, Kif15 localizes to kinetochore microtubules to aid in stability and regulate length through plus end tracking, as proposed elsewhere [38], as well as antagonize motor movement that only allows for subtle, well-regulated displacement, as shown here. Kif15 can rescue the function of inhibited Eg5 by utilizing Coil-1 in conjunction with its motor heads to build up mechanical strain and slide anti-parallel microtubules apart, building a bipolar spindle that is necessary for successful mitosis. This mechanism demonstrates the therapeutic importance of Kif15, whose inhibition in tandem with an Eg5 inhibitor could prove to be more effective in the clinic.

2.5 Materials and Methods

2.5.1 Molecular Biology and Baculovirus Construction

pET15-Kif15-Coil-1 was constructed as described previously [27]. pET15-Kif15-N420 was constructed by isothermal assembly. A PCR fragment encompassing Kif15 amino acids 1-420 was generated with Phusion DNA polymerase (Thermo) and assembled into pET15 (Novagen) restricted with *NdeI* and *XhoI*.

pFASTBAC1-Kif15-GFP (pRO1221) and pFASTBAC1-Kif15-N700-GFP (pRO1222) were constructed by 3 part isothermal assembly into the Bam H1 and PstI sites of pFASTBAC1 (ThermoFisher Scientific). Kif15 and GFP coding sequences were PCR amplified to include: 1) a (GGG)₂ linker in between Kif15 and a 3'-end-positioned GFP; and 2) a hexahistidine tag downstream of GFP. pRO1221 and pRO1222 were used with the Bac-to-Bac system (ThermoFisher Scientific) to create baculoviruses that express Kif15-FL-GFP-His6 and Kif15-N700-GFP-His6, respectively.

pFASTBAC-HTc-Eg5-WT was constructed as described previously [16]. The Eg5 coding region from pEGFP-C1-Eg5-WT was amplified and assembled into Sall-EcoRI-restricted pFASTBAC-HTc (ThermoFisher Scientific) by isothermal assembly. This was used with the Bac-to-Bac system (Invitrogen) to create baculoviruses that express His6-Eg5-WT.

2.5.2 Protein Expression and Purification

His₆-Kif15-N420 and His₆-Kif15-Coil-1 were expressed and purified in BL21DE3 cells as described previously [16, 27]. Both constructs were expressed with 0.4 mM IPTG for 4 hours. For purification, cells were pelleted and resuspended in lysis buffer (PNI [50 mM sodium phosphate, 500 mM NaCl, 20 mM imidazole], 5 mM β -mercaptoethanol, and 1% NP40, and protease inhibitors [1 mM phenylmethylsulfonyl fluoride, 1 mM benzamidine, and 10 μ g/mL each of leupeptin, pepstatin, and chymostatin]). All buffers to purify His₆-

Kif15-N420 additionally contained 50 μ M MgATP. Lysate was incubated with 1 mg/mL lysozyme for 30 minutes, sonicated, and clarified by centrifugation at 35,000 rpm for 1 hour in a Ti 45 rotor (Beckman). \sim 3 mL of Ni⁺⁺⁺-NTA agarose (Qiagen) was incubated with the supernatant for 1 hour at 4°C, and then washed with wash buffer (PNI, 5 mM β -ME, 10% glycerol). Protein was eluted with PNI, 5 mM β -ME, and 180 mM imidazole. His₆-Kif15-Coil-1 was desalted with a PD10 column (GE Healthcare) equilibrated with 10 mM K-HEPES, pH=7.7, 100 mM KCl, 1 mM DTT, and 20% sucrose. His₆-Kif15-N420 was subjected to size exclusion chromatography on a Superdex 200 column equilibrated in 10 mM K-HEPES, pH=7.7, 100 mM KCl, 1 mM DTT, and 0.1 mM MgATP. For both, peak fractions were pooled, aliquoted, frozen in liquid nitrogen, and stored at -80°C.

Kif15-FL-GFP-His₆, Kif15-N700-GFP-His₆, and His₆-Eg5-WT were expressed in Sf9 cells for 72 hours. For purification, cells were pelleted and resuspended in lysis buffer (PNI, 5 mM β -mercaptoethanol (β -ME), and 1% NP40, and protease inhibitors [1 mM phenylmethylsulfonyl fluoride, 1 mM benzamidine, and 10 μ g/ml each of leupeptin, pepstatin, and chymostatin]). Lysate was incubated on ice for 15 minutes, sonicated, and clarified by centrifugation at 35,000 rpm for 1 hour in a Ti 45 rotor (Beckman). \sim 2 ml of Ni⁺⁺⁺-NTA agarose (Qiagen) was incubated with the supernatant for 1 hour at 4°C, and then washed extensively with wash buffer (PNI, 5 mM β -ME, and 50 μ M MgATP). Protein was eluted with PNI, 5 mM β -ME, 0.1 mM MgATP, and 180 mM imidazole, and peak fractions subjected to desalting with a PD10 column (GE Healthcare) equilibrated in 10 mM K-HEPES, pH=7.7, 300 mM KCl, 1 mM DTT, and 0.1 mM MgATP. Protein concentrations were determined using Bradford assays and take into account that Kif15 exists as a dimer in solution and Eg5 exists as a tetramer in solution. Powdered sucrose was added to 20% w/v. Protein was aliquoted, frozen in liquid nitrogen, and stored at -80°C.

2.5.3 Microtubule Preparation

Tubulin (bovine, Cytoskeleton TL238) was reconstituted in 25 μL PEM80 buffer (80 mM PIPES (Sigma P-1851), 1 mM EGTA (Sigma E-4378), 4 mM MgCl_2 (Mallinckrodt H590), pH adjusted to 6.9 with KOH) supplemented with 1 mM GTP (Cytoskeleton BST06) and kept on ice. Tubulin from PurSolutions (bovine, 1001) was also used and reconstituted in the supplied polymerization buffer. 13 μL PEM104 buffer (104 mM PIPES, 1.3 mM EGTA, 6.3 mM MgCl_2 , pH adjusted to 6.9 with KOH), 2.2 μL 10 mM GTP, and 2.2 μL DMSO were mixed. 4.8 μL of 10 mg/mL tubulin were added to the mixture and allowed to incubate for 40 minutes at 37°C. Subsequently, 2 μL of stabilization solution (STAB, 38.6 μL PEM80, 0.5 μL 100 mM GTP, 4.7 μL 65 g/L NaN_3 (Sigma S-8032), 1.2 μL 10 mM Taxol (Cytoskeleton TXD01), 5 μL DMSO (Cytoskeleton)) was added to the stock microtubule solution at room temperature.

Digested microtubules were made by removing the C-terminal E-hook of microtubules with subtilisin. 7.5 μL of pre-formed microtubules were mixed with 0.75 μL of 20 μM subtilisin (Sigma P8038) and was allowed to incubate at 37°C for 40 minutes. To stop digestion, 0.8 μL of 20 mM PMSF (phenylmethanesulfonyl fluoride, Sigma P7626) in DMSO was added to the digested microtubule mixture. 2 μL of STAB solution was then added to the digested microtubules at room temperature.

Polarity-marked microtubules were prepared by making a brightly fluorescent microtubule seed and polymerizing dimmer tubulin from that nucleation point. The microtubule seed was formed using GMPCPP, a non-hydrolysable analog of GTP (Jena Bioscience NU-405L). Rhodamine-labeled tubulin (Cytoskeleton, TL590M) was used in different concentrations to denote the bright seed from the dimmer elongation. First, the seed was polymerized by mixing 13 μL PEM104, 2.2 μL 10 mM GMPCPP, 2.2 μL DMSO, 4 μL non-labeled tubulin (10 mg/mL), and 1 μL rhodamine-labeled tubulin (10 mg/mL). The seed mixture was incubated at 37°C and allowed to incubate for 40 minutes. The elongation solution was made by mixing 13 μL PEM104, 2.2 μL 10 mM GTP, 2.2 μL DMSO, 2 μL

non-labeled tubulin (10 mg/mL), and 1.5 μ L rhodamine-labeled tubulin (1 mg/mL). The elongation mixture was incubated at 37°C for 1 minute to ensure that the mixture was at least at room temperature. After a minute, 1.5 μ L of the seed mixture was added to the elongation mixture and allowed to incubate at 37°C for 40 minutes. Subsequently, 2 μ L of STAB solution was added to the polarity-marked microtubules at room temperature.

2.5.4 Microtubule Gliding Assays

Microtubule gliding assays for Kif15 were performed as described previously [16, 27]. Flow cells were constructed with double-stick tape, and motor was added at stock concentration (1.1 μ M Kif15; 0.88 μ M Eg5) for 3 minutes and X-rhodamine-labeled GMPCPP microtubules (1:9 labeled:unlabeled) at 300 nM tubulin in BRB80 for 3 minutes. Flow cells were washed between each addition with 3 volumes of BRB80, 50 mM KCl, 1 mM MgATP, and 500 μ g/mL casein. After the final addition, flow cells were washed with 3 volumes of BRB80, 50 mM KCl, 1 mM MgATP, 500 μ g/mL casein, and oxygen scavenging mix (200 μ g/mL glucose oxidase, 35 μ g/mL catalase, 25 mM glucose, 70 mM β -ME). Microtubule gliding was recorded at 5-s intervals by time-lapse microscopy.

Combined gliding and optical trapping assays were constructed in the same manner except 1:9 biotinylated microtubules were used in place of rhodamine microtubules and 1.25 μ m streptavidin beads (Spherotech) were added to the final buffer addition. Beads were trapped in solution and actively bound to the biotinylated microtubules for force measurement.

2.5.5 Bead Functionalization

Coil-1 was tethered to 0.44 μ m streptavidin polystyrene beads (Spherotech - SVP-05-10) via a 1,010 bp DNA linker functionalized with biotin and a terminal amine. The 1,010 bp DNA linkers were created using PCR and the M13mp18 plasmid template. All primers were ordered from Integrated DNA Technologies (IDT). One 5' biotinylated primer (for-

ward, 5'-biotin-TATTGCGTTTCCTCGGTTTC-3') and one 5' amine-functionalized primer (reverse, 5'-amine-TTGAAATACCGACCGTGTGA-3') were used with the M13mp18 template. After PCR, the amine-functionalized end of the tethers were crosslinked to anti-His tag antibody (GenScript - A00186-100) using sulfo-NHS/EDC chemistry. EDC (1-ethyl-3-(3-dimethylaminopropyl)carbodiimide hydrochloride, Thermo Scientific - 22980), Sulfo-NHS (N-hydroxysulfosuccinimide, Thermo Scientific - 24510), ethanolamine (Sigma - E9508), and PBS (1x, pH 7.4) were used in this reaction. The DNA linkers were then purified using Micro Bio-Spin 30 columns (Biorad). Streptavidin beads, DNA linker (33 ng/ μ L), and Coil-1 (1 nM) diluted in assay buffer (AB, 80 mM PIPES, 1 mM EGTA, 4 mM MgCl₂, 1 mM DTT, 20 μ M Taxol, 1 mg/mL casein, 1 mM ATP) were incubated together for 1 hour at 4°C on a rotator to create Coil-1 tethered beads.

Motor functionalized beads were created by binding the C-terminus of the motor to the bead via a His-tag linkage. 0.44 μ m streptavidin polystyrene beads (Spherotech - SVP-05-10) were incubated with 0.2 mg/mL biotinylated anti-His tag antibody (Qiagen - 34440) to create anti-His tag coated beads. The beads were washed with PBS (1x, pH 7.4) 4 times by centrifuging at 10,000 rpm for 6 minutes to remove any unreacted biotinylated anti-His. The beads were then incubated with 1 nM of motor diluted in AB for 1 hour at 4°C on a rotator in the presence of an oxygen scavenging system (5 mg/mL β -D-glucose (Sigma G8270), 0.25 mg/mL glucose oxidase (Sigma G2133), and 0.03 mg/mL catalase (Sigma C40)).

2.5.6 Single Molecule Optical Trapping Assays

A flow cell that holds a volume of \sim 15 μ L was assembled using a microscope slide, etched coverslips, and double-sided sticky tape. Before assembly, etched coverslips were incubated in a solution of 100 μ L poly-l-lysine (PLL, Sigma P8920) in 30 mL ethanol for 15 minutes. The coverslip was then dried with a filtered air line. After flow cell assembly, microtubules were diluted 150 times from the stock in a solution of PemTax (1 μ L 10

mM Taxol in 500 μ L PEM80). The diluted microtubules were added to the flow cell via capillary action and allowed to incubate to the PLL surface for 10 minutes. Unbound microtubules were then washed out with 20 μ L PemTax. A solution of casein (Blotting-Grade Blocker, Biorad 1706404) diluted in PemTax (1:8 mixture) was then added to the flow cell and allowed to incubate for 10 minutes to block the remainder of the surface to prevent non-specific binding. We found that the assay was very sensitive to the grade of casein used to block the surface and found optimal results with the blotting-grade blocker used here. After the incubation, the flow cell was washed with 50 μ L PemTax and 80 μ L assay buffer (AB). 20 μ L of the bead solution described above (either tethered or with full motor) that had incubated for 1 hour was then added to the flow cell.

Optical trapping measurements were obtained using a custom built instrument with separate trapping and detection systems. The instrument setup and calibration procedures have been described previously [32]. Briefly, beads were trapped with a 1,064 nm laser that was coupled to an inverted microscope with a 100x/1.3 NA oil-immersion objective. Bead displacements from the trap center were recorded at 3 kHz and further antialias filtered at 1.5 kHz. Position calibration and trap stiffness measurements were obtained using custom Matlab (Mathworks) programs.

To ensure that we were at the single molecule limit for both the binding assay and motility assay, the protein-bead ratio was adjusted so that fewer than half of the beads trapped and tested on microtubules showed binding, actually having 5-10% binding the majority of the time.

In the binding assay, beads were trapped in solution and brought close to surface-bound microtubules to allow for binding of Coil-1. Once a tether was confirmed through visual inspection in DIC mode, the tether was centered by an automated two axis piezostage centering routine. Afterward, the bead was again trapped and the piezostage was translated to load the interaction with force. Rupture of the Coil-1-microtubule interaction was confirmed by the bead diffusing away from the microtubule after the trap is turned off once

the measurement was complete. A single tether was characterized to have a single break back to baseline in the measurements. This was also the case for the directional pulling assay with polarity-marked microtubules. The exception is that the orientation of the microtubule was checked in fluorescence mode, noted, and then after switching back to DIC mode, the piezostage was translated in the direction of testing (either toward the plus end (dimly fluorescent elongation) or minus end (brightly fluorescent seed) of the microtubule).

In the motor motility assay, a motor-coated bead was trapped in solution and subjected to position calibration and trap stiffness Labview routines. Afterward, the bead was brought close to a surface-bound microtubule to allow for binding. Bead position displacement and force generation were measured for single motor-bound beads.

This is very similar to the unloaded velocity assay except for when the bead is brought close to the microtubule, the trap and detection lasers are turned off, and the bead motion on the microtubule is video-tracked with a DAGE CCD camera. Custom Matlab code based on a cross-correlation method was used to track the bead positions over time [44].

2.5.7 Microtubule Bundle Assays

Microtubule bundles were generated by adhering a rhodamine-labeled polarity-marked microtubule to a coverslip surface (substrate microtubule) that was further blocked with casein. A motility mixture consisting of a known concentration of motor, polarity-marked microtubules with a biotinylated seed at the minus end (cargo microtubule), and streptavidin coated beads was then added to the flow cell to allow for spontaneous bundle formation through the motors. A free, streptavidin-coated bead was trapped in solution and brought to an apparent microtubule bundle. Bundles appear slightly thicker than normal isolated microtubules under DIC microscopy. Bead binding to an end verifies that a motor-formed bundle was found as beads only bind the biotinylated minus ends of the cargo microtubules. Control experiments in the absence of motor did not bind microtubules.

2.5.8 Single Molecule Photobleaching Assay

Single molecules of FL-Kif15-GFP were imaged at 200 pM in assay buffer through non-specific adsorption to an etched coverslip in a flow cell. The protein was allowed to incubate for 10 minutes, and then unbound motor was washed out with 3 volumes of assay buffer. Images were acquired at 8.66 Hz using TIRF microscopy equipped with an EMCCD camera. GFP was excited with 488 nm at an exposure time of 0.1 sec. Locating individual fluorescent FL-Kif15-GFP molecules for photobleaching analysis was performed from analysis of video frames using custom software written in Matlab (Mathworks) [45].

2.5.9 Data Analysis

Nanometer position and piconewton force values were measured using calibration data and trap stiffness measurements from each bead before data acquisition. Those traces were visualized in custom-built Matlab code to determine overall signature of the traces as well as the stall force measurements. Other scripts were used to determine lifetimes, velocities, and local force-velocity relationships. Step-finding code based on a sliding Student's t-test was used to determine the boundaries of each step to denote a dwell time in between, as well as allow for measuring varied step sizes [46]. A dwell was defined as constant position over time in between steps. In this code, a dwell was measured if the change in the moving average of position was less than 3 nm. This step threshold was chosen due to the defined step sizes of most kinesins (around 8 nm), but could allow for variability without detecting steps from noise (measurements less than 3 nm). Accounting for steps less than 3 nm shows a marked increase in number of steps. However, upon visual inspection of how the trace was analyzed by the code for accuracy, it was found that these steps below 3 nm were indeed noise and therefore not accounted for in averaging.

Force change correlates with the distance the bead has been displaced from the trap center from motor movement. In order to see how velocity correlates with different forces,

traces were analyzed over 5 second windows to find the average force, or bead position relative to the trap center. The average velocity that correlates with each window was then calculated using a linear fit. These data sets were then used to construct a force-velocity curve.

2.5.10 Stochastic Simulation

In our computational model, a motor protein contains three elements: motor head, stalk, and non-motor tail. Motor head is a stochastic stepper following the three-state force-velocity relation (Equations 1 and 2). Parameters for the three-state model were taken from experimental data for Kif15 (Table 1). At each time step, forward stepping occurs with probability

$$v(F)dt \quad (2.3)$$

where $v(F)$ is the force-dependent speed of the motor, and dt is the time increment per integration step. Under resisting load, a backward step occurs with rate

$$k_b e^{(f\delta_b)} \quad (2.4)$$

where $k_b = 0.25/s$ is the unloaded backward stepping rate, f is the magnitude of the resisting load, and $\delta_b = 4$ nm is the force sensitivity of the backward steps. Values of k_b and δ_b were chosen so that backstepping occurs about 30% of stepping events, as measured experimentally. Unbinding of a motor head occurs with rate

$$\frac{1}{2}k_m^{off} [1 + \text{erf}(f - f_{stall}/2\sigma_s)]. \quad (2.5)$$

Here, $k_m^{off} = 1/s$ is the basal off rate, $\text{erf}(x)$ is the error function, f is the magnitude of the resisting load, $f_{stall} = 2.7$ pN is the stall force, and $\sigma_s = 0.01$ pN is the transition width of

the error function. An unbound motor head immediately relaxes to its equilibrium position and rebinds to the microtubule with rate $5/s$.

For the tail domain, an unbinding event follows a form similar to unbinding of the motor head:

$$\frac{1}{2}k_t^{off} [1 + \text{erf}(f - f_t/2\sigma_t)] \quad (2.6)$$

with $k_t^{off} = 10/s$, $f_t = 6.1$ pN (rupture force of Coil-1), and $\sigma_t = 0.5$ pN. An unbound tail domain immediately relaxes to its equilibrium position and rebinds to the microtubule. The stalk is modeled as a Hookean spring of stiffness 0.5 pN/nm, and force on the motor increases linearly with the distance between its motor head and tail. Choice of model parameters whose values are not experimentally available were made to approximately reproduce the experimental observations in other aspects, such as the motor head stalling and tail rupturing. For the purpose of examining dependence on different model components, in particular, backstepping and tethering (Figure 5D-G), precise values of model parameters are not important.

A microtubule was considered to be rigidly linked to a trapped bead of stiffness 0.04 pN/nm, the same as in the experiment. Time evolution of its position was made via Brownian dynamics method, with a stochastic velocity Verlet integration algorithm. Each run started with five motors. Their motor heads are initially bound to the microtubule and tails are bound to the substrate. After the simulation starts, motors walk along the microtubule and slide it. The microtubule's position and force were recorded in time. In simulations with tethers (Figure 5F,G), five additional motors were introduced, with their tail domains bound to the cargo microtubule, while their motor domains were affixed to the substrate. For these tethers, rupturing of the tails from the cargo microtubule can happen, but their motor domains are immobile, which mimic the situation that can occur during microtubule gliding (Figure 5A), or in an anti-parallel microtubule bundle where motor heads are in rigor states. A more extensive analysis of this model will be published elsewhere.

2.6 Acknowledgements

We would like to thank Wonmuk Hwang for his expertise, critical reading of the paper, and simulation work, all of which greatly strengthened this manuscript. This material is based upon work supported by the National Science Foundation Graduate Research Fellowship Program under Grant No. 1445197 (D.N.R.). This work was also supported, in part, by the Singapore-MIT Alliance for Research and Technology-BioSyM and NSF Grant No. 1330792 (M.J.L.). R.O. was supported by National Institutes of Health R01 GM086610 and is a scholar of the Leukemia and Lymphoma Society.

2.7 Bibliography

- [1] Rebecca Heald and Alexey Khodjakov. Thirty years of search and capture: The complex simplicity of mitotic spindle assembly. *J Cell Biol*, 211(6):1103–11, Dec 2015.
- [2] Lukas C Kapitein, Erwin J G Peterman, Benjamin H Kwok, Jeffrey H Kim, Tarun M Kapoor, and Christoph F Schmidt. The bipolar mitotic kinesin eg5 moves on both microtubules that it crosslinks. *Nature*, 435(7038):114–8, May 2005.
- [3] A Blangy, H A Lane, P d’Hérin, M Harper, M Kress, and E A Nigg. Phosphorylation by p34cdc2 regulates spindle association of human eg5, a kinesin-related motor essential for bipolar spindle formation in vivo. *Cell*, 83(7):1159–69, Dec 1995.
- [4] A P Enos and N R Morris. Mutation of a gene that encodes a kinesin-like protein blocks nuclear division in *a. nidulans*. *Cell*, 60(6):1019–27, Mar 1990.
- [5] I Hagan and M Yanagida. Kinesin-related cut7 protein associates with mitotic and meiotic spindles in fission yeast. *Nature*, 356(6364):74–6, Mar 1992.
- [6] M M Heck, A Pereira, P Pesavento, Y Yannoni, A C Spradling, and L S Goldstein. The kinesin-like protein klp61f is essential for mitosis in *drosophila*. *J Cell Biol*, 123(3):665–79, Nov 1993.
- [7] M A Hoyt, L He, K K Loo, and W S Saunders. Two *saccharomyces cerevisiae* kinesin-related gene products required for mitotic spindle assembly. *J Cell Biol*, 118(1):109–20, Jul 1992.
- [8] T U Mayer, T M Kapoor, S J Haggarty, R W King, S L Schreiber, and T J Mitchison. Small molecule inhibitor of mitotic spindle bipolarity identified in a phenotype-based screen. *Science*, 286(5441):971–4, Oct 1999.
- [9] D M Roof, P B Meluh, and M D Rose. Kinesin-related proteins required for assembly of the mitotic spindle. *J Cell Biol*, 118(1):95–108, Jul 1992.

- [10] K E Sawin, K LeGuellec, M Philippe, and T J Mitchison. Mitotic spindle organization by a plus-end-directed microtubule motor. *Nature*, 359(6395):540–3, Oct 1992.
- [11] Adam M Saunders, James Powers, Susan Strome, and William M Saxton. Kinesin-5 acts as a brake in anaphase spindle elongation. *Curr Biol*, 17(12):R453–4, Jun 2007.
- [12] Christoph Segbert, Rosemarie Barkus, Jim Powers, Susan Strome, William M Saxton, and Olaf Bossinger. Klp-18, a klp2 kinesin, is required for assembly of acentrosomal meiotic spindles in *Caenorhabditis elegans*. *Mol Biol Cell*, 14(11):4458–69, Nov 2003.
- [13] Marvin E Tanenbaum, Libor Macůrek, Aniek Janssen, Erica F Geers, Mónica Alvarez-Fernández, and René H Medema. Kif15 cooperates with eg5 to promote bipolar spindle assembly. *Curr Biol*, 19(20):1703–11, Nov 2009.
- [14] A Sophia Gayek and Ryoma Ohi. Cdk-1 inhibition in g2 stabilizes kinetochore-microtubules in the following mitosis. *PLoS One*, 11(6):e0157491, 2016.
- [15] David Vanneste, Masatoshi Takagi, Naoko Imamoto, and Isabelle Vernos. The role of hklp2 in the stabilization and maintenance of spindle bipolarity. *Curr Biol*, 19(20):1712–7, Nov 2009.
- [16] Emma G Sturgill, Stephen R Norris, Yan Guo, and Ryoma Ohi. Kinesin-5 inhibitor resistance is driven by kinesin-12. *J Cell Biol*, 213(2):213–27, Apr 2016.
- [17] Emma G Sturgill and Ryoma Ohi. Kinesin-12 differentially affects spindle assembly depending on its microtubule substrate. *Curr Biol*, 23(14):1280–90, Jul 2013.
- [18] David J Sharp, Kent L McDonald, Heather M Brown, Heinrich J Matthies, Claire Walczak, Ron D Vale, Timothy J Mitchison, and Jonathan M Scholey. The bipolar kinesin, klp61f, cross-links microtubules within interpolar microtubule bundles of *Drosophila* embryonic mitotic spindles. *The Journal of cell biology*, 144(1):125–138, 1999.

- [19] K L McDonald, E T O'Toole, D N Mastronarde, and J R McIntosh. Kinetochore microtubules in ptk cells. *J Cell Biol*, 118(2):369–83, Jul 1992.
- [20] D N Mastronarde, K L McDonald, R Ding, and J R McIntosh. Interpolar spindle microtubules in ptk cells. *J Cell Biol*, 123(6 Pt 1):1475–89, Dec 1993.
- [21] Geng-Yuan Chen, Keith J Mickolajczyk, and William O Hancock. The kinesin-5 chemomechanical cycle is dominated by a two-heads-bound state. *J Biol Chem*, 291(39):20283–94, Sep 2016.
- [22] Troy C Krzysiak and Susan P Gilbert. Dimeric eg5 maintains processivity through alternating-site catalysis with rate-limiting atp hydrolysis. *J Biol Chem*, 281(51):39444–54, Dec 2006.
- [23] Megan T Valentine, Polly M Fordyce, Troy C Krzysiak, Susan P Gilbert, and Steven M Block. Individual dimers of the mitotic kinesin motor eg5 step processively and support substantial loads in vitro. *Nat Cell Biol*, 8(5):470–6, May 2006.
- [24] Joshua S Weinger, Minhua Qiu, Ge Yang, and Tarun M Kapoor. A nonmotor microtubule binding site in kinesin-5 is required for filament crosslinking and sliding. *Curr Biol*, 21(2):154–60, Jan 2011.
- [25] Yuta Shimamoto, Scott Forth, and Tarun M Kapoor. Measuring pushing and braking forces generated by ensembles of kinesin-5 crosslinking two microtubules. *Dev Cell*, 34(6):669–81, Sep 2015.
- [26] Hauke Drechsler, Toni McHugh, Martin R Singleton, Nicholas J Carter, and Andrew D McAinsh. The kinesin-12 kif15 is a processive track-switching tetramer. *Elife*, 3:e01724, Mar 2014.
- [27] Emma G Sturgill, Dibyendu Kumar Das, Yoshimasa Takizawa, Yongdae Shin, Scott E Collier, Melanie D Ohi, Wonmuk Hwang, Matthew J Lang, and Ryoma Ohi. Kinesin-

- 12 kif15 targets kinetochore fibers through an intrinsic two-step mechanism. *Curr Biol*, 24(19):2307–13, Oct 2014.
- [28] Nathalie Brouwers, Nuria Mallol Martinez, and Isabelle Vernos. Role of kif15 and its novel mitotic partner kbp in k-fiber dynamics and chromosome alignment. *PLoS One*, 12(4):e0174819, 2017.
- [29] K Svoboda and S M Block. Force and velocity measured for single kinesin molecules. *Cell*, 77(5):773–84, Jun 1994.
- [30] K Svoboda, C F Schmidt, B J Schnapp, and S M Block. Direct observation of kinesin stepping by optical trapping interferometry. *Nature*, 365(6448):721–7, Oct 1993.
- [31] M J Schnitzer, K Visscher, and S M Block. Force production by single kinesin motors. *Nat Cell Biol*, 2(10):718–23, Oct 2000.
- [32] Ahmad S Khalil, David C Appleyard, Anna K Labno, Adrien Georges, Martin Karplus, Angela M Belcher, Wonmuk Hwang, and Matthew J Lang. Kinesin’s cover-neck bundle folds forward to generate force. *Proc Natl Acad Sci U S A*, 105(49):19247–52, Dec 2008.
- [33] N J Carter and R A Cross. Mechanics of the kinesin step. *Nature*, 435(7040):308–12, May 2005.
- [34] William R Hesse, Miriam Steiner, Matthew L Wohlever, Roger D Kamm, Wonmuk Hwang, and Matthew J Lang. Modular aspects of kinesin force generation machinery. *Biophys J*, 104(9):1969–78, May 2013.
- [35] Stefan Lakämper and Edgar Meyhöfer. The e-hook of tubulin interacts with kinesin’s head to increase processivity and speed. *Biophys J*, 89(5):3223–34, Nov 2005.
- [36] G I Bell. Models for the specific adhesion of cells to cells. *Science*, 200(4342):618–27, May 1978.

- [37] J Howard and A A Hyman. Preparation of marked microtubules for the assay of the polarity of microtubule-based motors by fluorescence microscopy. *Methods Cell Biol*, 39:105–13, 1993.
- [38] Hauke Drechsler and Andrew D McAinsh. Kinesin-12 motors cooperate to suppress microtubule catastrophes and drive the formation of parallel microtubule bundles. *Proc Natl Acad Sci U S A*, 113(12):E1635–44, Mar 2016.
- [39] Gero Fink, Lukasz Hajdo, Krzysztof J Skowronek, Cordula Reuther, Andrzej A Kasprzak, and Stefan Diez. The mitotic kinesin-14 *ncd* drives directional microtubule-microtubule sliding. *Nat Cell Biol*, 11(6):717–23, Jun 2009.
- [40] Xiaolei Su, Hugo Arellano-Santoyo, Didier Portran, Jeremie Gaillard, Marylin Vantard, Manuel Thery, and David Pellman. Microtubule-sliding activity of a kinesin-8 promotes spindle assembly and spindle-length control. *Nat Cell Biol*, 15(8):948–57, Aug 2013.
- [41] Marcus Braun, Douglas R Drummond, Robert A Cross, and Andrew D McAinsh. The kinesin-14 *k1p2* organizes microtubules into parallel bundles by an atp-dependent sorting mechanism. *Nat Cell Biol*, 11(6):724–30, Jun 2009.
- [42] A Sophia Gayek and Ryoma Ohi. Kinetochore-microtubule stability governs the metaphase requirement for *eg5*. *Mol Biol Cell*, 25(13):2051–60, Jul 2014.
- [43] Janko Kajtez, Anastasia Solomatina, Maja Novak, Bruno Polak, Krno Vukušić, Jonas Rüdiger, Gheorghe Cojoc, Ana Milas, Ivana Šumanovac Šestak, Patrik Risteski, Federica Tavano, Anna H Klemm, Emanuele Roscioli, Julie Welburn, Daniela Cimini, Matko Glunčić, Nenad Pavin, and Iva M Tolić. Overlap microtubules link sister k-fibres and balance the forces on bi-oriented kinetochores. *Nat Commun*, 7:10298, Jan 2016.

- [44] J Gelles, B J Schnapp, and M P Sheetz. Tracking kinesin-driven movements with nanometre-scale precision. *Nature*, 331(6155):450–3, Feb 1988.
- [45] Yongdae Shin, Joseph H Davis, Ricardo R Brau, Andreas Martin, Jon A Kenniston, Tania A Baker, Robert T Sauer, and Matthew J Lang. Single-molecule denaturation and degradation of proteins by the aaa+ clpxp protease. *Proc Natl Acad Sci U S A*, 106(46):19340–5, Nov 2009.
- [46] Sonia K Brady, Sarangapani Sreelatha, Yinnian Feng, Shishir P S Chundawat, and Matthew J Lang. Cellobiohydrolase 1 from *trichoderma reesei* degrades cellulose in single cellobiose steps. *Nat Commun*, 6:10149, Dec 2015.

CHAPTER 3

THE COVER-NECK BUNDLE OF KIF15: A THERAPEUTIC TARGET

3.1 Summary

Kif15 acts as a redundant backup mechanism for bipolar mitotic spindle assembly when Eg5 has been inhibited by a drug. An Eg5 inhibitor in tandem with a Kif15 inhibitor is a promising candidate for chemotherapy, as Sturgill *et al.* have shown that Eg5 inhibited cells cannot survive without Kif15. Therefore, finding a drug that specifically disturbs Kif15 performance is crucial. Cover-neck bundle formation is the force generating mechanism through which kinesins are able to be motile. Here, the coverstrand of Kif15 was targeted as a potential site for specific inhibition. Polyclonal antibodies were generated in rabbits for the portion of the Kif15 coverstrand projected to form a β -sheet with the neck linker. Results show that the antibodies developed inhibit motility of Kif15. However, further studies and challenges are present regarding efficacy of antibody generation from peptide antigens, using sera in assays, and delivery of the final drug.

3.2 Introduction

As described in Chapter 2, Kif15 has been shown to be a promising candidate as a chemotherapy target [1, 2, 3, 4]. As the motor domains of the kinesin family are well conserved, attacking the ATP binding pocket is not ideal as the potential drug might promiscuously inhibit many types of kinesin. Therefore, a sequence specific to Kif15 must be targeted but also be effective at halting function, i.e. force generation.

Cover-neck bundle formation has been proposed to be the force generating mechanism for kinesin [5, 6, 7]. As shown in Figure 3.1, there are two elements that flank the motor domain: the neck linker (NL) and the coverstrand (CS). When no nucleotide is present, the NL and CS are out of phase. Upon binding of ATP, conformational changes occur such that

the NL and CS come close enough in contact to form a β -sheet, also known as the cover-neck bundle (CNB). This β -sheet formation thrusts the trailing head forward, providing the power stroke necessary to advance 8 nm to the next tubulin binding site.

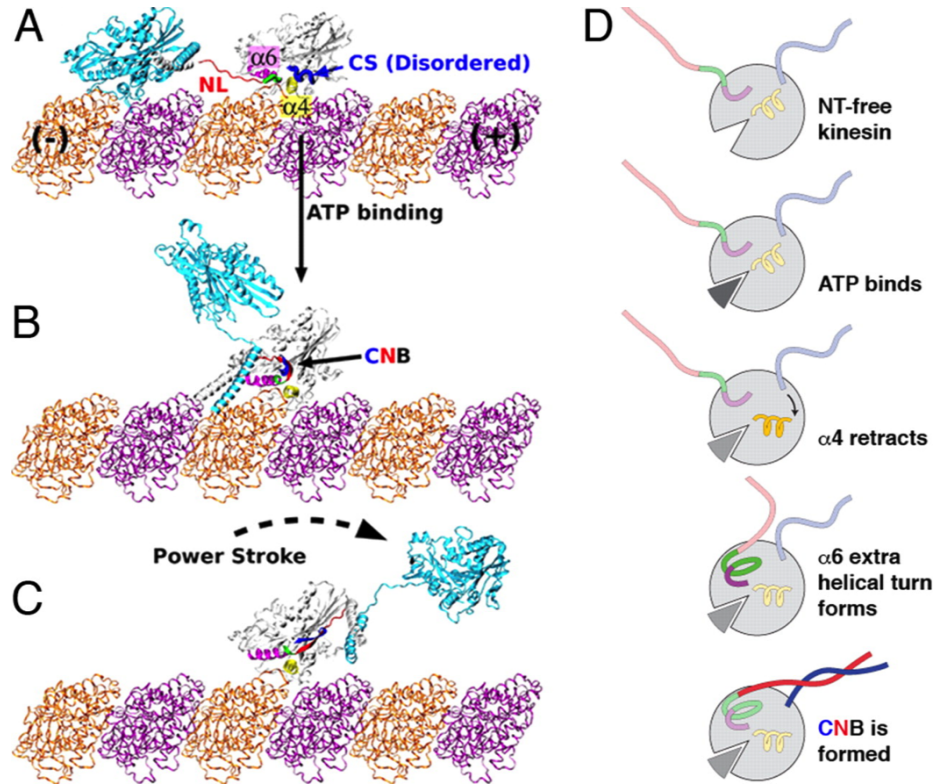


Figure 3.1: **Cover-Neck Bundle Force Generation Mechanism.** (A) The neck linker (NL, red) and coverstrand (CS, blue) are out of phase before ATP binding. (B) Upon ATP binding, $\alpha 4$ retracts, resulting in an extra helical turn of $\alpha 6$. This brings the NL and CS in enough proximity to form a β -sheet. This is known as the cover-neck bundle (CNB). (C) CNB formation generates the power stroke to send the trailing head forward. (D) Schematics of events in A-C. Adapted from Khalil *et al.*, (2008) PNAS. [5] Copyright (2008) National Academy of Sciences, U.S.A.

As shown in Table 3.1, the coverstrand sequences of kinesin-1, kinesin-5, and kinesin-12 are all relatively different as well as are located at different lengths from the N-terminus. There are a few residues, highlighted in yellow, that are either similar or are the same throughout each sequence. This indicates that there are a few key residues necessary for CNB formation, but the CSs are diverse enough to potentially generate different targets. Strikingly, the Loop 13 domains (Table 3.2) and NL domains (Table 3.3) are very similar

in sequence, showing the conserved nature of the residues needed for β -sheet formation. Therefore, the CS of Kif15 was chosen as a potential drug target, namely a polyclonal antibody, to test inhibition ability.

Kinesin-1	R ⁵	E	I	P	A	E	D	S	I ¹³
Kinesin-5	K ¹¹	K	E	E	K	G	K	N	I ¹⁹
Kinesin-12	Q ¹⁹	P	S	N	E	G	D	A	I ²⁷

Table 3.1: **Coverstrand Sequences of Kinesins.** Kinesin-1, Kinesin-5 (Eg5), and Kinesin-12 (Kif15) coverstrand sequences are shown with residue numbers as superscripts. Highlighted cells show residues that are equal or have common functional groups across the different motor proteins.

Kinesin-1	L ²⁹⁸	G	G	N	A ³⁰²
Kinesin-5	L ³²⁴	G	G	R	A ³²⁸
Kinesin-12	L ³²⁸	G	G	N	A ³³²

Table 3.2: **Loop 13 Sequences of Kinesins.** Kinesin-1, Kinesin-5 (Eg5), and Kinesin-12 (Kif15) Loop 13 sequences are shown with residue numbers as superscripts. Highlighted cells show residues that are equal or have common functional groups across the different motor proteins.

Kinesin-1	V ³³³	K	N	V	V	C	V	N	E ³⁴¹
Kinesin-5	I ³⁵⁹	L	N	K	P	E	V	N	Q ³⁶⁷
Kinesin-12	I ³⁶³	K	N	K	A	V	V	N	E ³⁷¹

Table 3.3: **Neck Linker Sequences of Kinesins.** Kinesin-1, Kinesin-5 (Eg5), and Kinesin-12 (Kif15) coverstrand sequences are shown with residue numbers as superscripts. Highlighted cells show residues that are equal or have common functional groups across the different motor proteins.

As antibody development is costly, an initial optical trapping assay was performed with the N420 construct of Kif15 to see if there was any evidence for CNB formation in Kif15 specifically. N420 was chosen because this construct has tags for bead binding on the N-terminus, or the CS. Because of this binding geometry, 16 nm steps should be observed as only one motor head is being monitored by the trap. However, if some intermediate

transitions were occurring, such as CNB formation, those may be observable in a stepping trace. The results of this initial test are shown in Figure 3.2. Strikingly, both 8 and 16 nm steps were observed in multiple traces. As CNB formation occurs when the NL and CS are in close proximity (therefore the motor heads are in close proximity as the step is taking place), then it makes sense that an intermediate transition about halfway between the expected 16 nm steps is observed. In light of these exciting results, antibody generation was pursued (Methods).

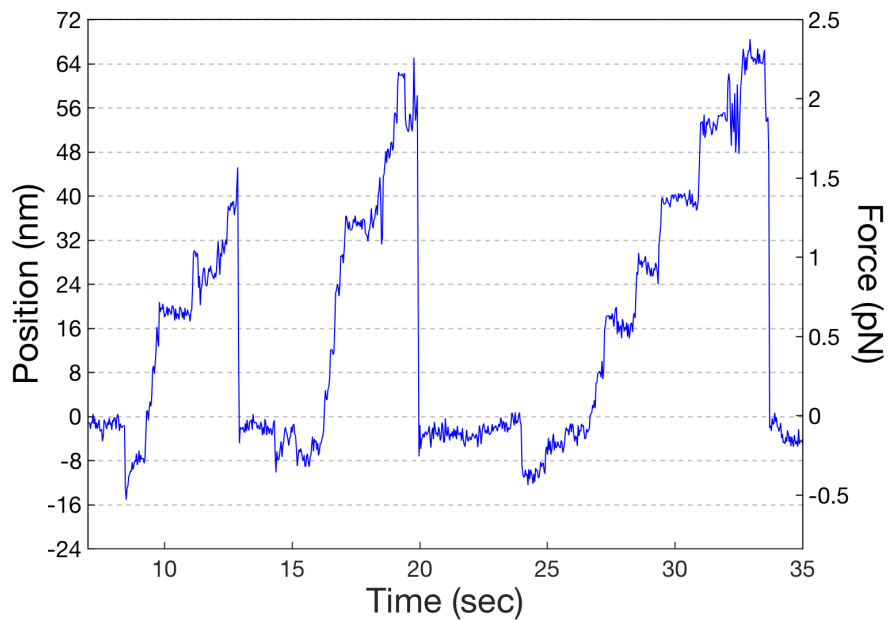


Figure 3.2: **Kif15 Motility with Bead on Motor Head.** The Kif15 construct N420 takes both 8 and 16 nm steps when a bead is attached to one of the motor heads. The 8 nm transitions may be due to cover-neck bundle formation.

3.3 Materials and Methods

3.3.1 Protein Expression and Purification

FL-Kif15, N700, and N420 were expressed and purified as described previously (details in Chapter 2) [1, 3, 2].

3.3.2 Antibody Generation

Polyclonal antibodies for the kinesin-12 Kif15 coverstrand were developed by the Vanderbilt Antibody and Protein Resource at Vanderbilt University. Cocalico Biologicals was outsourced by the antibody core to generate peptides and care for the animals used for antibody production. The peptide QPSNEGDAIC was developed by Cocalico and used to generate antibodies in two rabbits (no. 492 and no. 493).

Cocalico used the following initial protocol for antibody generation. On Day 0, a pre-bleed/initial inoculation was performed. The rabbits were given a booster shot on Days 14 and 21. On Day 35, a test bleed was drawn. On Day 49, another boost was given. On Day 56, another test bleed was drawn. Based on the test bleeds giving low yields of antibody as tested with western blots (Figure 3.3), the rabbits were boosted for another two months every two weeks. As ELISA scores showed significant amounts of antibody present (Figure 3.4), the rabbits were then exsanguinated and terminal sera samples were obtained for both rabbits. Samples were affinity purified by the antibody core.

3.3.3 Screening Assay

Antibody efficacy was tested in an unloaded assay similar to those described previously [1]. Briefly, N700 was diluted 5000x from stock in assay buffer (AB) and incubated with 0.44 μm beads coated in biotinylated anti-His for 1 hour. A flow cell was constructed by adding 100x diluted MTs onto an etched coverslip, allowing them to incubate for 10 minutes. The flow cell was washed with 20 μL PTX and subsequently 20 μL CTX (see appendix for all buffer recipes). CTX incubated for 5 minutes. 50 μL PTX was then washed in flowed by 80 μL assay buffer. For a control experiment, motor coated beads were then added to the flow cell. To test the antibody, an appropriate amount (5 μL or 1 μL) antibody was added to the final motor/bead dilution and incubated for 15 minutes. The final motor/bead solution incubated with antibody was then added to the flow cell.

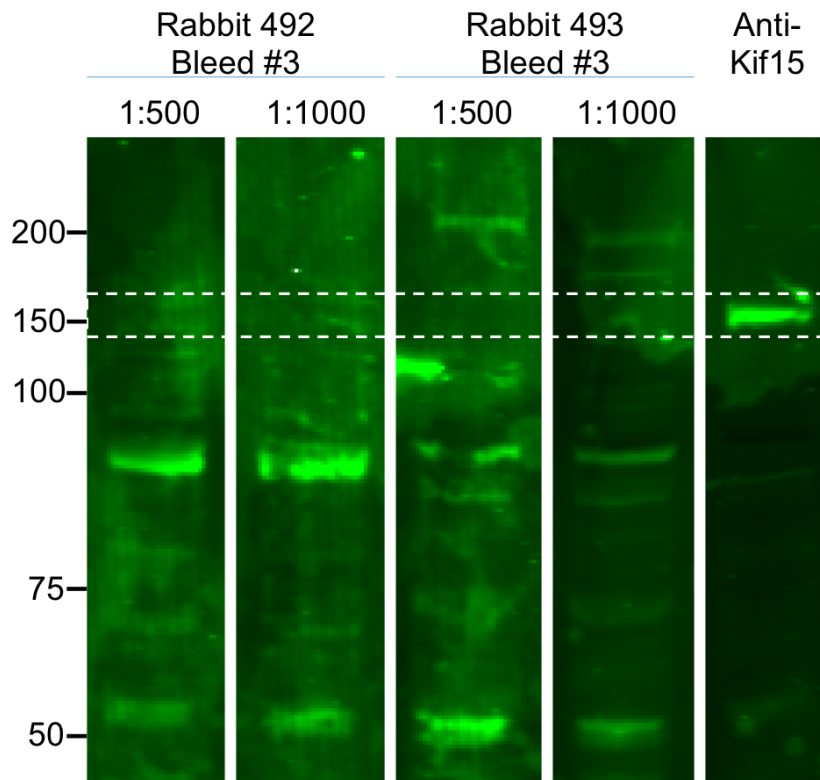


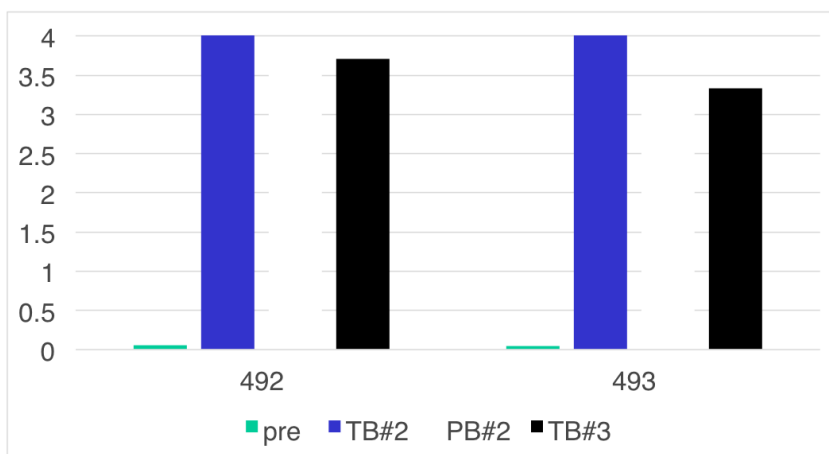
Figure 3.3: **Western Blot of Antibody Pre-Bleeds.** Western blot of pre-bleeds from rabbits 492 and 493 compared against purified anti-Kif15. A faint band is observed for rabbit 493 indicating that there may be some anti-Kif15 activity in the samples.

Upon loading the sealed flow cell onto the microscope, beads in solution were trapped and brought to the surface in close proximity to a MT. The response of the motor coated bead was then recorded to either walk, float away, or bind without walking.

3.4 Results and Discussion

Antibodies for the coverstrand sequence QPSNEGDAIC (Table 3.1 flanked with a cysteine) were generated in two rabbits, 492 and 493, and tested as described in Methods. N700 diluted 5000x was used as a control to test for motility. N700 was chosen because it moved well in previous assays (Chapter 2) and has tags on the C-terminus, leaving the N-terminal CS available for antibody binding. Here, slightly more than 50% of the beads

	KIF15	1:100	1:500	1:1000	1:5000	1:10000	1:20000	1:50000	1:100000	blank	2nd only
pre	492	0.051	0.05	0.061	0.057	0.049	0.058	0.05	0.049	0.049	0.044
	493	0.05	0.05	0.055	0.05	0.064	0.055	0.054	0.061	0.048	0.046
TB#2	492	1.189	4.185	4.305	4.323	4.277	4.246	3.244	1.561	0.056	0.047
	493	1.206	2.722	4.344	4.342	4.283	4.002	2.969	1.476	0.051	0.046
PB#2	492	0.367	1.806	2.835	3.683	3.461	1.883	1.191	0.883	0.045	0.041
	493	0.113	0.644	1.517	3.255	3.7	2.553	2.09	1.763	0.069	0.045
TB#3	492	0.721	1.352	3.117	3.708	2.814	2.17	1.778	0.625	0.048	0.043
	493	0.551	1.337	2.868	3.337	3.232	2.551	1.203	0.936	0.046	0.048



	pre	TB#2	PB#2	TB#3
492	0.057	4.323	3.683	3.708
493	0.05	4.342	3.255	3.337

Figure 3.4: **ELISA Scores of CS Antibodies.** ELISA scores performed by the antibody core showed there to be a significant amount of antibody present in the rabbits just before exsanguination. The y-axis denotes relative abundances of antibody for rabbits 492 and 493. pre refers to pre-bleed of rabbits before being boosted. TB refers to test bleed, and PB refers to production bleed.

tested walked on MTs, indicating that the assays were above the single molecule limit. This was purposeful as this allowed for faithful binding and walking of beads without (1) the beads being so overly saturated with motor that they become immotile or (2) the motor being so dilute that screening becomes difficult to interpret. The control yielded that 43/80 beads were motile, 37/80 beads diffused away, and 0/80 bound without motility.

To test the efficacy of the antibody, 5 μL of production bleed 3 from rabbit 492 were incubated with N700 on beads. After adding this mixture to the flow cell, 0/80 beads were motile, 48/80 diffused away, and 32/80 beads bound without motility. The experiment was repeated except with 1 μL antibody in the incubation to see if using a less concentrated

amount of antibody changed motility results. Here, 0/80 beads were motile, 33/80 beads diffused away, and 47/80 beads bound without motility. These results indicate that the antibody is effective at halting Kif15 motility.

Control experiments with conventional kinesin, or kinesin-1, were performed to ensure the specificity of the antibody to the Kif15 coverstrand. The assay above was repeated except using kinesin-1 diluted 3000x and 1 μ L antibody. Here, 34/40 beads were motile, 2/40 beads diffused away, and 4/40 beads bound without motility. This experiment confirms that the antibody is specifically acting on Kif15.

A different set of control experiments with just sera and anti-His beads showed a large percentage of beads sticking to MTs without motor being present. The antibodies should likely be further purified to get better performance. Nevertheless, the results using kinesin-1 combined with antibody sera still showed motility in the vast majority of beads tested. This suggests that the antibody is still specifically inhibiting Kif15 motility, but challenges are still present in testing in the assay.

Future improvements and work include further purifying the antibody, potentially generating the antibody in a different animal that responds better to peptide antigens, developing monoclonal antibodies, or changing inhibition strategies, such as using an aptamer instead of an antibody. Also, quantitative concentration studies with the antibodies should be performed, as well as testing their inhibition efficacy at the single molecule level. In the end, these studies show that targeting the coverstrand of Kif15, and potentially other kinesins, is a promising avenue for developing specific and effective inhibitors that could later be translated into deliverable drugs.

3.5 Acknowledgements

The Vanderbilt Antibody and Protein Resource developed the antibodies and gave advice throughout the generation process. This material is based upon work supported by the National Science Foundation Graduate Research Fellowship Program under Grant No.

1445197 (D.N.R.). This work was also supported, in part, by the Singapore-MIT Alliance for Research and Technology-BioSyM and NSF Grant No. 1330792 (M.J.L.).

3.6 Bibliography

- [1] Dana N Reinemann, Emma G Sturgill, Dibyendu Kumar Das, Miriam Steiner Degen, Zsuzsanna Vörös, Wonmuk Hwang, Ryoma Ohi, and Matthew J Lang. Collective force regulation in anti-parallel microtubule gliding by dimeric kif15 kinesin motors. *Current Biology*, 27(18):2810–2820, 2017.
- [2] Emma G Sturgill and Ryoma Ohi. Kinesin-12 differentially affects spindle assembly depending on its microtubule substrate. *Current Biology*, 23(14):1280–1290, 2013.
- [3] Emma G Sturgill, Dibyendu Kumar Das, Yoshimasa Takizawa, Yongdae Shin, Scott E Collier, Melanie D Ohi, Wonmuk Hwang, Matthew J Lang, and Ryoma Ohi. Kinesin-12 kif15 targets kinetochore fibers through an intrinsic two-step mechanism. *Current Biology*, 24(19):2307–2313, 2014.
- [4] Emma G Sturgill, Stephen R Norris, Yan Guo, and Ryoma Ohi. Kinesin-5 inhibitor resistance is driven by kinesin-12. *J Cell Biol*, 213(2):213–227, 2016.
- [5] Ahmad S Khalil, David C Appleyard, Anna K Labno, Adrien Georges, Martin Karplus, Angela M Belcher, Wonmuk Hwang, and Matthew J Lang. Kinesin’s cover-neck bundle folds forward to generate force. *Proceedings of the National Academy of Sciences*, 105(49):19247–19252, 2008.
- [6] Wonmuk Hwang, Matthew J Lang, and Martin Karplus. Force generation in kinesin hinges on cover-neck bundle formation. *Structure*, 16(1):62–71, 2008.
- [7] William R Hesse, Miriam Steiner, Matthew L Wohlever, Roger D Kamm, Wonmuk Hwang, and Matthew J Lang. Modular aspects of kinesin force generation machinery. *Biophysical journal*, 104(9):1969–1978, 2013.

CHAPTER 4

PROGRESSIVE KINESIN-14 HSET EXHIBITS DIRECTIONAL FLEXIBILITY DEPENDING ON MOTOR TRAFFIC

4.1 Summary

A common mitotic defect observed in cancer cells that possess supernumerary (>2) centrosomes is multipolar spindle formation. Such structures are resolved into a bipolar geometry by minus end directed motor proteins, such as cytoplasmic dynein and the kinesin-14 HSET. HSET is thought to antagonize plus end directed kinesin-5 Eg5 to balance spindle forces. However, the biomechanics of this force opposition are unclear, as HSET has previously been defined as a non-processive motor. Here, we use optical trapping to elucidate the mechanism force generation by HSET. We show that a single HSET motor has a processive nature with the ability to complete multiple steps while trapped along a MT and when unloaded can move in both directions for microns. Compared to other kinesins, such as the spindle-relevant Eg5, HSET has a relatively weak stall force of 1.1 pN. Moreover, HSET's tail domain and its interaction with the E-hook of tubulin are necessary for long-range motility. *In vitro* polarity-marked bundle assays revealed that HSET selectively generates force in anti-parallel bundles on the order of its stall force. When combined with varied ratios of Eg5, HSET adopts the directionality of these partner motors while acting as an antagonizing force and velocity brake, requiring at least a 10 fold higher Eg5 concentration to surpass HSET's sliding force and velocity. These results reveal HSET's ability to change roles within the spindle from acting as an adjustable MT slider and force regulator to a processive motor that aids in minus end focusing.

4.2 Introduction

Proper assembly of the mitotic spindle is essential for genetically identical daughter cells to be formed. The characteristic bipolar geometry of the spindle arises from the organization of the microtubule (MT) minus ends into two poles, which are generally defined by two centrosomes. The plus ends extend into the midzone, creating MT overlaps and opportunities for attachment to kinetochores [1]. Molecular motors are key to spindle assembly and act through intrinsic force-generating mechanisms. Kinesin-5, or Eg5, slides anti-parallel MTs apart through its homotetrameric structure and plus end directed movement to separate the centrosomes [2]. Kinesin-14 (Ncd for *Drosophila melanogaster* or HSET/KIFC1 for humans), a minus end directed motor, has its motor domain at the C-terminus (as opposed to other plus end directed kinesins) and has a non-motor MT binding domain at the N-terminus [3]. This motor has been shown to have important roles during meiosis and mitosis [4, 5, 6, 7, 8]. In meiotic cells that lack centrosomes, kinesin-14 focuses MT minus ends to form spindle poles [7]. In cancer cells, kinesin-14 focuses supernumerary centrosomes to resolve multipolar structures into a bipolar geometry [9]. The importance of this activity is underscored by a study which demonstrated that HSET is essential for proper spindle assembly in acentrosomal and centrosomal human cancer cells, regardless of normal or supernumerary centrosome number [9].

The mechanism by which kinesin-14 generates force in the spindle is not well understood. In addition, it is not clear if its activities in opposing Eg5 or in clustering supernumerary centrosomes are distinct or related in mechanism. Pole focusing would require unidirectional, processive motion over long distances. However, at the single molecule level, kinesin-14s have largely been thought to be non-processive [10, 11, 12, 13, 14, 15]. Previous kinetic studies by determined that Ncd and Eg5 have low to no chemical processivity, suggesting that the origin is related to structural differences in the coiled coil neck regions from conventional kinesin [16]. However, Eg5 was later shown to be processive by Valentine *et al.* from single molecule (SM) optical trapping assays [17]. It was indeed

demonstrated that artificially coupling two Ncd motors resulted in processive movement for more than 1 μm [14]. Working strokes of single Ncd motors have also been measured in a three-bead optical trapping assay that was originally adapted for non-processive myosin [11, 18]. In an unusual case, yeast kinesin-14 Kar3 has been shown to walk processively as a heterodimer containing a non-motor protein that acts as an anchor while other motor head translocates [19, 20].

HSET has also been established to oppose the activity of Eg5, which individually generates forces up to around 5 pN, and aid in balancing forces within the spindle [7, 17]. Therefore, since kinesin-14 was defined as non-processive, it was assumed that it worked together to oppose Eg5 [6, 8]. However, in spite of its apparent non-processivity, kinesin-14 is still able to collectively slide anti-parallel MTs apart *in vitro* [6, 8, 21] and is even able to regulate the velocity of sliding MTs through sensing motor density in corresponding MT overlap lengths [21]. Feedback regulation in anti-parallel MT bundles has also been observed with kinesin-12 Kif15, which has a similar structure to HSET [22]. Also strikingly, HSET overexpression causes spindle elongation in HeLa cells, which is counterintuitive since kinesin-14s are thought to be minus end directed [4]. Together, due to the distinctly different motor characteristics required for pole focusing and anti-parallel MT sliding, it is likely that HSET has unique underlying motility mechanisms to accomplish these tasks.

Here, we use optical tweezers to investigate the homodimeric kinesin-14 HSET at the SM level to better understand how the motor is able to differentiate between its physiological roles of sliding versus focusing MTs. Three constructs were evaluated: FL-HSET (full length), HSET- ΔT (motor and stalk only), and HSET- ΔM (tail and stalk only) to determine the role each domain plays during motility. We observed that while FL-HSET contains a diffusive element, traces from a weak optical trap show that the motor can in fact take multiple, consecutive steps along a MT. Furthermore, a single unloaded HSET motor can traverse a MT bidirectionally for microns. These results demonstrate that homodimeric FL-HSET is a weakly processive motor. To investigate the sliding role of HSET and its ability

to antagonize outward force generation in the spindle from Eg5, these two motors were investigated in various ratios within the vicinity of polarity-marked bundles. We found that HSET selectively slides anti-parallel MTs apart with a force double that of the stall force. Moreover, at similar concentrations, HSET adopts Eg5's directionality while stunting force and velocity output and requires at least 10x more Eg5 in the surrounding environment to generate force that exceeds HSET alone. Collectively, these results reveal that human kinesin-14 is more processive and directionally flexible than previously appreciated and provide insight into its systems level relationship with Eg5.

4.3 Results

4.3.1 FL-HSET Generates Weak Force at the SM Level

FL-HSET was investigated at the SM level using high-resolution optical tweezers to determine the force generation and processive capabilities of the motor in a loaded environment (Figure 4.1A). Force-displacement measurements were recorded for single molecules of FL-HSET. The SM limit was achieved by diluting the motor such that fewer than 20% of the beads would bind [23].

FL-HSET was able to generate force against a very weak trap with structured stepping and a defined stall, or maximum force, at an average of 1.1 pN (Figure 4.1B). HSET does not have a traditional plateaued stall, as with kinesin-1, but instead falls off abruptly after reaching a maximum force. Furuta *et al.* studied single Ncd motors with an optical trap, and only small, unstructured displacements were observed above baseline; no stepping or stalls were observed [14]. Step sizes and dwell times were obtained through a step/dwell-finding algorithm described in Methods. Step sizes were measured for forward and backward steps and fit to double Gaussian curves (Figure 4.1C). FL-HSET takes 8 nm steps, corresponding to the lattice spacing of tubulin dimers in MTs, with a smaller population of 16 nm steps. These could be due to the diffusive element of the motor taking over briefly or two very

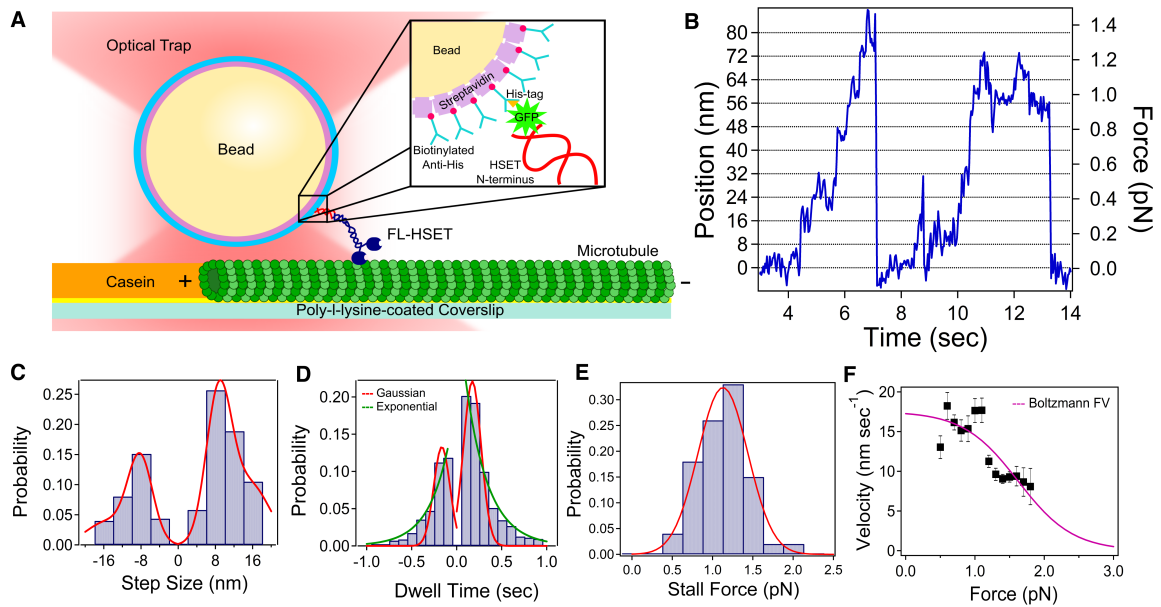


Figure 4.1: FL-HSET is Weakly Processive in Loaded Assay. (A) Schematic of the loaded motility assay. (B) Representative trace of a single FL-HSET motor walking along a MT, taking consecutive steps, reaching a stall force, and then returning to the trap center. (C) The forward (minus end directed) step size of FL-HSET distribution fit to a double Gaussian is $8.7 \text{ nm} \pm 2.7 \text{ nm}$ and $15.6 \text{ nm} \pm 4.2 \text{ nm}$ (average \pm S.D., $N=918$). The backward (plus end directed) step size, also fit to a double Gaussian is $8.2 \text{ nm} \pm 2.7 \text{ nm}$ and $15.4 \text{ nm} \pm 4.4 \text{ nm}$ ($N=465$). (D) FL-HSET dwells between each forward step for $0.17 \text{ sec} \pm 0.1 \text{ sec}$ and each backward step for $0.17 \text{ sec} \pm 0.09 \text{ sec}$. Exponential fits yield a forward time constant of $k^{-1} = 0.25 \text{ sec}$ and backward time constant of $k^{-1} = 0.23 \text{ sec}$. (E) The average stall force of FL-HSET is $1.1 \text{ pN} \pm 0.34 \text{ pN}$ ($N=100$). (F) Force-velocity data (error bars are SEM) were fit to the Boltzmann kinetic model. The parameters for this fit are shown in Table 4.1.

fast 8 nm steps in succession that could not be resolved by our step/dwell-finding algorithm. FL-HSET can also take backward (plus end directed) steps approximately 33% of the time. Dwell time distributions for forward and backward steps are shown in Figure 4.1D and are fit to a single Gaussian and exponential curves. The forward time constant and backward time constant are very similar, $k^{-1} = 0.25 \text{ sec}$ and $k^{-1} = 0.23 \text{ sec}$, respectively. The average stall force of FL-HSET (Figure 4.1E) was found to be very weak (1.1 pN) in comparison to other kinesins (approximately 5 pN for kinesin-1 and kinesin-5) [17, 23].

The force-velocity relationship exhibited by FL-HSET was analyzed, shown in Figure 4.1F, and these data are fit to a one-parameter force-velocity fit (Equation 4.1) [24].

$$V(F) = \frac{V_0(1+A)}{1 + Ae^{F\delta/(k_B T)}} \quad (4.1)$$

Here, V_0 is unloaded velocity, A is a constant that indicates whether the process is biochemically ($A \ll 1$) or mechanically ($A \geq 1$) limited, δ is a characteristic distance, and $k_B T$ is thermal energy. $F_{1/2}$ is the force at which the velocity is half the maximum velocity, or the stall force, and it can be approximated as Equation 4.2.

$$F_{1/2} = \frac{k_B T}{\delta} \ln(A^{-1}). \quad (4.2)$$

The measured and fitted parameters for FL-HSET are shown in Table 4.1. Here, the fitted unloaded velocity is significantly different from the measured value. As demonstrated in Figure 2, FL-HSET at the SM level has a diffusive nature. However, load has a different effect on HSET, and the fitted unloaded velocity is consistent with the measured force velocity data. The fitting also reveals that HSET is biochemically limited, which is consistent with previous kinetic analysis of Ncd that suggested ADP release was the rate-limiting step [12]. The characteristic distance of 10.4 nm is close to the measured step size of HSET as well as the 9 nm working strokes measured in the diffusive three-bead optical trap assay [11]. The predicted stall force and measured stall force values are also very similar. Overall, the Boltzmann relation successfully models experimental HSET force-velocity data.

Experiment			Boltzmann Fit			
Unloaded Velocity (nm s ⁻¹)	Run Length (nm)	Stall Force (pN)	V ₀ (nm s ⁻¹)	A	δ (nm)	F _{1/2} (pN)
245 ± 130	755 ± 610	1.1 ± 0.3	17.3	0.0016	10.4	1.6

Table 4.1: **Boltzmann Model Parameters for Kinesin-14.** Parameters found from fitting Eq. 4.1 to force-velocity data obtained from SM optical trapping experiments. The fit is shown in Figure 4.1F.

4.3.2 Unloaded FL-HSET is Bidirectional

The behavior of FL-HSET without the confines of the trap was evaluated to see if the diffusive nature observed previously with fluorescence was present. The unloaded nature of FL-HSET at the SM level attached to a bead was evaluated using a video-tracking algorithm described in Methods. The assay setup was the same as for the loaded assay except that the trap is turned off once the motor-coated bead binds to the MT. Characteristics such as directionality, velocity, and run length were then evaluated with parameters extracted from the algorithm. Interestingly, FL-HSET still contains a diffusive element at the SM level, even though stepping was observed in the loaded assay. The movement of the motor is bidirectional, in that it moves both towards the minus and plus ends of the MT. A representative trace showing HSET's bidirectionality is shown in Figure 4.2A. Strikingly, microns long distances are observed in these traces in both directions over a time span of minutes. Figure 4.2B shows how dwell finding analysis was used to determine how far HSET moved before changing directions (Methods). Mean squared displacement (MSD) analysis was performed to determine whether the motion observed was directed or diffusive (Figure 4.2C). In averaging the points over the first 20 seconds of each trace, the MSD was linear, with a calculated diffusion constant of $5.9 \times 10^4 \text{ nm}^2/\text{sec}$. This value is very similar to the diffusion constant calculated for FL-HSET in a fluorescence motility assay. However, the data differs in that the unloaded traces measured here are significantly longer than in Norris *et al.* This could be due to photobleaching in the fluorescence experiment, but it is likely that HSET's attachment to a large bead significantly reduces its off-rate.

Figure 4.2D shows the calculated distance traveled in each direction before switching directions to see if FL-HSET had a bias for either. These values were calculated using the step/dwell-finding algorithm described in Methods. Here, a step threshold of 200 nm was used to account for geometric motion of the 440 nm bead. If there were sequential steps in the same direction, they were added together until the step changed directions, where the process was repeated until the end of the trace. This analysis yielded the data in Figure

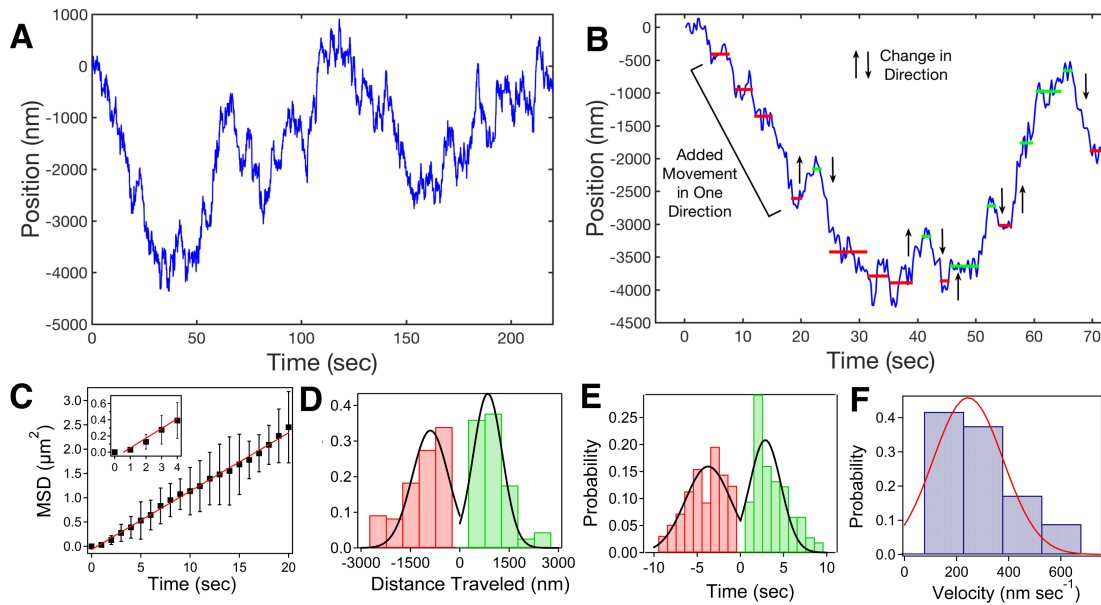


Figure 4.2: HSET is Bidirectional in Unloaded Assay. (A) Representative trace of a single FL-HSET moving along a MT. The trace shows bidirectional movement and association with the MT for minutes at a time. (B) The step/dwell finding algorithm (Methods) demonstrated with the first 70 sec of the trace in (A). Red dwells indicate movement toward one end, and green dwells towards the other. Successive movements in one direction were added together to determine how far HSET moved before changing directions. (C) MSD analysis reveals a diffusion constant $D = 5.9 \times 10^4 \text{ nm}^2/\text{sec}$. Inset shows initial deviation from linearity. (D) Distributions showing the distance traveled in each direction before changing directions. FL-HSET moves $755 \text{ nm} \pm 610 \text{ nm}$ (average \pm S.D.) toward one direction ($N=113$) and $731 \text{ nm} \pm 450 \text{ nm}$ toward the other ($N=117$) before changing directions, showing no preference for movement in either direction. (E) Distributions showing the time traveled in each direction. FL-HSET moves $3.7 \text{ sec} \pm 2.6 \text{ sec}$ toward one end and $2.9 \text{ sec} \pm 1.8 \text{ sec}$ toward the other before changing directions. (F) The unloaded velocity is $245 \text{ nm/sec} \pm 130 \text{ nm/sec}$ (average \pm S.D., $N=192$).

4.2D that are fit to single Gaussian curves. From this, FL-HSET has no directional bias as a single molecule on a single MT. This is reflective of the trace in Figure 4.2A. The time spent traveling in either direction was evaluated the same way (Figure 4.2E), revealing that FL-HSET also spends about the same time traveling in either direction. The average unloaded velocity for this construct (Figure 4.2F) is 217 nm/sec . There is a substantial difference between this velocity and the maximum velocity from the force-velocity data ($\sim 20 \text{ nm/sec}$), suggesting that HSET behaves quite differently when under load than when

able to freely diffuse.

The unloaded assay was repeated on subtilisin-digested MTs (dMT), where the E-hook, or negatively-charged C-terminal tail, is cleaved from MTs [22]. The motor has a significant number of positive residues, especially in the tail domain, that could interact with these E-hooks, promoting processivity. Flow cells with MT and dMT were investigated side-by-side with the same motor-bead dilutions. Under SM conditions with unaltered MTs, 11% of beads (N=65 beads attempted total) showed binding and subsequent bidirectional movement as described above and in Figure 4.2. Interestingly, when repeating the assay with dMTs, no beads bound the surface-attached dMTs (N=60 beads). These results reveal that the E-hook, likely through electrostatic interactions between the motor and MTs, are necessary for initial binding and subsequent motility. E-hook/tail interactions were also observed in fluorescence assays of Ncd [25].

4.3.3 HSET Tail Domain is Required for Substantial Processivity

In addition to studying the properties of FL-HSET, a tailless construct (HSET- Δ T) was made to evaluate the role of the N-terminal tail domain in MT targeting, force generation, and processivity capabilities. The tail domain has been shown to be critical for MT-MT crosslinking, sliding, and focusing spindle poles [6, 8]. We carried out a similar set of unloaded optical trap experiments using HSET- Δ T. This assay proved more difficult than with FL-HSET due to only approximately 40% of the beads showing any movement after binding.

A representative unloaded trace of HSET- Δ T is shown in Figure 4.3A. Consistent with previous results, the bidirectional nature of HSET is not present with HSET- Δ T. MSD analysis revealed that this construct does not act diffusively (Figure 4.3B). However, the MSD shows an initial flat trajectory followed by an upward parabolic trend toward the end. This is reflective of the fact that HSET- Δ T only moved 40% of the time (flat when stationary), but when it did move, it was unidirectional (Figure 4.3A) and directed (upward

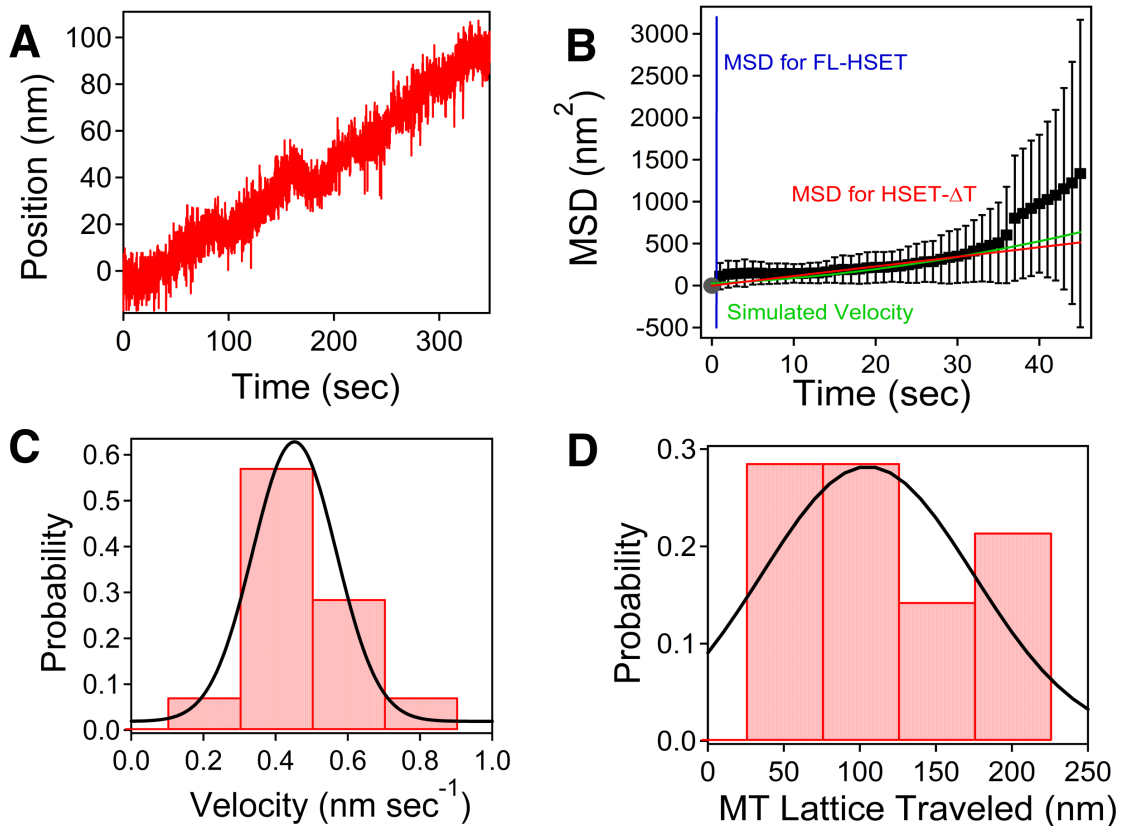


Figure 4.3: HSET Tail Domain Required for Processivity. (A) Representative trace of a single HSET-ΔT motor moving unidirectionally along a MT. (B) MSD analysis revealed an upward parabolic trend toward the end of the trace, indicating directed motion. However, the initial points are flat, which is reflective of HSET-ΔT only moving 40% of the time. The MSD for FL-HSET is shown in blue for comparison, as well as simulated velocity based on experimental unloaded data in green. (C) The average unloaded velocity of HSET-ΔT was fit to a single Gaussian, $0.45 \text{ nm/sec} \pm 0.12 \text{ nm/sec}$ (S.D., $N=14$). (D) The distance traveled along the MT for this construct was $77 \text{ nm} \pm 40 \text{ nm}$ ($N=14$).

parabolic feature). The overall velocity is also much slower (Figure 4.3C), with an average of 0.45 nm/sec . The maximum distance traveled was much smaller than for FL-HSET as well, with an average apparent run length of less than 100 nm (Figure 4.3D). These results show that the tail domain plays a crucial role by facilitating longer run distances, larger velocities, and bidirectionality. In conjunction with the dMT studies performed with FL-HSET, these results suggest that the tail domain is necessary for consistent binding to MTs, and the E-hook likely plays an important role in keeping HSET associated with the MT

lattice.

We next sought to directly investigate the interaction between the tail domain and MTs. We used a purified HSET tail domain construct with the motor domain deleted (HSET- Δ M) in rupture assays to observe the bond lifetime of HSET- Δ M at a defined force, as has been described previously (Figure 4.4A, Methods) [22]. A double Gaussian distribution of lifetimes was revealed through this assay on normal MTs, with average lifetimes of $0.29 \text{ sec} \pm 0.07 \text{ sec}$ and $1.0 \text{ sec} \pm 0.6 \text{ sec}$ (Figure 4.4B). The average force at rupture was $2.1 \text{ pN} \pm 1.2 \text{ pN}$ and $5.6 \text{ pN} \pm 2.3 \text{ pN}$ (Figure 4.4C). The lifetime is also on the order of the dwell time measured between each step in Figure 4.1D. However, the tail domain is then able to quickly rebind, allowing for multiple measurements on the same MT, which is reflective of the ability of unloaded HSET to stay associated with the same MT for a long period of time even though it is moving bidirectionally.

Binding experiments were repeated on dMTs to further investigate the nature of the tail/MT interaction. MT digestion was confirmed through SDS-PAGE where the alpha and beta tubulin bands separated [26]. The lifetime measurements collapsed to a single distribution, with an average of $0.22 \text{ sec} \pm 0.08 \text{ sec}$ (Figure 4.4E). The average force at rupture decreased, with an average of $1.5 \text{ pN} \pm 0.3 \text{ pN}$ and $3.5 \text{ pN} \pm 1.8 \text{ pN}$. However, the vast majority of events occur at the much lower force of 1.5 pN . The lifetime-force relationship was fit to the Bell model, which describes force dependent binding for biological interactions [27]. The distance to the transition state was calculated from each fit with values of 0.52 nm for HSET- Δ M on MT and 0.92 nm on dMT [27, 28]. Together, these results reveal that the tail domain is interacting with MTs through two mechanisms. The tail domain interacts slightly more strongly with the negatively-charged E-hook tail of tubulin. However, the shorter lifetime distribution remains in the digested experiment, which is likely due to the tail interacting weakly with the MT lattice. It is interesting that the lattice interaction lifetime is very similar to the average dwell time between each step, which would mechanically not allow for much processivity alone. However, the additional interaction with the

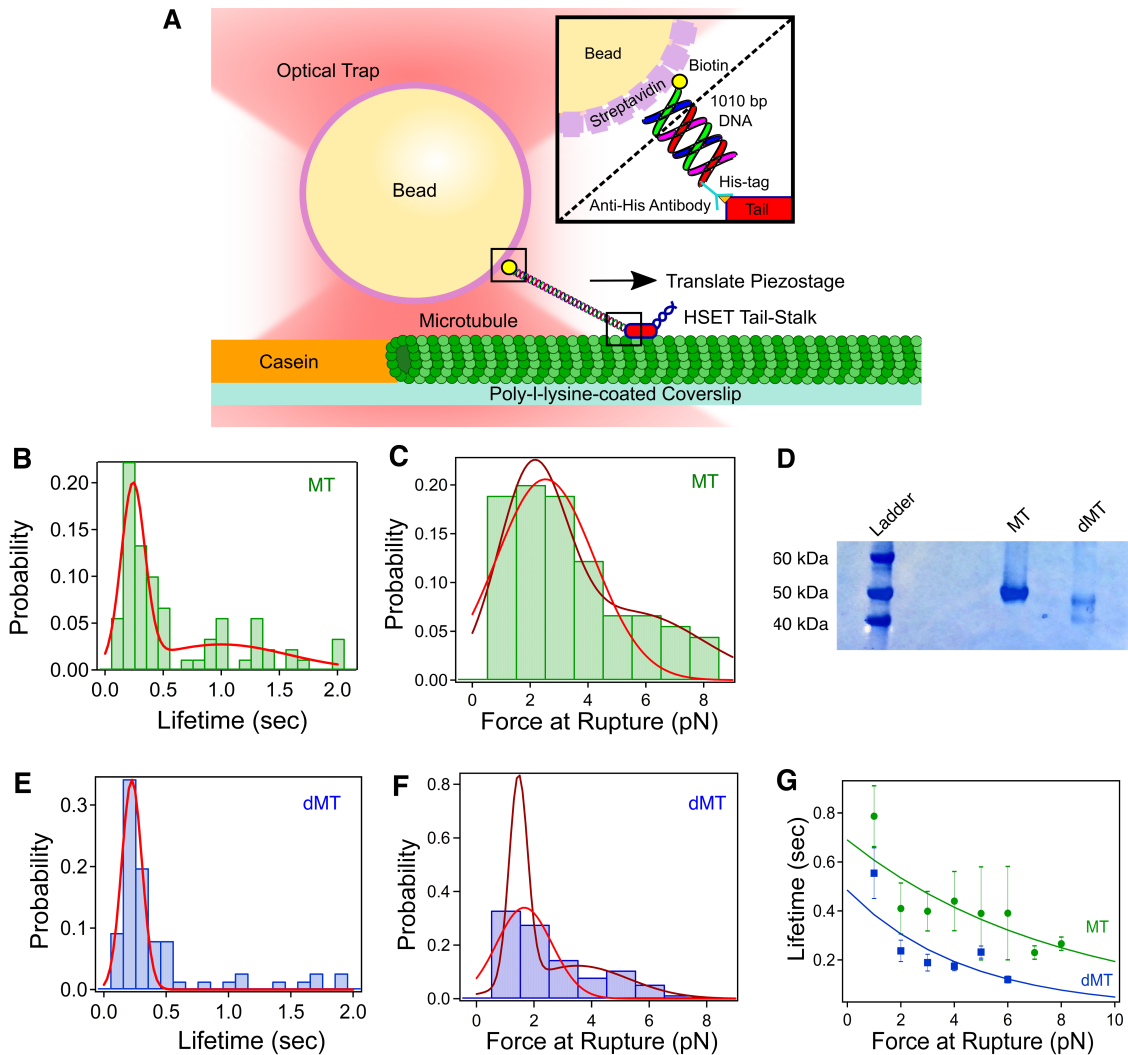


Figure 4.4: HSET Tail Domain Interacts with E-hooks. (A) Assay schematic. (B) Lifetime distribution for TS on normal MTs. There was a double Gaussian distribution, with averages of $0.29 \text{ sec} \pm 0.07 \text{ sec}$ (average S.D.) and $1.0 \text{ sec} \pm 0.6 \text{ sec}$ ($N=90$). (C) The force at rupture for TS on normal MTs was $2.1 \text{ pN} \pm 1.2 \text{ pN}$ and $5.6 \text{ pN} \pm 2.3 \text{ pN}$. (D) SDS-PAGE gel confirming successful E-hook digestion. (E) The double Gaussian lifetime distribution collapsed down to a single for digested MTs, $0.22 \text{ sec} \pm 0.08 \text{ sec}$ ($N=76$). (F) The force at rupture for digested MTs was $1.5 \text{ pN} \pm 0.3 \text{ pN}$ and $3.5 \text{ pN} \pm 1.8 \text{ pN}$, with the majority of events occurring at the lower force. (G) Force-lifetime relationship follows the Bell model showing distinct binding modes on the two MT types. The extracted distances to the transition state is 0.52 nm on MT and 0.92 nm on dMT.

E-hook allows for HSET to stay associated with the MT longer, allowing for the increased potential for processivity, as seen in the unloaded assay (Figure 4.2). Requirement of the E-hook for processivity is in agreement with fluorescence studies of Ncd by Furuta *et al.*

[25].

4.3.4 HSET Acts as a Force Brake Against Eg5

While the interplay of Eg5 and HSET has been investigated previously *in vivo* [4, 7], regulation of their relative force generation in MT bundles has not been explored *in vitro*. Mountain *et al.* reported HSET to oppose the action of Eg5 in bundles [7], and other studies have shown kinesin-14s Ncd and Klp2 to slide anti-parallel MTs apart while locking parallel MTs [6, 8]. However, Cai *et al.* found spindles to elongate upon overexpression of HSET, which suggests that Eg5's outward sliding force is enhanced upon HSET overexpression [4]. To elucidate the role HSET plays with Eg5 in the spindle, an *in vitro* MT bundle assay with known MT orientation was utilized at different Eg5:HSET ratios (Figure 4.5A). First, the force generating capabilities of HSET alone in bundles was investigated using ~ 20 nM HSET (Figure 4.5B). As shown in fluorescence assays, parallel MT bundles become locked (red), with an antagonizing signature around baseline. In anti-parallel bundles (blue), HSET generates a slow force ramp that plateaus off at an average force of $2.2 \text{ pN} \pm 0.8 \text{ pN}$ (avg \pm std, N=18). The average velocity of the force ramp was $0.69 \text{ nm/sec} \pm 0.3 \text{ nm/sec}$ (N=18).

Subsequently, different ratios of Eg5 were added to the HSET bundle assay to evaluate the effect of HSET on Eg5 force generation in bundles (Figure 4.5C). Shimamoto *et al.* found Eg5 force generation to increase linearly with the number of motors in an anti-parallel overlap and also observed a ramp/plateau trace pattern [29]. As the average plateau force for Eg5 (red) was $6.8 \text{ pN} \pm 2.1 \text{ pN}$ (N=7), we can estimate that there are approximately 6-10 motors in the anti-parallel overlap when bundles formed in the presence of ~ 20 nM Eg5 (see Figure 4.2F of [29]). The average ramp velocity was also significantly higher for Eg5 at $1.6 \text{ nm/sec} \pm 0.7 \text{ nm/sec}$. The following Eg5:HSET molar ratios were then employed: 10:1 (orange), 2:1 (yellow), 1:1 (green), and 1:2 (blue). HSET or Eg5 alone is in purple or red, respectively. Interestingly, even though Eg5 at the SM level is

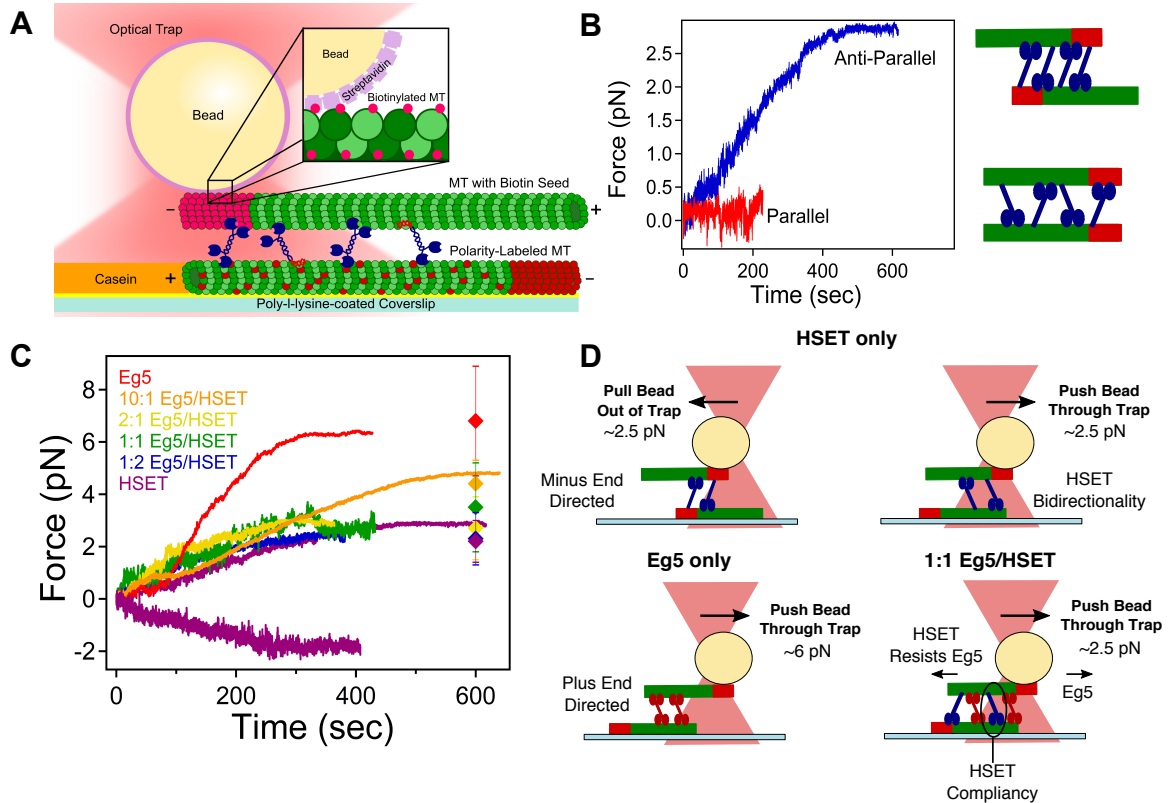


Figure 4.5: HSET Acts as a Force Brake Against Eg5 in Bundles. (A) Bundle assay schematic. (B) HSET selectively generates force in anti-parallel bundles (blue) while parallel bundles (red) become locked. (C) Representative traces of different motor molar ratios of Eg5 and HSET were utilized to determine how HSET affects Eg5 force generation in bundles. Diamonds are average force plateau values. See results in Table 4.2. (D) Direction of cargo MT movement in each bundle scenario. HSET is compliant to Eg5's direction of movement while still resisting Eg5's full force generation potential.

much stronger (stall force ~ 5 pN) than HSET (stall force ~ 1 pN), HSET appears to control the bundle force and velocity characteristics (see Table 4.2). Average plateau forces remain around that of HSET alone in the combined motor assays. The average ramp velocity for HSET alone, 1:2, 1:1, 2:1, and 10:1 Eg5/HSET are all very similar as well. While the velocities were similar between all of the bundles involving HSET, the plateau force increased from an average between 2-3 pN to almost 5 pN for 10:1 Eg5/HSET.

To evaluate whether HSET's bidirectional nature at the SM level has an effect when in combination with the relatively stronger Eg5 motor in bundles, the direction of bundle MT movement was evaluated (Figure 4.5D). Bundle orientation was noted by the polarity

Motor Combination	Ramp Velocity (nm/sec)	Absolute Plateau Force (pN)
Eg5	1.6 ± 0.7 , N=7	6.8 ± 2.1 , N=7
10:1 Eg5/HSET	0.76 ± 0.4 , N=9	4.4 ± 0.9 , N=9
2:1 Eg5/HSET	0.83 ± 0.2 , N=8	2.7 ± 1.2 , N=8
1:1 Eg5/HSET	0.66 ± 0.2 , N=11	3.5 ± 1.7 , N=11
1:2 Eg5/HSET	0.69 ± 0.5 , N=7	2.3 ± 1.0 , N=7
HSET	0.69 ± 0.3 , N=18	2.2 ± 0.8 , N=18

Table 4.2: **Force Generation Parameters in Eg5/HSET Bundles.** Ramp velocity was found by analyzing the displacement of the linear region of a bundle trace. The plateau force was determined by finding the maximum force reached in each bundle trace (avg. \pm std.).

markings (Methods), and the relative direction of cargo MT/bead movement was recorded. In anti-parallel bundles with HSET alone, the bead was both persistently pushed and pulled out of the trap, indicating that HSET motors move collectively in both directions in bundles. HSET diffusion within MT overlaps has also been observed previously in fluorescence experiments [21]. In anti-parallel bundles with Eg5 alone, the bead was solely pushed through the trap. As the bead is on the minus end of the cargo MT and Eg5 is plus end directed, the cargo MT can only be pushed through the trap, and this has been observed previously as well [29]. Interestingly, in all cases where both HSET and Eg5 are in anti-parallel bundles, the bead is solely pushed through the trap, suggesting that Eg5 motility is dominating within bundle overlaps. HSET's directional flexibility thus allows it to be compliant in bundles when a stronger motor is present. However, Eg5 does not overtake HSET in generating force. As shown in Table 4.2, HSET's presence significantly decreases force generation in combined motor bundles. This is likely due to HSET's ability to be minus end directed, as well as its tail domain building resistance within the overlap. Together, these data show that HSET acts as a force brake against Eg5, regulates ramping velocity within bundles, but is also compliant, allowing for sensitive and complex force regulation in anti-parallel overlaps.

4.4 Discussion

By measuring step size, dwell time, and stall force, we have demonstrated that HSET is capable of completing multiple catalytic cycles before releasing from the MT lattice. Until now, kinesin-14s of the Ncd class were thought to be non-processive under physiological conditions through MT gliding [10] and kinetic [12, 16] assays. Although Ncd is capable of hydrolyzing multiple ATP molecules per encounter with the MT lattice, Crevel *et al.* categorized Ncd as being non-processive [16]. In SM fluorescence assays, Ncd was found to be weakly processive, with run lengths ranging from 40-500 nm, but only under very low ionic strength conditions [25]. Until now, a conventional optical trapping assay has not been performed with HSET. Here, we observe FL-HSET take multiple 8 nm steps, reach a stall force, return to the trap center, and reinitiate the cycle over again. The stall force of 1.1 pN is very weak in comparison to other kinesins, such as Eg5 (approximately 5 pN) [17, 29]. Previous studies showed that approximately 4 Ncd motors were required for MT gliding to occur [10], suggesting that it must work in teams in order to slide MTs. However, a weak stall force and the need to work together do not preclude single molecule processivity. Furthermore, the microns-long distances a single HSET traverses in an unloaded assay suggests that even though bidirectional diffusion occurs, the motor also has the ability to undergo processive, unidirectional motion, also evidenced by the multiple consecutive steps observed in the trapping assay. This compliance in directionality could be attributed to the need to constantly regulate Eg5's outward force during mitosis and serve as a force regulator and adjustable crosslinker.

Kinetic parameters were also extracted from the motor's force-velocity relationship using a Boltzmann force-velocity fit. We found that HSET is biochemically limited, agreeing with previous kinetic studies that concluded ADP release was the rate-limiting step for Ncd [12]. Also, the difference between the maximum velocity calculated from the force-velocity curve (~ 20 nm/sec) and the measured unloaded velocity (~ 200 nm/sec) suggests that HSET can sense if load is present and change its motility properties to be compliant in

its surrounding environment.

Studies of HSET- Δ T revealed that the tail domain is required for much extended dwell times and thus long-range motion, as well as the diffusive element of FL-HSET. In HSET, the tail domain may be acting as a temporary anchor, likely due to electrostatic interactions with the E-hook, or negatively charged C-terminal tail, of the MTs, as exhibited in other mitotic kinesins with a non-motor MT binding domain [22]. The presence of the tail domain yielded unbiased bidirectional motion of HSET in the unloaded assay. This could be due to the bead facilitating contact of the tail domain with the E-hooks. Binding experiments confirmed that the tail domain interacts somewhat more strongly with the E-hook present on MTs. Upon digestion of the E-hooks, the motor could not bind the MT, and the tail domain associated very weakly to dMTs in the binding assay. In combination with the unloaded assay, these results show that the tail domain is not sufficient to aid in binding HSET to dMTs. The absence of the tail domain rendered the motor immobile, revealing its importance for overall motility, whether processive or diffusive in nature.

We were also able to evaluate HSET's role in force generation regulation in the presence of Eg5. Not only did we confirm that HSET generates force selectively in anti-parallel MT orientations, but it also acts as a force brake against Eg5. Previous studies have shown that HSET opposes the activity of Eg5 *in vivo* [7], agreeing with our *in vitro* bundle assay result. Braun *et al.* also revealed that HSET localizes in MT overlaps and thus regulates velocity in MT bundles [21]. Our studies reveal that it takes a significant proportion of Eg5 relative to HSET in solution (at least 10:1) to overtake HSET force regulation. Furthermore, Eg5 controls MT sliding direction within bundles while HSET regulates force and velocity. This is reflective of previous findings that Ncd motility is facilitated through guided diffusion [30], which appears to be controllable through neighboring motors. Here, Eg5 dominates the guided direction, but HSET, as an adjustable crosslinker, determines the rate of motion and force magnitude.

How do we reconcile spindle elongation upon HSET overexpression with generation

of an inward spindle force? Yeast kinesin-14 has been shown to align MTs so that Eg5 can exert a more efficient sliding force in the spindle [31]. *In vitro* studies of multiple Ncd motors artificially linked together showed that by even adding one additional motor, processivity and force generation capacity increased, and it increased non-linearly with the addition of up to four motors [14]. Also, Norris *et al.* found that HSET forms motor clusters with soluble tubulin to activate processivity. It is possible that HSET is able to change its role when necessary by acting as a slider until aggregation occurs for a task requiring much higher processivity, such as focusing MT minus ends for spindle bipolarity.

Another possibility could be due to HSET's complex nature in bundles of both being compliant with and resistive against Eg5. Since HSET has the ability to move concertedly with Eg5 due to its combined bidirectional and processive nature, this could explain spindle elongation as opposed to shortening upon overexpression. Other kinesins are also known to toggle between diffusive and motile states, such as Eg5, where motility is activated upon motor head interactions with two anti-parallel tracks [2, 32]. Perhaps HSET is also activated in overlaps.

We have demonstrated here that HSET can be bidirectional and processive. As a single molecule, the motor indeed has the ability to take steps, but the overall behavior appears diffuse and affected by its environment, with the reason for it changing directions after moving microns being unclear. However, the behavior that is responsible for opposing Eg5's outward sliding within bundles could be attributed to both processive and compliant modes of motility. In order to generate productive force against Eg5, processive and unidirectional motion must occur in the opposite direction to some degree. Yet, we have shown that HSET regulates velocity and force production in bundles until a threshold is reached where Eg5 action then dominates, giving light to HSET's adaptability. Therefore, it is likely that both of these qualities are important for HSET's unique function as a force regulator within the spindle. Spindle architecture not only creates tension and compressive stresses but it is dynamic, readjusting to cues as the machinery is assembled [33]. Bundling

multiple MTs together creates a geometry to handle higher forces present in the spindle. Given spindle dynamics, there may be a need to not only bundle microtubules but adjust the position and permit sliding between MT elements to new overall lengths.

4.5 Conclusions

The kinesin-14 HSET was demonstrated through SM optical trapping assays to have a weakly processive nature, having the ability to complete multiple mechanochemical cycles before diffusing away from the MT lattice. This was shown through its ability to take multiple 8 nm steps, reaching a stall force, and repeating the cycle again. The tail domain is required for bidirectional movement and for overall motility through interacting with the E-hook. The motor's ability to crosslink and slide MTs as well as its processive nature suggest that HSET is able to discriminate between different cellular environments. This reflects its conditional ability to be physiologically relevant when centrosome number is not two, making it an attractive cancer therapy target.

4.6 Materials and Methods

4.6.1 Molecular Biology and Baculovirus Construction

HSET and HSET- Δ T were prepared using an HSET cDNA corresponding to Gen Bank Accession Number BC121041. HSET and HSET- Δ T plasmids were prepared in the baculovirus vector pFASTBAC-HTa (Life Technologies) for use with the insect cell expression system. HSET- Δ M was cloned into the bacterial expression vector pET15B (Novagen). Amino acid sequences of the tail, stalk, and motor domains of HSET/KIFC1 (*H. sapiens* kinesin-14) were determined by sequence alignment to Ncd (*D. melanogaster* kinesin-14) using [8] as a guide, and used to design pFASTBAC-HTa-EGFP-HSET Δ T. pFASTBAC-HTa-EGFP-HSET Δ T also contains a flexible amino acid linker (GGSGGS) to ensure rotational freedom between domains.

Each construct contains the corresponding amino acid sequence, which was verified by DNA sequencing:

pFASTBAC-HTa-EGFP-HSET: MSYY-His6-YDIPTTENLYFQGAMDPEF-EGFP(aa 1-239)-HSET(aa 1-673).

pFASTBAC-HTa-EGFP-HSET Δ T: MSYY-His6-YDIPTTENLYFQGAMDPEF-EGFP(aa 1-239)-GGSGGS-HSET(aa 139-673).

pFASTBAC-HTa-HSET: MSYY-His6-DYDIPTTENLYFQGAMDPEF-HSET(aa 1-673).

pET15B-HTa-EGFP-HSET Δ M: MGSS-His6-SSGLVPRGSH-EGFP(aa 1-239)-SGLRS-RAQASNS-HSET(aa 1-304).

All constructs were prepared by isothermal assembly [34]. PCR fragments consisting of HSET amino acids 1-673 (pFASTBAC-HTa-EGFP-HSET, pFASTBAC-HTa-HSET), 139-673 (pFASTBAC-HTa-EGFP-HSET Δ T), or 1-304 (pET15B-HTa-EGFP-HSET Δ M) were generated by amplification of the HSET ORF (using pEGFP-C1-HSET as a DNA template [35] using Phusion DNA polymerase (New England Biolabs M0530S). These fragments were then assembled into their expression vectors cut using the indicated restriction enzymes: pFASTBAC-HTa-EGFP-HSET: EcoRI/XhoI. pFASTBAC-HTa-EGFP-HSET Δ T, pFASTBAC-HTa-HSET: EcoRI/KpnI. pET15B-HTa-EGFP-HSET Δ M: NdeI/XhoI Constructs were used with the Bac-to-Bac system (Invitrogen) per manufacturers' protocol to create a baculovirus expressing the indicated protein.

4.6.2 Protein Expression and Purification

Constructs in the pFASTBAC-HTa vector were expressed in Sf9 cells by infecting them with the corresponding baculovirus for 72 hours. Constructs in the pET15B vector were expressed in BL21DE3 cells with 0.4 mM IPTG for 16 hours at 16°C. Each protein was purified via His6-affinity chromatography, followed by size exclusion chromatography, as follows: cells were pelleted and resuspended in PNI buffer (50 mM sodium phosphate, 500 mM NaCl, 20 mM imidazole) with 5 mM β -mercaptoethanol (β -ME), 1% NP40, and pro-

tease inhibitors (1 mM phenylmethylsulfonyl fluoride, 1 mM benzamidine, and 10 $\mu\text{g}/\text{mL}$ each of leupeptin, pepstatin, and chymostatin). Cells were then lysed by sonication and clarified by centrifugation at 4°C at 35K rpm for 1 hour in a Ti-45 rotor (Beckman). 4 mL of Ni⁺⁺-NTA agarose (Qiagen) were incubated with the supernatant for 1-2 hours, then washed extensively with wash buffer (PNI, 5 mM β -ME, 50 μM MgATP) for 3-4 hours. The proteins were then eluted from the Ni⁺⁺-NTA agarose column in PNI with 5 mM β -ME, 180 mM imidazole, and 100 μM MgATP. Peak fractions (5 mL total) were then subjected to size exclusion chromatography on a Hiload 16/60 Superdex 200 preparatory grade column (GE Healthcare) in gel filtration buffer (10 mM K-HEPES, pH 7.7, 1 mM DTT, 300 mM KCl, and 100 μM MgATP). Protein concentrations were determined in mg/mL using Bradford assays (BioRad) and converted to molar units assuming dimer formation. Powdered sucrose was added to 20% w/v, then each protein was aliquoted, snap frozen in liquid nitrogen, and stored at -80°C.

4.6.3 Microtubule Preparation

Tubulin was reconstituted and polymerized into MTs as described previously [22]. Tubulin (bovine, Cytoskeleton TL238) was reconstituted in 25 μL PEM80 buffer (80 mM PIPES (Sigma P-1851), 1 mM EGTA (Sigma E-4378), 4 mM MgCl₂ (Mallinckrodt H590), pH adjusted to 6.9 with KOH) supplemented with 1 mM GTP (Cytoskeleton BST06) and kept on ice. Tubulin from PurSolutions (bovine, 1001) was also used and reconstituted in the supplied polymerization buffer. 13 μL PEM104 buffer (104 mM PIPES, 1.3 mM EGTA, 6.3 mM MgCl₂, pH adjusted to 6.9 with KOH), 2.2 μL 10 mM GTP, and 2.2 μL DMSO were mixed. 4.8 μL of 10 mg/mL tubulin were added to the mixture and allowed to incubate for 40 minutes at 37°C. Subsequently, 2 μL of stabilization solution (STAB, 38.6 μL PEM80, 0.5 μL 100 mM GTP, 4.7 μL 65 g/L NaN₃ (Sigma S-8032), 1.2 μL 10 mM Taxol (Cytoskeleton TXD01), 5 μL DMSO (Cytoskeleton)) was added to the stock microtubule solution at room temperature.

MTs with their E-hooks digested by subtilisin were also prepared as described previously [22]. Digested microtubules were made by removing the C-terminal E-hook of microtubules with subtilisin. 7.5 μL of pre-formed microtubules were mixed with 0.75 μL of 20 μM subtilisin (Sigma P8038) and was allowed to incubate at 37°C for 40 minutes. To stop digestion, 0.8 μL of 20 mM PMSF (phenylmethanesulfonyl fluoride, Sigma P7626) in DMSO was added to the digested microtubule mixture. 2 μL of STAB solution was then added to the digested microtubules at room temperature.

Polarity-marked microtubules were prepared by making a brightly fluorescent microtubule seed and polymerizing dimmer tubulin from that nucleation point. The microtubule seed was formed using GMPCPP, a non-hydrolysable analog of GTP (Jena Bioscience NU-405L). Rhodamine-labeled tubulin (Cytoskeleton, TL590M) was used in different concentrations to denote the bright seed from the dimmer elongation. First, the seed was polymerized by mixing 13 μL PEM104, 2.2 μL 10 mM GMPCPP, 2.2 μL DMSO, 4 μL non-labeled tubulin (10 mg/mL), and 1 μL rhodamine-labeled tubulin (10 mg/mL). The seed mixture was incubated at 37°C and allowed to incubate for 40 minutes. The elongation solution was made by mixing 13 μL PEM104, 2.2 μL 10 mM GTP, 2.2 μL DMSO, 2 μL non-labeled tubulin (10 mg/mL), and 1.5 μL rhodamine-labeled tubulin (1 mg/mL). The elongation mixture was incubated at 37°C for 1 minute to ensure that the mixture was at least at room temperature. After the minute was complete, 1.5 μL of the seed mixture was added to the elongation mixture and allowed to incubate at 37°C for 40 minutes. Subsequently, 2 μL of STAB solution was added to the polarity-marked microtubules at room temperature.

4.6.4 Single Molecule Optical Trapping Assays

0.44 μm streptavidin-coated beads (Spherotech, Lake Forest, IL) were prepared by washing with phosphate-buffered saline (PBS) followed by sonication. These beads were then incubated in 0.2 mg/mL biotinylated anti-His tag antibody (Qiagen, Hilden, Germany)

to create anti-His coated beads. The beads were then washed 4 times with PBS by centrifuging at 10,000 rpm for 6 minutes to remove any unbound antibody. After gentle sonication, FL-HSET and HSET- Δ T constructs diluted in assay buffer (AB, PEM80 (80 mM PIPES (Sigma Aldrich, St. Louis, MO), 1 mM EGTA (Sigma Aldrich, St. Louis, MO), 4 mM MgCl₂ (Mallinckrodt, Dublin, Ireland), pH adjusted to 6.9 with KOH), 1 mM DTT (Sigma Aldrich, St. Louis, MO), 20 μ M Taxol (Cytoskeleton, Denver, CO), 1 mg/mL casein (Blotting-Grade Blocker, Biorad, Hercules, CA), 1 mM ATP (Sigma Aldrich, St. Louis, MO))) were incubated with the biotinylated anti-His beads to allow binding of the N-terminal His-tag for 1 hour at 4°C on a rotator in the presence of oxygen scavenging reagents (5 mg/mL β -D-glucose (Sigma Aldrich, St. Louis, MO), 0.25 mg/mL glucose oxidase (Sigma Aldrich, St. Louis MO), and 0.03 mg/mL catalase (Sigma Aldrich, St. Louis, MO)).

Flow cells with an approximate volume of 15 μ L were constructed by attaching an etched coverslip to a microscope slide with two strips of double-sided tape. Before flow cell construction, the etched slide was incubated with poly-l-lysine (Sigma Aldrich, St. Louis, MO) for subsequent MT attachment. After assembly, MTs were diluted 100-200 times in PemTax (0.02 mM Taxol in PEM80), added to the flow cell, and incubated for 10 minutes. The flow cell was then washed with 2 volumes of PemTax to remove any unbound MTs. Casein diluted in PemTax to 1 mg/mL was then added and incubated for 10 minutes to reduce any non-specific binding. 5 volumes of PemTax were then added to wash out any unbound casein, followed by 8 volumes of AB. 2 volumes of the bead/motor solution described above were then added to the flow cell.

Optical trapping measurements were obtained using a custom built instrument described previously [36, 37, 38]. Bead displacements from the trap center were recorded at 3 kHz and antialias filtered at 1.5 kHz. Position and trap stiffness calibrations were measured using custom Labview (National Instruments) programs. The SM limit of the assay was determined through serial dilution of the motor constructs such that fewer than half of the

beads trapped bound to MTs, with an actual binding percentage of about 10% [23]. In loaded motility assays, beads were trapped in solution where position and trap stiffness calibrations were performed. Subsequently, the bead was brought to a MT adhered to the coverslip surface to allow for binding. Displacement and force generation were then measured for single motor-bound beads. In unloaded motility assays, beads are trapped in solution and brought to a MT. The trapping laser is turned off, and the motion of the bead is then video-tracked with a DAGE CCD camera. Cross-correlation methods were used to track bead positions over time through custom MATLAB code [37, 39, 40]. Mean squared displacement (MSD) analysis of unloaded traces was performed using the Matlab plug-in msdalyzer [41]. MSDs were then averaged over 1-second intervals.

Tail binding measurements were obtained by pulling on beads tethered to MTs through the tail domain. The tail domain was tethered to streptavidin beads by a 1,010 base pair DNA linker functionalized with biotin on one end and a terminal amine on the other. The 1,010 bp DNA linkers were created as described previously [22]. The amine was further crosslinked to anti-His antibody (GenScript, Piscataway, NJ) using sulfo-NHS/EDC chemistry (ThermoScientific), as described previously [22]. The diluted beads in a 100 μ L volume were incubated with 1 μ L of diluted 100x diluted DNA linker (25 ng/ μ L stock) and 1 μ L 100x diluted tail-stalk (10 μ M stock) for 1 hour. Flow cells were created as described above. In the final step, the tethered beads were added. Beads were then trapped in solution and brought close to MTs to allow for tether formation. The piezostage was then moved 200 nm at 2 μ m/sec to impart force on the interaction. Single ruptures were characterized through a single, uninterrupted return to baseline after the force ramp.

Measurement of force generation in polarity-marked MT bundles was performed as described previously [22]. Briefly, fluorescent polarity-marked MTs were added to a poly-l-lysine coverslip in a flow cell and allowed to incubate for 10 minutes. After washing with buffer, casein was used to block the remainder of the surface to prevent non-specific binding, incubating for 5 minutes. While the first two steps incubated, diluted 1.25 μ m

streptavidin coated beads were incubated with concentrated biotin seed MTs (minus end biotinylated seed formed with GMPCPP, non-labeled tubulin polymerized from the seed to form an elongation) in the presence of oxygen scavenging reagents. The bead/MT solution was then diluted 100x, and the appropriate ratio of motor (Eg5:HSET) was added. The bead/MT/motor solution was then quickly added to the flow cell. Force and displacement measurements were recorded within 30 minutes of the final addition. Bundle orientation was determined by knowing the location of the trap center (streptavidin bead will only be by the biotinylated minus end of the top MT) and the relative location of the fluorescent polarity marked MT on the bottom.

Calibration and trap stiffness data were used to determine the displacement and force generation with resolution at the nm and pN levels, respectively. Motility traces, and stall forces therein, were visualized using custom-written MATLAB code as described previously [36, 37, 38]. Other codes were used to determine lifetimes, velocities, run lengths, and force-velocity relationships. A step/dwell-finding algorithm based on a sliding Student's t-test was used to determine the edge of each step so that a dwell was defined in between [42]. A step threshold of 3 nm was imposed due to the defined step sizes of most kinesins being around 8 nm but also allowing for variation without detecting noise. The force-velocity behavior of FL-HSET was calculated by averaging force over 5 second windows, and the average velocity for each window was calculated using a linear fit. The data were then fit to a three-state kinetic model (Eq. 4.1 and Eq. 4.2).

4.6.5 Quantification and Statistical Analysis

All experiments were repeated until convergence and high N to ensure that the data were robust. Average and standard deviation are reported throughout the paper and figure legends. Error bars are standard error unless stated otherwise. The N value for each experiment is reported in each figure. N represents: number of stalls (Figure 4.1E), number of steps (Figure 4.1C, Figure 4.2D), number of dwells (Figure 4.1D, Figure 4.2E), number of

velocity traces (Figure 4.2F, Figure 4.3C), number of processivity measurements (Figure 4.2D, Figure 4.3D), number of lifetime measurements (Figure 4.4B, Figure 4.4E), number of rupture events (Figure 4.4C, Figure 4.4F), number of parallel bundle measurements (Figure 4.5B), number of anti-parallel bundle measurements (Figure 4.5B), and number of mixed bundle traces (Figure 4.5C). In the custom written algorithms used for analysis, a sliding Student's t-test was used to determine boundaries (steps, dwells, stalls, change in direction) in each trace.

4.7 Acknowledgements

We would like to thank the Ohi lab and Stephen Norris for their expertise, critical reading of the manuscript, and for materials used in this study. We are also grateful for helpful discussions with William Hancock and Marija Zanic about this work. This material is based upon work supported by the National Science Foundation Graduate Research Fellowship Program under Grant No. 1445197 (D.N.R.). This work was also supported, in part, by the Singapore-MIT Alliance for Research and Technology-BioSym and NSF Grant No. 1330792 (M.J.L). R.O. was supported by the National Institutes of Health R01 GM086610 and is a scholar of the Leukemia and Lymphoma Society.

4.8 Bibliography

- [1] Rebecca Heald and Alexey Khodjakov. Thirty years of search and capture: The complex simplicity of mitotic spindle assembly. *J Cell Biol*, 211(6):1103–1111, 2015.
- [2] Lukas C Kapitein, Erwin JG Peterman, Benjamin H Kwok, Jeffrey H Kim, Tarun M Kapoor, and Christoph F Schmidt. The bipolar mitotic kinesin eg5 moves on both microtubules that it crosslinks. *Nature*, 435(7038):114–118, 2005.
- [3] Heather B McDonald, Russell J Stewart, and Lawrence SB Goldstein. The kinesin-like ncd protein of drosophila is a minus end-directed microtubule motor. *Cell*, 63(6):1159–1165, 1990.
- [4] Shang Cai, Lesley N Weaver, Stephanie C Ems-McClung, and Claire E Walczak. Kinesin-14 family proteins hset/xctk2 control spindle length by cross-linking and sliding microtubules. *Molecular biology of the cell*, 20(5):1348–1359, 2009.
- [5] Christian Hentrich and Thomas Surrey. Microtubule organization by the antagonistic mitotic motors kinesin-5 and kinesin-14. *The Journal of Cell Biology*, 189(3):465–480, 2010.
- [6] Marcus Braun, Douglas R Drummond, Robert A Cross, and Andrew D McAinsh. The kinesin-14 klp2 organizes microtubules into parallel bundles by an atp-dependent sorting mechanism. *Nature cell biology*, 11(6):724–730, 2009.
- [7] Vicki Mountain, Calvin Simerly, Louisa Howard, Asako Ando, Gerald Schatten, and Duane A Compton. The kinesin-related protein, hset, opposes the activity of eg5 and cross-links microtubules in the mammalian mitotic spindle. *The Journal of cell biology*, 147(2):351–366, 1999.
- [8] Gero Fink, Lukasz Hajdo, Krzysztof J Skowronek, Cordula Reuther, Andrzej A

- Kasprzak, and Stefan Diez. The mitotic kinesin-14 ncd drives directional microtubule–microtubule sliding. *Nature cell biology*, 11(6):717–723, 2009.
- [9] Julia Kleylein-Sohn, Bernadette Pöllinger, Michaela Ohmer, Francesco Hofmann, Erich A Nigg, Brian A Hemmings, and Markus Wartmann. Acentrosomal spindle organization renders cancer cells dependent on the kinesin hset. *J Cell Sci*, 125(22):5391–5402, 2012.
- [10] Michael J DeCastro, Chih-Hu Ho, and Russell J Stewart. Motility of dimeric ncd on a metal-chelating surfactant: evidence that ncd is not processive. *Biochemistry*, 38(16):5076–5081, 1999.
- [11] Regis M Fondecave, Leigh A Clarke, Christoph F Schmidt, Russell J Stewart, et al. Working strokes by single molecules of the kinesin-related microtubule motor ncd. *Nature cell biology*, 2(10):724–729, 2000.
- [12] Kelly A Foster and Susan P Gilbert. Kinetic studies of dimeric ncd: evidence that ncd is not processive. *Biochemistry*, 39(7):1784–1791, 2000.
- [13] Anthony E Butterfield, Russell J Stewart, Christoph F Schmidt, and Mikhail Skliar. Bidirectional power stroke by ncd kinesin. *Biophysical journal*, 99(12):3905–3915, 2010.
- [14] Ken’ya Furuta, Akane Furuta, Yoko Y Toyoshima, Misako Amino, Kazuhiro Oiwa, and Hiroaki Kojima. Measuring collective transport by defined numbers of processive and nonprocessive kinesin motors. *Proceedings of the National Academy of Sciences*, 110(2):501–506, 2013.
- [15] E Pechatnikova and EW Taylor. Kinetics processivity and the direction of motion of ncd. *Biophysical journal*, 77(2):1003–1016, 1999.

- [16] IM-TC Crevel, A Lockhart, and RA Cross. Kinetic evidence for low chemical processivity in *ncd* and *eg5* edited by j. karn. *Journal of molecular biology*, 273(1):160–170, 1997.
- [17] Megan T Valentine, Polly M Fordyce, Troy C Krzysiak, Susan P Gilbert, and Steven M Block. Individual dimers of the mitotic kinesin motor *eg5* step processively and support substantial loads in vitro. *Nature cell biology*, 8(5):470–476, 2006.
- [18] Jeffrey T Finer, Robert M Simmons, and James A Spudich. Single myosin molecule mechanics: piconewton forces and nanometre steps. *Nature*, 368(6467):113–119, 1994.
- [19] Christine Mieck, Maxim I Molodtsov, Katarzyna Drzewicka, Babet van der Vaart, Gabriele Litos, Gerald Schmauss, Alipasha Vaziri, and Stefan Westermann. Non-catalytic motor domains enable processive movement and functional diversification of the kinesin-14 *kar3*. *Elife*, 4:e04489, 2015.
- [20] Maxim I Molodtsov, Christine Mieck, Jeroen Dobbelaere, Alexander Dammermann, Stefan Westermann, and Alipasha Vaziri. A force-induced directional switch of a molecular motor enables parallel microtubule bundle formation. *Cell*, 167(2):539–552, 2016.
- [21] Marcus Braun, Zdenek Lansky, Agata Szuba, Friedrich W Schwarz, Aniruddha Mitra, Mengfei Gao, Annemarie Lüdecke, Pieter Rein ten Wolde, and Stefan Diez. Changes in microtubule overlap length regulate kinesin-14-driven microtubule sliding. *Nature chemical biology*, 13(12):1245, 2017.
- [22] Dana N Reinemann, Emma G Sturgill, Dibyendu Kumar Das, Miriam Steiner Degen, Zsuzsanna Vörös, Wonmuk Hwang, Ryoma Ohi, and Matthew J Lang. Collective force regulation in anti-parallel microtubule gliding by dimeric *kif15* kinesin motors. *Current Biology*, 27(18):2810–2820, 2017.

- [23] Karel Svoboda and Steven M Block. Force and velocity measured for single kinesin molecules. *Cell*, 77(5):773–784, 1994.
- [24] Michelle D Wang, Mark J Schnitzer, Hong Yin, Robert Landick, Jeff Gelles, and Steven M Block. Force and velocity measured for single molecules of rna polymerase. *Science*, 282(5390):902–907, 1998.
- [25] Ken'ya Furuta and Yoko Yano Toyoshima. Minus-end-directed motor ncd exhibits processive movement that is enhanced by microtubule bundling in vitro. *Current Biology*, 18(2):152–157, 2008.
- [26] Stefan Lakämper and Edgar Meyhöfer. The e-hook of tubulin interacts with kinesin's head to increase processivity and speed. *Biophysical journal*, 89(5):3223–3234, 2005.
- [27] George I Bell et al. Models for the specific adhesion of cells to cells. *Science*, 200(4342):618–627, 1978.
- [28] Johannes Stigler and Matthias Rief. Ligand-induced changes of the apparent transition-state position in mechanical protein unfolding. *Biophysical journal*, 109(2):365–372, 2015.
- [29] Yuta Shimamoto, Scott Forth, and Tarun M Kapoor. Measuring pushing and braking forces generated by ensembles of kinesin-5 crosslinking two microtubules. *Developmental cell*, 34(6):669–681, 2015.
- [30] Sirish Kaushik Lakkaraju and Wonmuk Hwang. Hysteresis-based mechanism for the directed motility of the ncd motor. *Biophysical journal*, 101(5):1105–1113, 2011.
- [31] Austin J Hepperla, Patrick T Willey, Courtney E Coombes, Breanna M Schuster, Maryam Gerami-Nejad, Mark McClellan, Soumya Mukherjee, Janet Fox, Mark Winey, David J Odde, et al. Minus-end-directed kinesin-14 motors align antiparallel

- microtubules to control metaphase spindle length. *Developmental cell*, 31(1):61–72, 2014.
- [32] Siet MJL van den Wildenberg, Li Tao, Lukas C Kapitein, Christoph F Schmidt, Jonathan M Scholey, and Erwin JG Peterman. The homotetrameric kinesin-5 klp61f preferentially crosslinks microtubules into antiparallel orientations. *Current Biology*, 18(23):1860–1864, 2008.
- [33] Frederick Gittes, E Meyhöfer, Sung Baek, and Jonathon Howard. Directional loading of the kinesin motor molecule as it buckles a microtubule. *Biophysical journal*, 70(1):418–429, 1996.
- [34] Daniel G Gibson, Lei Young, Ray-Yuan Chuang, J Craig Venter, Clyde A Hutchison, and Hamilton O Smith. Enzymatic assembly of dna molecules up to several hundred kilobases. *Nature methods*, 6(5):343–345, 2009.
- [35] Emma G Sturgill, Dibyendu Kumar Das, Yoshimasa Takizawa, Yongdae Shin, Scott E Collier, Melanie D Ohi, Wonmuk Hwang, Matthew J Lang, and Ryoma Ohi. Kinesin-12 kif15 targets kinetochore fibers through an intrinsic two-step mechanism. *Current Biology*, 24(19):2307–2313, 2014.
- [36] William R Hesse, Miriam Steiner, Matthew L Wohlever, Roger D Kamm, Wonmuk Hwang, and Matthew J Lang. Modular aspects of kinesin force generation machinery. *Biophysical journal*, 104(9):1969–1978, 2013.
- [37] Yongdae Shin, Joseph H Davis, Ricardo R Brau, Andreas Martin, Jon A Kenniston, Tania A Baker, Robert T Sauer, and Matthew J Lang. Single-molecule denaturation and degradation of proteins by the aaa+ clpxp protease. *Proceedings of the National Academy of Sciences*, 106(46):19340–19345, 2009.
- [38] Ahmad S Khalil, David C Appleyard, Anna K Labno, Adrien Georges, Martin Karplus, Angela M Belcher, Wonmuk Hwang, and Matthew J Lang. Kinesin’s cover-

neck bundle folds forward to generate force. *Proceedings of the National Academy of Sciences*, 105(49):19247–19252, 2008.

- [39] Jeff Gelles, Bruce J Schnapp, and Michael P Sheetz. Tracking kinesin-driven movements with nanometre-scale precision. *Nature*, 331(6155):450–453, 1988.
- [40] Yongdae Shin, Yaqing Du, Scott E Collier, Melanie D Ohi, Matthew J Lang, and Ryoma Ohi. Biased brownian motion as a mechanism to facilitate nanometer-scale exploration of the microtubule plus end by a kinesin-8. *Proceedings of the National Academy of Sciences*, 112(29):E3826–E3835, 2015.
- [41] Nadine Tarantino, Jean-Yves Tinevez, Elizabeth Faris Crowell, Bertrand Boisson, Ricardo Henriques, Musa Mhlanga, Fabrice Agou, Alain Israël, and Emmanuel Laplantine. Tnf and il-1 exhibit distinct ubiquitin requirements for inducing nemo–ikk supramolecular structures. *J Cell Biol*, 204(2):231–245, 2014.
- [42] Sonia K Brady, Sarangapani Sreelatha, Yinnian Feng, Shishir PS Chundawat, and Matthew J Lang. Cellobiohydrolase 1 from *trichoderma reesei* degrades cellulose in single cellobiose steps. *Nature communications*, 6:10149, 2015.

CHAPTER 5

BIOCONJUGATED CORE-SHELL MICROPARTICLES FOR HIGH FORCE OPTICAL TRAPPING

*This chapter is adapted from Reinemann *et al.*, “Bioconjugated Core-Shell Microparticles for High Force Optical Trapping” *Particle and Particle Systems Characterization* (2018) by permission granted under the Wiley license policy.

5.1 Summary

Due to their high spatial resolution and precise application of force, optical traps are widely used to study the mechanics of biomolecules and biopolymers at the single-molecule level. Recently, core-shell particles with optical properties that enhance their trapping ability represent promising candidates for high-force experiments. To fully harness their properties, methods for functionalizing these particles with biocompatible handles are required. Here, we provide a straightforward synthesis for producing functional titania core-shell microparticles with proteins and nucleic acids by adding a silane-thiol chemical group to the shell surface. These particles display higher trap stiffness compared to conventional plastic beads featured in optical tweezers experiments. These core-shell microparticles were also utilized in biophysical assays such as amyloid fiber pulling and actin rupturing to demonstrate their high force applications. We anticipate the functionalized core-shells can be used to probe the mechanics of stable proteins structures that are inaccessible using current trapping techniques.

5.2 Introduction

Optical traps have been widely used as a tool to measure small displacements, exert finely controlled forces, and manipulate microscopic objects [1]. By tethering a biomolecule

of interest between a dielectric particle, for example a plastic bead, and a glass coverslip surface, the optical force and position can be finely controlled to measure the mechanical properties of proteins, nucleic acids, biopolymers, and protein aggregates involved in physiological function as well as disease [2, 3, 4, 5]. An optical trap is formed by focusing a laser beam into a diffraction-limited spot using a high numerical aperture objective lens. In the presence of the optical trap, a dielectric particle, through redirecting the light, will experience a gradient force laterally toward the focus of the trap where the photon flux is highest, as well as a scattering force in the direction of propagation of light [1]. A dielectric object, referred to here as a trapping handle, is trappable when the magnitude of the gradient force is larger than that of the scattering force. Using a single gradient optical trap, objects with refractive indices larger than $n=1.73$ become untrappable in an aqueous medium, such as biological buffers, due to large amounts of scattering [6]. Yet, fine tuning the difference in index of refraction of the trapping handle and the surrounding medium can lead to higher trapping force [7].

Micrometer-sized beads, normally made of polystyrene, are widely employed in optical trapping experiments. These beads are commercially available and feature a wide range of surface functionalization with chemically reactive molecules including primary amines, carboxylates, and hydroxyls, which in turn can be conjugated to biomolecules of interest for single molecule experiments [8]. However, most experiments utilizing these polystyrene beads are measuring relatively low forces, such as from molecular motor motility (~ 5 pN) [9], binding affinity of proteins to cytoskeletal filaments (~ 50 pN) [10], and structural transitions of DNA (~ 65 pN) [11]. Conventional optical tweezers have been used to initially probe high force biological phenomena such as amyloid fiber strength [3, 4], DNA packaging [12], and rheology of cytoskeletal networks [13], but high force measurements generally require either larger beads or alternate approaches such as magnetic tweezers [14, 15], microneedle manipulation [15, 16], or atomic force microscopy [15].

Recently, Schaffer and coworkers developed anatase-titania core microspheres with de-

creased scattering and exceptionally high trapping stability [17] without the need to use high laser powers that can lead to photodamage of biomolecules, sample heating, and damage to optics [18]. Titania microparticles with an anatase core and amorphous shell represent a model system for high force optical trapping experiments due to the differences in dielectric constant between the core and shell that allows for a simple assay change (from polystyrene beads to core-shell microparticles) to increase the trap stiffness without altering the instrumental setup. In order to leverage these very promising core-shell titania microparticles for cell and molecular biophysics research, clear and straightforward methods for synthesizing and functionalizing the surface must be developed. Whereas microparticles with an anti-reflection coating have been preliminarily utilized in cellular binding and manipulation experiments, [19, 20] the proteins used for binding were non-covalently attached to the bead surface. Non-covalently tethered biomolecules are not ideal for high force applications due to uncertainties in the protein geometry and strength.

Here, we report a robust synthetic approach to design core-shell titania microparticles that achieve high trapping forces and a strategy for covalently linking proteins (prion proteins, streptavidin) or nucleic acids to these particles. We then demonstrate their use in inherently high force biophysical assays. We anticipate the methods described here will permit wider use of these improved trapping handles in optical trapping applications requiring the use of currently inaccessible high forces [3, 4], as well as in combined coincident optical trapping and fluorescence assays [21, 22] where minimizing laser powers while maintaining trapping stability is vital [23].

5.3 Materials and Methods

5.3.1 Core-Shell Microparticle Synthesis

The synthetic strategy used in this paper is outlined in Figure 5.1, based on Jannasch *et al.* [17]. High refractive index cores are necessary to increase trapping stability of the

final particles. To make the titania cores, a 0.46% (by weight) solution of titanium butoxide (TBT) was chelated with ethylene glycol (EG) overnight in a nitrogen environment under rotation. Specifically, a mixture of 154 μL TBT and 30 mL EG was made in a 60 mL cleaned and dried glass jar inside a nitrogen glove box. The glove box is necessary because the reagents are water sensitive, and the addition of water severely alters the core synthesis. Before the jar was closed, a stir bar was added, and the jar was parafilm multiple times before removing it from the glove box to mix overnight at ambient conditions. It should be noted that if it is necessary to bring micropipettes and tips into the glove box, the tips should not be attached to the micropipette. Any residual trapped air in the tip can lead to misshapen cores or no core formation; therefore, they must be fully purged with nitrogen as with everything else. Also, cutting off the bottom of the pipette tip at approximately the first graduated line to make the opening larger aids greatly in accurately pipetting viscous liquids throughout this protocol (such as TBT and Tween-20).

A 2.03 mM Tween-20 solution in 100 mL of acetone was made and rigorously stirred for 10 minutes. Then, 100 μL of water was added to this solution. The amount of water is crucial for the spherical shape of the cores. Subsequently, the acetone solution was mixed with 18-20 mL of the TBT-EG solution, depending on the size of cores needed (19 mL of TBT-EG solution produced ~ 500 nm cores, Figure 5.2B). Adding more or less TBT-EG will make the cores bigger or smaller, respectively. The reaction mixture was stirred for 10 minutes to allow for the initial formation of precipitate, the magnetic stir bar was removed, and the solution was stored at room temperature for 24 hours. The relatively transparent solution turned into a milky white solution, then forming a precipitate at the bottom of the jar. The particles were collected by centrifuging the solution for five minutes at 7,000 rpm and redispersed in cold ethanol stored at 4°C a total of three times. After the final centrifugation step, the pellet was dried in a microcentrifuge tube in a convection oven at 70°C for thirty minutes to evaporate any remaining solvent prior to calcination. The dried cores were then annealed for 1 hour at 500°C in a furnace (Blue M, M15A-

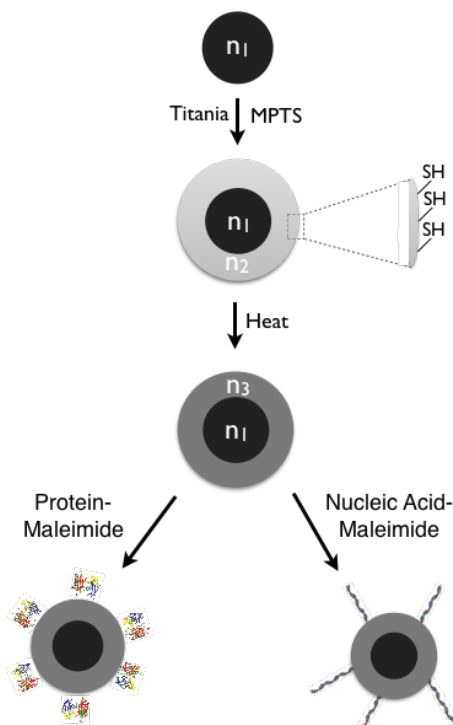


Figure 5.1: **Synthetic strategy for the production of anatase-titania core-shell particles functionalized with proteins or nucleic acid structures.** Anatase cores with a high index of refraction ($n_1 \sim 2.3$) are coated with an amorphous titania shell (with index of refraction $n_2 \sim 1.6$), and functionalized with surface exposed thiol groups using MPTS (see Methods). The index of refraction of the shell can be tuned by heating to an estimated $n_3 \sim 1.7-1.8$, which leads to high trapping stability (see Discussion). The surface exposed thiol groups can be crosslinked to proteins and nucleic acids using thiol chemistry.[24]

1A) to induce a transition of the titania into the anatase phase. Conversion of the cores into the anatase phase was verified using Raman spectroscopy (Renishaw inVia) at 532 nm [25, 26]. The cores were sized using a light microscope with differential interference contrast microscopy (DIC). ImageJ [27] was used to analyze the size of the cores in pixels. A pixel to nm conversion can be formed by sizing a distribution of beads with a known size, for example $0.44 \mu\text{m}$, $0.75 \mu\text{m}$, and $1.25 \mu\text{m}$ beads sold by Spherotech. The annealed cores can be stored at room temperature in a sealed container overnight.

The next step is to add shells, which enable the redirection of light in two stages such that an effectively higher refractive index particle is produced. The shells will also be chemically functionalized for biocompatibility. For the addition of the amorphous titania shells,

0.5 mg of anatase cores were resuspended in 3.3 mL of cold ethanol with 800 μM Lutensol and disaggregated using a probe sonicator. Separately, a solution of 3.3 mL ethanol and 50-175 μL of TBT was prepared in a glove box under a nitrogen environment in a clean glass jar with a lid. It is essential that the ethanol have no contaminants, such as water or other organic solvents. Thus, the glove box should be purged prior to each use to ensure that trace amounts of organic solvents from other users have been removed. Outside of the glove box, the core dispersion solution was quickly added to the TBT solution to lessen contact with humid air. The jar was then parafilm multiple times. The amount of TBT added in this step dictates the diameter of core-shell particles after mixing, with 100 μL TBT producing core-shell particles with diameter $\sim 1,350$ nm. The core-TBT mixture was reacted for a total of two hours in a temperature controlled bath sonicator at $\sim 30^\circ\text{C}$. The water level in the sonicator should be maintained below the lip of the jar to ensure that no water enters the reaction. Ice can be added to the bath every ten minutes if heating occurs from constant sonication, as this can affect the integrity of the parafilm. To incorporate surface exposed thiol groups, 80 μL of a 1:100 dilution of (3-mercaptopropyl)trimethoxysilane (MPTS) in ethanol was added to the reaction mixture after 1 hour of sonication. The MPTS solution was prepared under a nitrogen environment in a glovebox. Upon completion of the two-hour reaction, the core-shell particles were cleaned by centrifuging for 5 minutes at 5,000 rcf, resuspending in 3 mL of cold ethanol after each wash for a total of three times. After the final wash, the particles were sonicated for 2 minutes prior to heating. It is important to sonicate the core-shell particles prior to storage or any use as they will clump over time.

The refractive index of the shell can be altered and optimized by heating. Longer heating times result in higher refractive index and concomitantly smaller particles. To tune the index of refraction of the titania shell, a 100 μL aliquot of the cleaned core-shells was centrifuged for 5 minutes at 1,500 rcf in a microcentrifuge tube, and the supernatant was removed. The pellet was resuspended in 10 μL of cold ethanol and sonicated for 2 minutes. The aliquot was then spun down in a mini-centrifuge for a few seconds, and the supernatant

was removed. The pellet was heated at 50°C on a dry block heater for 5-15 minutes. The particles were then quenched by placing the microcentrifuge tube on ice for 1 min, followed by resuspension of the particles in 100 μ L of phosphate buffered saline buffer (137 mM NaCl, 2.7 mM KCl, 10 mM Na₂HPO₄, 2 mM KH₂PO₄, pH = 7.4), sonicated for 2 minutes, and stored at 4°C under rotation. The final diameter of the core-shells particles was determined similarly to the sizing process described for the anatase cores.

5.3.2 Covalent Crosslinking to Protein or DNA

A two-step crosslinking reaction was used to covalently couple amine-containing proteins to the surface exposed sulfhydryl groups of the particles. The procedure described here is for the Sup35 prion protein³ harboring a terminal amine group opposite a C-terminal biotin tag. However, the methodology is applicable to any biomolecule with a surface exposed primary amine moiety, such as a DNA strand with a terminal amine.

A 30 μ L solution of 100 μ M protein in PBS was incubated with 3 μ L of 20 mM sulfosuccinimidyl 4-[N-maleimidomethyl]cyclohexane-1-carboxylate (sulfo-SMCC), a heterobifunctional crosslinker, at room temperature for two hours. During the incubation period, 25 μ L of core-shell particles were cleaned in 500 μ L of PBS containing 0.1% Tween-20 (PBST) by centrifuging at 1,500 rcf for 2 minutes, resuspended in 100 μ L of PBS, and sonicated for 2 minutes. Excess sulfo-SMCC was removed from the protein or DNA solution using a disposable desalting chromatography column (Micro Bio-Spin, Biorad) in PBS buffer a total of three times. The maleimide-activated protein or DNA was then immediately added to the core-shell suspension and mixed overnight at 4°C. The bio-functionalized core-shells were then washed three times at 1,500 rcf for 2 minutes, and stored in 100 μ L of PBST buffer under rotation at 4°C until use.

5.3.3 Optical Trapping and TIRF

The core-shell particles were tested using a custom built optical trapping instrument [28]. The optical trapping instrument relies on back focal plane detection of scattered photons for position detection. To quantify any improvement in trapping stability when using core-shells versus commercially available polystyrene particles, the trapping and detection lasers were first aligned, and the trap stiffness was calculated using an equipartition based calibration [29]. For each batch of core-shells the variance of at least five beads was measured.

To measure the presence of covalently linked proteins on the bead surface using fluorescence, a custom-built total internal reflection fluorescence (TIRF) microscope with a 532 nm excitation laser (World Star Technologies) was used for excitation of the Sup35 proteins labeled with Alexa555. Fluorescence emission was imaged using an EM-CCD camera (Andor Technologies).

5.3.4 Amyloid Tethering

To test the functionality of core-shell beads in an inherently high force assay, tethers were made with amyloid fibers in the same manner as described previously [3, 4]. NM monomers from Sup35 prions, fluorescently-tagged NM, and biotinylated-NM were prepared as described previously [3]. Strong-psi (mechanically less strong) NM seeds were used in this study. NM coated particles were prepared by conjugating streptavidin to thiol-coated particles through the sulfo-SMCC crosslinking reaction. Maleimide-streptavidin was formed by mixing 100 μL of streptavidin (0.5 mg/mL in PBS) with 2.5 μL sulfo-SMCC ($\sim 23\text{mM}$ in DMSO) and reacted at room temperature for 2 hours under rotation. The streptavidin-SMCC mixture was purified using a desalting column equilibrated with CRBB buffer (5 mM KPO_4 , 150 mM NaCl, pH 7.2 + 5 mM TCEP). To bind maleimide-streptavidin to thiol-coated particles, 30 μL of maleimide-streptavidin was combined with

200 μ L thiol-coated particles. The mixture was incubated for at least 2 hours at room temperature or overnight at 4°C. The particles were then spun down and clarified in CRBB. Then, they were gently sonicated for 2 minutes. To make NM coated particles, 50 μ L streptavidin-coated particles were combined with 1.5 mL biotinylated-NM at 1.2 mM and allowed to incubate for 1 hour at 4°C.

Amyloid fibers were formed as described previously [3]. Briefly, NM fiber solution was made containing 2.5 mM NM monomer, fiber seeds, CRBB, and 5 mM TCEP. 2.5 mL NM fiber seeds, which are mature NM fibers seeded by yeast cell lysates, were added to 497.5 mL CRBB with 5 mM TCEP. NM monomer was added to the solution to make the final concentration of monomer 2.5 mM. The sample was briefly vortexed, wrapped with aluminum foil, and incubated at 4°C for 1 day.

The amyloid pulling assay was assembled similarly as described previously [3, 4]. Assembly takes advantage of the fact that the amyloid fiber monomers can be used as handles that fold onto pre-formed amyloid fibers [3, 4]. A flow cell was constructed by using a non-etched coverslip and adhering it to a microscope slide with double sided sticky tape. NM monomers diluted in CRBB buffer (5 mM KPO_4 , 150 mM NaCl, pH 7.2 + 5 mM TCEP) at 1 mM were added to the flow cell and allowed to incubate for 15 minutes. The flow cell was then washed with 5 volumes of CRBB to wash out any unbound monomer. Casein (Blotting-Grade Blocker) at 5 mg/mL was then added and allowed to incubate for 40 minutes in order to block any non-specific binding of future assay components. The flow cell was washed with 5 volumes of CRBB, and subsequently, pre-formed amyloid fibers were added. After 15 minutes, the flow cell was washed three times with 1 mL of CRBB + 0.1 mg/mL casein. Core shell particles coated in NM monomer were then added to the flow cell and allowed to incubate overnight under high humidity at 4°C. Before trapping experiments took place, the flow cell was washed three times with 200 mL of CRBB + 0.1 mg/mL casein to wash out any unbound particles.

For the amyloid pulling experiment, a surface tethered bead was located on the coverslip

surface and subsequently centered in the detection laser, similarly to the DNA stretching assay. The optical trap was turned on, and the piezostage was translated to generate force by displacing the bead from the trap center. Bead position and force were measured using custom-written LabVIEW algorithms.

5.3.5 Actin Rupture Experiments

Biotinylated actin (10 actin:1 biotinylated actin) was polymerized as described previously [30]. Briefly, 5 μL 10 mg/mL actin (Cytoskeleton, AKL99) were mixed with 5 μL 1 mg/mL biotinylated actin (Cytoskeleton, AB07). General Actin Buffer (GAB, 5 mM Tris-HCl, 0.2 mM CaCl_2 , 0.5 mM DTT, 0.2 mM ATP) was made, and 100 μL were added to the actin mixture. This mixture was placed on ice for 1 hour. Polymerization occurred upon adding 11 μL Actin Polymerization Buffer (APB, 50 mM Tris-HCl, 500 mM KCl, 2 mM MgCl_2 , 2 mM CaCl_2 , 2 mM DTT, 5 mM ATP) and incubating for 20 minutes on ice. Actin filaments were stabilized with 5 μL phalloidin with an Alexa 532 tag (Life Technologies, A22282) and incubation in the dark for 1 hour on ice. Actin was then diluted 100x in a 10:1 GAB/APB buffer mixture.

For rupture experiments, a ~ 15 μL flow cell was constructed using a microscope slide, an etched coverslip, and double-stick tape. Diluted 1.25 μm streptavidin beads (SpheroTech, SVP-10-5) were added to the flow cell and incubated for 10 minutes to permit surface binding. Then, 10 mg/mL casein in 10:1 GAB/APB was added to remove any unbound beads and to block the remaining surface, allowing it to incubate for 10 minutes. Next, diluted biotinylated actin was added to the flow cell and incubated for 10 minutes to allow binding to surface-affixed beads. Finally, diluted streptavidin-coated core-shell particles in 10:1 GAB/APB were added to the flow cell and allowed to incubate for 10 minutes. Once the slide was loaded onto the trapping microscope, a self-assembled tether was found by finding a core-shell bead in close proximity to a surface bound streptavidin bead that was not diffusing away. To rupture the filament, the core-shell bead was trapped, and the

piezostage was translated in 200 nm increments at 2 $\mu\text{m}/\text{sec}$ until the tether was fully elongated to generate force by displacing the bead from the trap center. Single ruptures were identified through clean, uninterrupted breaks to baseline and the bead diffusing away upon release of the trap. Bead position and force were measured using custom-written LabVIEW algorithms [31].

5.4 Results and Discussion

5.4.1 Synthesis and Characterization of Core-Shell Particles

Using the synthetic strategy outlined in Figure 5.1, we provide a straightforward method for the synthesis of optical trapping handles with increased trapping stability. Our synthetic approach is considerably modified from work described in the literature and optimized to generate high trapping forces [32, 33, 34]. A representative image of the anatase cores is shown in Figure 5.2A. In the initial step, titania cores are synthesized by a nucleation reaction where the diameter of the cores is linearly dependent on the concentration of TBT used (Figure 5.2B). Using 2-3 mM TBT, we were able to synthesize cores with tightly controlled diameters between 400-800 nm. To determine the size of the particles, we found that particle diameters estimated using a scanning electron microscope (SEM) agreed well with measurements (normally less than 10% error) using a custom-built light microscope equipped with a 100X objective (1.4 numerical aperture, Nikon) and DIC. To calculate particle diameters, DIC images were used to measure the average diameter of a particular particle in pixels using the software ImageJ. With a predetermined pixel size of 23.75 nm/pixel for the CCD camera used (DAGE-MTI), we estimated the average diameter in nanometers for numerous beads per condition.

Since a mismatch in the index of refraction between the core ($n = 2.3$) [33] and shell ($1.6 < n < 1.8$) [33] materials is vital for enhanced trapping stability [17], Raman spectroscopy was utilized to confirm the anatase phase of the cores after calcination. Raman spectra show

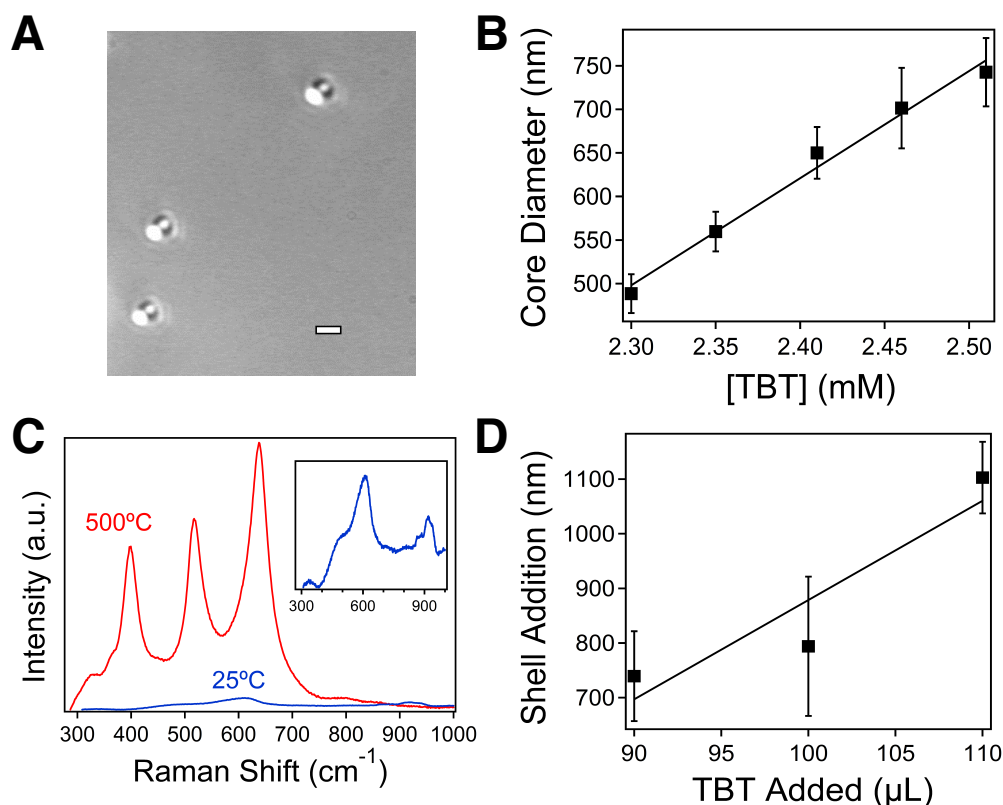


Figure 5.2: **Synthesis and characterization of core-shell particles.** (A) Image of anatase cores (scale bar, 500 nm) obtained using a light microscope with DIC. (B) Anatase core size increases with additional TBT utilized (avg. \pm std., N=30 per concentration measured). (C) Raman spectra for cores before (blue) and after (red) calcination showing the transition of titania to the anatase phase, seen as appearance of bands described in the text. (D) Size of shell thickness using different amounts of TBT in the reaction with no heating (avg. \pm std., N=10 per concentration measured).

the emergence of the characteristic peaks for anatase at 399, 519, and 639 cm^{-1} [25, 26] only upon heating the cores at 500°C (Figure 5.2C, red).

Coating of the anatase cores with amorphous titania shells was carried out at constant surfactant concentration, using varying concentrations of TBT precursor to dictate the shell thickness (Figure 5.2D). Previously, it had been suggested that a silica layer deposited on the surface of core-shells could provide a conjugation strategy to couple molecules of interest to the particles but was mainly used as a way to generate fluorophore-free luminescent beads upon calcination [33, 34]. However, silica coating of particles can be a tedious reaction and often leads to particle agglomeration and loss of functionality [35]. Instead, we

employed a silane functionalizer, MPTS, to incorporate thiol groups on the titania shell surface. Although thiol chemistry provides a convenient strategy for coupling to primary amines in biomolecules, other silane analogues can easily be used to enable different surface chemistries including amines and hydroxyls.

5.4.2 Particle Size and Trapping Stability are Temperature Dependent

The amorphous titania shell has an index of refraction of ~ 1.55 which is lower than the suggested $n=1.75$ for optimal trapping stability of the core-shell microparticles, as predicted by theory [17]. The index of refraction of titania, and concomitantly the size of the microparticle, can be tuned by heating. Upon heating at 50°C , the particle diameter decreased 15% within 15 minutes (Figure 5.3A). Thus, to synthesize core-shells with a final diameter of $0.9\text{-}1.1\ \mu\text{m}$ we started with core-shells $\sim 1.3\ \mu\text{m}$ in diameter prior to heating. Using a single beam optical trapping instrument, we characterized the trapping stability of the particles by comparing the trap stiffness at a constant laser power ($\sim 370\ \text{mW}$ at $1064\ \text{nm}$ before the objective), between the core-shell microparticles, and commercially available polystyrene beads of a similar size ($1.025\ \mu\text{m}$, $n=1.57$, Spherotech).

Polystyrene beads are the current gold standard in the field of single-molecule biophysics for optical trapping experiments, including at high forces [3]. We demonstrate here that our core-shell microparticles displayed higher trapping stiffness than the polystyrene beads, even in the absence of heating (Figure 5.3B). Upon heating, the change in density of the titania shell leads to an increase in index of refraction [33], and we observe a 3-4 times increase in trap stiffness for the core shells (Figure 5.3B). When heated for longer than 20 minutes, the core-shells were no longer trappable with a single beam trap, likely due to an increase in the scattering force [17]. These results demonstrate functionalized anatase-titania core-shell particles feature up to a 4-fold improvement in trapping stability compared to standard polystyrene beads.

There is a linear correlation between trap stiffness and core-shell bead diameter (also

associated with increased refractive index change with increased heating time, Figure 3C). For comparison, the trap stiffnesses of different sized polystyrene (1.09 μm , 2.192 μm , 6.7 μm ; Spherotech) and silica (0.97 μm , 2.32 μm , 4.09 μm ; Bangs Labs) were also measured (Figure 3C inset). The trap stiffness measurements are much lower than for our core-shell microparticles, and the stiffness decreases with increasing bead diameter. Here, we note that the correlation between bead diameter (d_{bead}) and trap stiffness is complex due to the measured bead sizes falling within different optic regimes. Most optical trapping applications fall into an intermediate regime ($d_{\text{bead}} \approx \lambda_{\text{trap}}$, here $\lambda_{\text{trap}} = 1064 \text{ nm}$) between Rayleigh ($d_{\text{bead}} \ll \lambda_{\text{trap}}$) and Mie ($d_{\text{bead}} \gg \lambda_{\text{trap}}$) scattering conditions [1]. As d_{bead} becomes greater than λ_{trap} , the trapping rays are spread out over a larger distance, causing a decrease in stiffness with increased d_{bead} [1, 36]. These results stress the importance of finely tuning the core-shell microparticle diameter and their overall improvement over conventional beads.

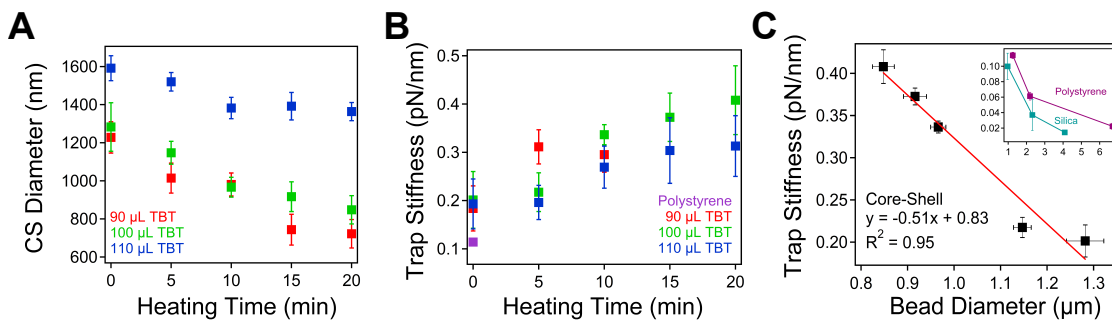


Figure 5.3: **Temperature dependence of core-shell particles.** (A) Average diameter of anatase-titania core-shell particles as a function of heating time at 50°C . Three separate batches of core-shells are plotted, with initial diameters ranging from $1.6 \mu\text{m}$ to $1.2 \mu\text{m}$, depending on the amount of TBT used (avg. \pm std., $N=10$ particles per heating measurement). (B) Average trapping stiffness for conventional polystyrene beads (P.S., diameter $\sim 1.25 \mu\text{m}$), and core-shells heated up to 20 minutes (avg. \pm std., $N=10$ particles per stiffness measurement). (C) Trap stiffness versus core-shell diameter correlation for $100 \mu\text{L}$ TBT. Inset: Trap stiffness (avg. \pm std, $N=10$ particles per measurement) of polystyrene (Spherotech) and silica (Bangs Labs) beads of different diameters.

5.4.3 Biophysical Experiments Using Core-Shell Particles

Since the core-shell microparticles surpassed the standard polystyrene beads in trapping stability, we then functionalized the microparticles with proteins to pursue two different high force assays. First, we coupled core-shell particles to the prion protein Sup35 labeled with an Alexa555 fluorescent tag. We chose to use the Sup35 protein, produced in *Saccharomyces cerevisiae*, due to its involvement in amyloid fibril formation [3]. As demonstrated by Dong *et al.* and Castro *et al.*, single amyloid fibers, which form aggregates in neurodegenerative diseases such as Alzheimer's, have a shockingly large modulus, greater than that of spider silk [3, 4]. Amyloid fiber stability and strength have been of interest to the biophysics and medical fields investigating mechanisms of prion diseases [37]. In Dong *et al.*, an optical trap was used to unfold and rupture amyloid fibers. However, a conventional optical trap required a denaturing reagent to rupture fibers [3]. The core-shell particles synthesized in this study are well suited for this experiment that requires greater force than previously attained.

Here, we used sulfo-SMCC to covalently crosslink the amine-terminus of Sup35 fluorescently labeled with Alexa555 to surface exposed thiol groups on the core-shells. Sup35 coated core-shells were imaged using DIC and TIRF microscopy (Figure 5.4A-C). Fluorescence intensity of the core-shells decreased with time due to photobleaching of the Alexa555 dye, suggesting the Sup35 protein successfully bound the core-shell surface. The same process was successfully carried out to covalently bind streptavidin to the core-shell surface. Given the ubiquitous use of biotinylated proteins, nucleic acids, and molecular motors in single-molecule experiments, streptavidin coated core-shells can be easily introduced into well-developed assays to probe biomolecule mechanics and activity (e.g. ClpXP mechanical protein degradation [38], protein folding- unfolding [39]).

We performed a surface-tethered amyloid fiber assay using our core-shell titania microparticles functionalized with streptavidin and subsequently conjugated with biotinylated NM monomer (methods). A schematic of the assay is shown in Figure 5.5A. Upon the se-

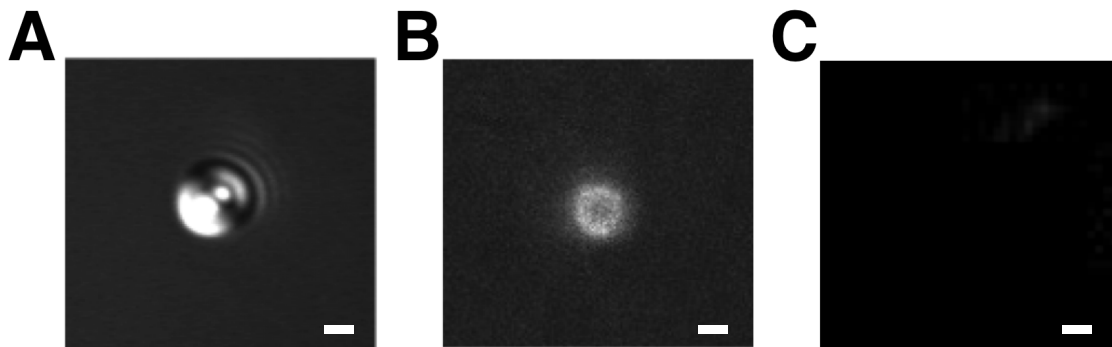


Figure 5.4: **Fluorophore addition to core-shell particles.** (A) DIC image of anatase-titania core-shell particles coated with Sup35 proteins. (B) TIRF microscopy images show fluorescence emission of the Alexa555 dye on the surface-bound Sup35 protein. The fluorescence intensity from the beads decreased with time due to photobleaching of the dye. (C) Fluorescence image of streptavidin coated core-shell particle with no dye. No autofluorescence was observed. Scale bar: 500 nm.

quential bottom-up assembly of core shell-fiber tethers, a piezostage was translated against a trapped bead to elongate and concomitantly impart force on the fiber (Figure 5.5B). As the microparticle is pulled away from the focus of the optical trap, the force across the fiber is above 100 pN, and multiple domains of the fiber unfold. This leads to sharp decreases in bead position as the bead moves closer to the trap center (Figure 5.5C). This lessens the force on the fiber continually until no more events are observed at the end of the trace. The same tether was pulled again (Figure 5.5D), and as a significant amount of force is imparted on the partially unfolded fiber, complete rupture is observed. Evidence of this was found by a clean rupture to baseline (corresponding to the trap center) and the bead being able to freely move away from the coverslip surface when the trap was turned off at the conclusion of the trace. These experiments demonstrate our core-shell particles functionalized with NM monomer can be used in high force assays to study the mechanics of individual amyloid fibers, and the streptavidin coated microparticles can easily be implemented into well-established biophysical assays.

To further demonstrate the capabilities of bio-functionalized core-shell beads, an actin rupture assay was performed. Actin is a major cytoskeletal component that is responsi-

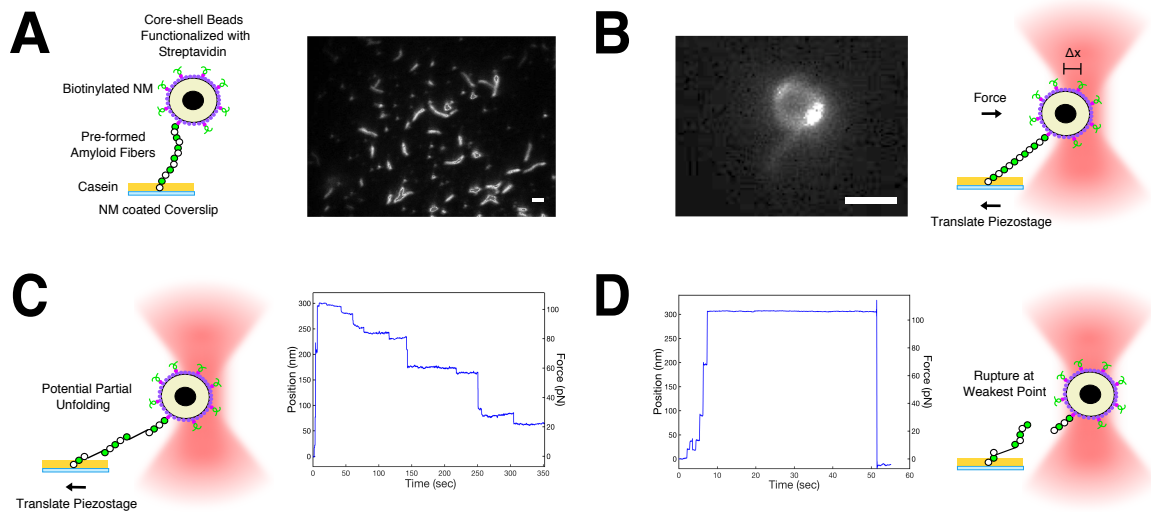


Figure 5.5: Amyloid pulling assay using core-shell particles. (A) Core-shell particles were tethered to a coverslip surface by an amyloid fiber as described previously [3, 4]. NM monomers were non-specifically bound to a coverslip, which was subsequently coated in casein. Pre-formed fluorescent fibers were then added to the flow cell and self-assembled with unfolded monomer on the surface. The fluorescence image shows fibers attached to the surface via monomers (higher concentration than used in pulling assay). Core-shell particles were functionalized with streptavidin using sulfo-SMCC crosslinking and then incubated with biotinylated monomer. (B) Beads coated in monomer and fluorescent monomer were used to image an amyloid fiber tethered to the surface. Once a tether was found, the piezostage was translated to generate force on the fiber. (C) Unfolding events were observed from pulling on the fiber. As the tether becomes longer from unfolding, the bead drifts back to the trap center. (D) After a sustained dwell for more than 40 seconds, at 100 pN, the tether ruptured. Scale bar: 1 μm .

ble for much of the structure inside of a cell, and its polymerization drives cell motility [41]. Due to the high levels of load an actin network bears in the cell, investigation of its mechanical properties would yield biophysical insight into the cell's force balance mechanisms. The tensile strength of actin has been investigated previously using a pair of glass microneedles [16, 42, 43], microfabricated cantilevers [44], and optical tweezers under low force (0-8 pN) [40]. Kishino *et al.* ruptured an actin filament using glass needles and found the tensile strength to be 108 pN without and 117 pN with tropomyosin, both of which were independent of filament length [42]. Here, core-shell particles were utilized to rupture actin filaments in an optical trapping assay. As shown in Figure 5.6A, core-shells

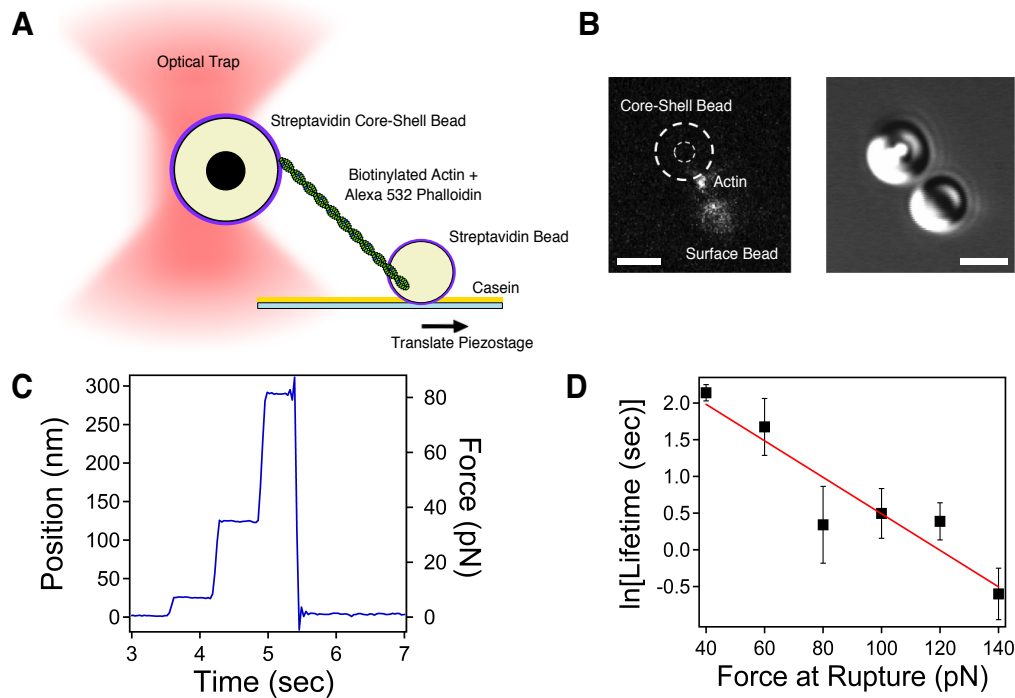


Figure 5.6: **Actin rupture assay.** (A) Assay schematic. (B) Fluorescence visualization of tether formation between a streptavidin-coated core-shell bead and a surface bound streptavidin bead. (C) Example actin rupture trace using beads at a trap stiffness of ~ 0.3 pN/nm. (D) Linear relationship between the $\ln(\text{lifetime})$ and rupture force, following the Bell model for bond lifetimes [40]. $N=10$. Error bars: SEM.

were functionalized with streptavidin, as described earlier, and used to form tethers with single biotinylated actin filaments attached to surface bound streptavidin polystyrene beads (Methods). As the phalloidin stabilizer was labeled with Alexa 532, tether formation was confirmed using fluorescence (Figure 5.6B). Figure 5.6C shows an example rupture trace of an actin filament using core-shell beads at a trap stiffness of ~ 0.3 pN/nm (see also Figure 5.3B), with an average rupture force of $90.8 \text{ pN} \pm 26 \text{ pN}$ (avg. \pm std., $N=10$). These rupture forces are similar to that of Kishino *et al.* [42]. The lifetime of the event (time between total filament elongation and rupture) decreases exponentially with rupture force, following the Bell model for bond lifetimes [45]. While more extensive analysis of actin strength is required, this assay demonstrates core-shell beads' ability to be utilized in high force biological experiments.

5.5 Conclusions

Here we provide a synthetic strategy for making optical trapping handles that display increased trapping stability, detailing how to control the size and refractive index. These handles are composed of a high-refractive-index anatase cores coated with an anti-reflection titania shell. By introducing a silane functionalizer to the particle surface, we provide a straightforward method for covalently coupling protein structures. We anticipate this approach will broaden the use of these next-generation trapping handles in experiments probing mechanically stable biological interactions/structures, such as studying the mechanics of amyloid fibrils or other high force experiments previously not possible with an optical trap. Furthermore, these particles are promising candidates for use in combined optical trapping and fluorescence approaches where decreasing trapping laser intensity, without sacrificing trapping stiffness, can provide longer fluorophore lifetimes [18].

5.6 Acknowledgements

The authors would like to thank Susan Lindquist for advice and amyloid fiber materials and Yu-Chuan Ou for assistance with acquiring Raman spectra. This material is based upon work supported by the National Science Foundation Graduate Research Fellowship Program under Grant No. 1445197 (D.N.R.). J.C.C. was supported in part by a GAANN fellowship from the US Department of Education under grant no. P200A090323. This work was also supported, in part, by the Singapore-MIT Alliance for Research and Technology?BioSyM and NSF Grant No. 1330792 (M.J.L.).

5.7 Bibliography

- [1] Keir C Neuman and Steven M Block. Optical trapping. *Review of scientific instruments*, 75(9):2787–2809, 2004.
- [2] Furqan M Fazal and Steven M Block. Optical tweezers study life under tension. *Nature photonics*, 5(6):318–321, 2011.
- [3] Jijun Dong, Carlos E Castro, Mary C Boyce, Matthew J Lang, and Susan Lindquist. Optical trapping with high forces reveals unexpected behaviors of prion fibrils. *Nature structural & molecular biology*, 17(12):1422–1430, 2010.
- [4] Carlos E Castro, Jijun Dong, Mary C Boyce, Susan Lindquist, and Matthew J Lang. Physical properties of polymorphic yeast prion amyloid fibers. *Biophysical journal*, 101(2):439–448, 2011.
- [5] JP Mills, M Diez-Silva, DJ Quinn, M Dao, MJ Lang, KSW Tan, CT Lim, G Milon, PH David, O Mercereau-Puijalon, et al. Effect of plasmodial resa protein on deformability of human red blood cells harboring plasmodium falciparum. *Proceedings of the National Academy of Sciences*, 104(22):9213–9217, 2007.
- [6] Ying Hu, Timo A Nieminen, Norman R Heckenberg, and Halina Rubinsztein-Dunlop. Antireflection coating for improved optical trapping. *Journal of Applied Physics*, 103(9):093119, 2008.
- [7] Astrid van der Horst, Peter DJ van Oostrum, Alexander Moroz, Alfons van Blaaderen, and Marileen Dogterom. High trapping forces for high-refractive index particles trapped in dynamic arrays of counterpropagating optical tweezers. *Applied optics*, 47(17):3196–3202, 2008.
- [8] Michael Bugiel, Horatiu Fantana, Volker Bormuth, Anastasiya Trushko, Frederic Schiemann, Jonathon Howard, Erik Schäffer, and Anita Jannasch. Versatile micro-

- sphere attachment of gfp-labeled motors and other tagged proteins with preserved functionality. *Journal of Biological Methods*, 2(4):e30, 2015.
- [9] Mark J Schnitzer, Koen Visscher, and Steven M Block. Force production by single kinesin motors. *Nature cell biology*, 2(10):718, 2000.
- [10] Jorge M Ferrer, Hyungsuk Lee, Jiong Chen, Benjamin Pelz, Fumihiko Nakamura, Roger D Kamm, and Matthew J Lang. Measuring molecular rupture forces between single actin filaments and actin-binding proteins. *Proceedings of the National Academy of Sciences*, 105(27):9221–9226, 2008.
- [11] Michelle D Wang, Hong Yin, Robert Landick, Jeff Gelles, and Steven M Block. Stretching dna with optical tweezers. *Biophysical journal*, 72(3):1335–1346, 1997.
- [12] Douglas E Smith, Sander J Tans, Steven B Smith, Shelley Grimes, et al. The bacteriophage phi29 portal motor can package dna against a large internal force. *Nature*, 413(6857):748, 2001.
- [13] Hyungsuk Lee, Jorge M Ferrer, Matthew J Lang, and Roger D Kamm. Molecular origin of strain softening in cross-linked f-actin networks. *Physical Review E*, 82(1):011919, 2010.
- [14] Jason P Rich, Jan Lammerding, Gareth H McKinley, and Patrick S Doyle. Nonlinear microrheology of an aging, yield stress fluid using magnetic tweezers. *Soft Matter*, 7(21):9933–9943, 2011.
- [15] Keir C Neuman and Attila Nagy. Single-molecule force spectroscopy: optical tweezers, magnetic tweezers and atomic force microscopy. *Nature methods*, 5(6):491–505, 2008.
- [16] H Kojima, A Ishijima, and T Yanagida. Direct measurement of stiffness of single actin

- filaments with and without tropomyosin by in vitro nanomanipulation. *Proceedings of the National Academy of Sciences*, 91(26):12962–12966, 1994.
- [17] Anita Jannasch, Ahmet F Demirörs, Peter DJ Van Oostrum, Alfons Van Blaaderen, and Erik Schäffer. Nanonewton optical force trap employing anti-reflection coated, high-refractive-index titania microspheres. *Nature Photonics*, 6(7):469–473, 2012.
- [18] Erwin JG Peterman, Frederick Gittes, and Christoph F Schmidt. Laser-induced heating in optical traps. *Biophysical journal*, 84(2):1308–1316, 2003.
- [19] Valentina Ferro, Aaron Sonnberger, Mohammad K Abdosamadi, Craig McDonald, Erik Schäffer, and David McGloin. Improved antireflection coated microspheres for biological applications of optical tweezers. In *Optical Trapping and Optical Micro-manipulation XIII*, volume 9922, page 99222T. International Society for Optics and Photonics, 2016.
- [20] Derek Craig, Alison McDonald, Michael Mazilu, Helen Rendall, Frank Gunn-Moore, and Kishan Dholakia. Enhanced optical manipulation of cells using antireflection coated microparticles. *ACS Photonics*, 2(10):1403–1409, 2015.
- [21] Matthew J Lang, Polly M Fordyce, and Steven M Block. Combined optical trapping and single-molecule fluorescence. *Journal of biology*, 2(1):6, 2003.
- [22] Peter B Tarsa, Ricardo R Brau, Mariya Barch, Jorge M Ferrer, Yelena Freyzon, Paul Matsudaira, and Matthew J Lang. Detecting force-induced molecular transitions with fluorescence resonant energy transfer. *Angewandte Chemie International Edition*, 46(12):1999–2001, 2007.
- [23] Meindert A van Dijk, Lukas C Kapitein, Joost van Mameren, Christoph F Schmidt, and Erwin JG Peterman. Combining optical trapping and single-molecule fluorescence spectroscopy: enhanced photobleaching of fluorophores. *The Journal of Physical Chemistry B*, 108(20):6479–6484, 2004.

- [24] Martina H Stenzel. Bioconjugation using thiols: old chemistry rediscovered to connect polymers with nature's building blocks, 2012.
- [25] Toshiaki Ohsaka, Fujio Izumi, and Yoshinori Fujiki. Raman spectrum of anatase, TiO_2 . *Journal of Raman spectroscopy*, 7(6):321–324, 1978.
- [26] WF Zhang, YL He, MS Zhang, Z Yin, and Q Chen. Raman scattering study on anatase TiO_2 nanocrystals. *Journal of Physics D: Applied Physics*, 33(8):912, 2000.
- [27] Caroline A Schneider, Wayne S Rasband, and Kevin W Eliceiri. Nih image to imagej: 25 years of image analysis. *Nature methods*, 9(7):671–675, 2012.
- [28] William R Hesse, Miriam Steiner, Matthew L Wohlever, Roger D Kamm, Wonmuk Hwang, and Matthew J Lang. Modular aspects of kinesin force generation machinery. *Biophysical journal*, 104(9):1969–1978, 2013.
- [29] Matthew J Lang, Charles L Asbury, Joshua W Shaevitz, and Steven M Block. An automated two-dimensional optical force clamp for single molecule studies. *Biophysical journal*, 83(1):491–501, 2002.
- [30] Daniel A Balikov, Sonia K Brady, Ung Hyun Ko, Jennifer H Shin, Jose M de Pereda, Arnoud Sonnenberg, Hak-Joon Sung, and Matthew J Lang. The nesprin-cytoskeleton interface probed directly on single nuclei is a mechanically rich system. *Nucleus*, pages 1–14, 2017.
- [31] Ahmad S Khalil, David C Appleyard, Anna K Labno, Adrien Georges, Martin Karplus, Angela M Belcher, Wonmuk Hwang, and Matthew J Lang. Kinesin's cover-neck bundle folds forward to generate force. *Proceedings of the National Academy of Sciences*, 105(49):19247–19252, 2008.
- [32] Hyung Kyun Yu, Gi-Ra Yi, Ji-Hwan Kang, Young-Sang Cho, Vinodhan N Manoharan,

- David J Pine, and Seung-Man Yang. Surfactant-assisted synthesis of uniform titania microspheres and their clusters. *Chemistry of Materials*, 20(8):2704–2710, 2008.
- [33] Ahmet Faik Demirörs, Anita Jannasch, Peter D J van Oostrum, Erik Schäffer, Arnout Imhof, and Alfons van Blaaderen. Seeded growth of titania colloids with refractive index tunability and fluorophore-free luminescence. *Langmuir*, 27(5):1626–34, Mar 2011.
- [34] Ahmet Faik Demirörs, Alfons van Blaaderen, and Arnout Imhof. Synthesis of eccentric titania- silica core- shell and composite particles. *Chemistry of Materials*, 2009.
- [35] Bhuvnesh Bharti, Jens Meissner, Sabine HL Klapp, and Gerhard H Findenegg. Bridging interactions of proteins with silica nanoparticles: The influence of ph, ionic strength and protein concentration. *Soft Matter*, 10(5):718–728, 2014.
- [36] Robert M Simmons, Jeffrey T Finer, Steven Chu, and James A Spudich. Quantitative measurements of force and displacement using an optical trap. *Biophysical journal*, 70(4):1813–1822, 1996.
- [37] Michael Schleegeer, Tanja Deckert-Gaudig, Volker Deckert, Krassimir P Velikov, Gijssje Koenderink, Mischa Bonn, et al. Amyloids: From molecular structure to mechanical properties. *Polymer*, 54(10):2473–2488, 2013.
- [38] Marie-Eve Aubin-Tam, Adrian O Olivares, Robert T Sauer, Tania A Baker, and Matthew J Lang. Single-molecule protein unfolding and translocation by an atp-fueled proteolytic machine. *Cell*, 145(2):257–267, 2011.
- [39] Dustin B Ritchie and Michael T Woodside. Probing the structural dynamics of proteins and nucleic acids with optical tweezers. *Curr Opin Struct Biol*, 34:43–51, Oct 2015.

- [40] D E Dupuis, W H Guilford, J Wu, and D M Warshaw. Actin filament mechanics in the laser trap. *J Muscle Res Cell Motil*, 18(1):17–30, Feb 1997.
- [41] A Mogilner and G Oster. Cell motility driven by actin polymerization. *Biophys J*, 71(6):3030–45, Dec 1996.
- [42] A Kishino and T Yanagida. Force measurements by micromanipulation of a single actin filament by glass needles. *Nature*, 334(6177):74–6, Jul 1988.
- [43] Y Tsuda, H Yasutake, A Ishijima, and T Yanagida. Torsional rigidity of single actin filaments and actin-actin bond breaking force under torsion measured directly by in vitro micromanipulation. *Proc Natl Acad Sci U S A*, 93(23):12937–42, Nov 1996.
- [44] Xiumei Liu and Gerald H Pollack. Mechanics of f-actin characterized with microfabricated cantilevers. *Biophys J*, 83(5):2705–15, Nov 2002.
- [45] G I Bell. Models for the specific adhesion of cells to cells. *Science*, 200(4342):618–27, May 1978.

CHAPTER 6

CONCLUSIONS AND FUTURE WORK

The studies in this dissertation have revealed mechanistic insight regarding how kinesins Kif15 and HSET are able to rescue bipolar mitotic spindle assembly under drugged or pathological conditions. Kif15 is able to replace the function of Eg5 when it has been inhibited by acting as a MT slider to aid in separating centrosomes. HSET re-establishes spindle bipolarity by focusing MT minus ends when centrosome number is not two, as is the case with many cancers. While both of these kinesins have force balancing roles under physiological conditions, their inhibition does not have much effect. However, under pathological or drugged conditions where their counterparts, Eg5 or two centrosomes, have been disturbed, then these backup mechanisms become vital to cell sustainability. This makes both Kif15 and HSET attractive cancer therapy targets.

To understand how a dimeric motor can replace the function of a tetramer, the mechanical properties and force generation capabilities of Kif15 were investigated using optical tweezers. Measurements of motor subdomains, single motors, and motor-microtubule bundles paired with stochastic simulations unveiled a mechanism for how Kif15 can rescue Eg5 function under chemotherapeutic conditions. It was found that Kif15's non-motor MT binding domain was stronger than the stall force of the motor, revealing that this motor has the ability to build up mechanical strain and slide MTs apart. However, single motor interactions on single MTs do not fully reflect the complex spindle structure in which Kif15 works. In order to reconstitute a more native environment, a new and novel assay was developed to evaluate Kif15 function in bundled assemblies. It was determined that Kif15 slides anti-parallel MTs apart while parallel bundles remain stationary. This is reflective of the location-specific roles that Kif15 plays in the spindle: static MT crosslinker/force regulator under physiological conditions (parallel kinetochore MTs) and active MT slider

under drugged conditions (anti-parallel interpolar MTs). These studies illuminate the therapeutic importance of Kif15, whose inhibition in tandem with an Eg5 poison could prove to be more effective at halting cancer in the clinic.

Another redundant backup mechanism involves pole focusing of the mitotic spindle by HSET. The single molecule mechanics of HSET were investigated here using optical trapping to give insight about how a previously defined non-processive motor, or cannot walk along a MT without diffusing away, could accomplish macroscopic force generation during mitosis. Constructs containing various sub-components of the motor were utilized to determine the role of each domain, and step size, dwell times, and stall forces were measured. Rupture assays were also performed on the ATP-independent tail domain to determine the strength of the interaction with MTs. We showed that HSET has a processive nature with the ability to complete multiple steps along a MT before release. Moreover, the tail binding domain of HSET and its interaction with the negatively charged E-hook tail of tubulin is necessary for long-range processivity. To further investigate the role of HSET in spindle mechanics and force balance, an optical tweezer assay was utilized to evaluate HSET force generation in MT bundles (alone and with Eg5), and we found that it acts as a force brake against Eg5, the main MT slider, *in vitro*. The motor's ability to crosslink and slide MTs, as well as its processive nature, suggest that HSET is able to discriminate between different cellular environments. This reflects its conditional ability to be physiologically relevant when centrosome number is not two, making it an attractive cancer therapy target.

Future work on these mitotic motors includes both therapeutic and further mechanistic investigations. The Ohi lab has been working to screen small molecules that would specifically inhibit Kif15. A few strong candidates have been discovered that significantly slow down or halt MT gliding. Further investigation with an optical trapping assay should be performed to determine how force generation is affected in a dose-response type manner when incubated with the candidate molecule. Optimization of the small molecule could

also be performed by changing out specific atoms or functional groups to see if it becomes more or less effective at inhibiting Kif15. This would also give insight about how the small molecule is specifically targeting the motor and disrupting its action.

Initial force generation studies of Kif15 with beads attached to the N-terminus (or the motor head) revealed interesting results. Both 8 and 16 nm steps were observed. If the bead is attached to one motor head, then, in theory, the data should reveal only 16 nm steps. The 8 nm transitions suggest that Kif15 may be generating force through the cover-neck bundle. An antibody was developed to target the coverstrand of Kif15, and initial studies suggested that it specifically inhibited Kif15 motility.

However, delivery of antibodies is difficult. Therefore, DNA aptamer development was pursued in collaboration with Ethan Lippmann's lab at Vanderbilt. A synthetic peptide of the Kif15 coverstrand sequence was purchased and given to the Lippmann lab for screening against a library of nucleic acid sequences. Those that show any binding affinity would be screened further to find the highest affinity peptide. The peptide would also be screened against kinesin-1 and Eg5 to ensure target specificity. The Lippmann lab is still developing and optimizing their screening setup. Once it is finished, the discovered high affinity peptide would be tested in unloaded assay to test its efficacy in halting Kif15 motility. To test its targeting ability to the cover-neck bundle, an assay with synthetic peptides of the neck linker would be employed. The neck linker peptide would be synthesized with a fluorescent tag. The coverstrand would be adhered by one end to a coverslip surface. The fluorescently tagged neck linker would then be flowed in and allowed to incubate with the coverstrand. Fluorescence microscopy would then be used to confirm the binding of the neck linker to the coverstrand. If all of these methods prove effective in inhibiting Kif15, *in vivo* studies would be pursued with Eg5 independent cell lines to see if mitosis continues in the presence of the selected aptamer.

In addition, a detailed synthetic strategy was developed for core-shell particles for high force optical trapping experiments. Covalent biofunctionalization capacity was added to

these beads for ease of use in biological assays. Now that these beads can be reliably synthesized in our lab, their potential applications have a wide range. The strength of individual amyloid fibers is still unexplored because their apparent rupture force exceeds that of conventional optical traps. Core-shell beads should remedy this issue. Initial results show significant unfolding events in individual fibers before final rupture. These unfoldings and range of rupture forces should be evaluated further. Other applications include using core-shell particles to evaluate the strength of other biological polymers, such as actin and microtubules, and the triggering capacity of T-cells.

From the perspective of the single molecule biophysics field as a whole, one challenge prevalent is reconstituting a motor-filament environment that reflects physiological function. The vast majority of studies use isolated, reductionist geometries, such as a single motor/protein interacting with a single filament. However, as outlined in Chapters 2 and 4, a MT bundle assay was developed to evaluate how more than one kinesin can work together in a crosslinked structure, as they would be within the cell, measuring force generation rates and capacity. The bundle assay was extended to involve two different kinesins that coexist in the spindle to evaluate how they regulate each other's force generation capabilities. To date, this has been one of the only assays where optical trapping and fluorescence have been utilized to investigate force generation in higher motor-filament architectures.

The future of the field will be utilizing engineered assays that will be employed to design, build, and probe other motor-filament mechanics that have not been investigated at higher levels *in vitro*. The bundle assay could be extended to not only include more complex structural hierarchy, but also explore the effects of external signals and targeted therapeutics. If physiologically relevant architectures can be reconstituted, then we can evaluate what happens to specific motors, filaments, proteins, etc. under drugged conditions in a dose-response type manner, which has a mechanistic comprehension advantage over bulk, cell-level testing.

APPENDIX A

PROTOCOLS

A.1 Buffer Recipes

1. PEM80, pH 6.9

To be used in microtubule and motor assays (Chapter 2)

Materials:

PIPES

EGTA

MgCl₂

KOH

Deionized water

(a) Prepare 250 mL of PEM80 by mixing:

6.048 g PIPES

95.1 mg EGTA

204.1 μ L of 4.9 M MgCl₂ into 250 mL final volume

(b) Add small volumes of concentrated KOH solution to adjust the pH to 6.9.

2. PEM104, pH 6.9

To be used in microtubule and motor assays (Chapter 2)

Materials:

PIPES

EGTA

MgCl₂

KOH

Deionized water

(a) Prepare 100 mL of PEM104 by mixing:

3.133 g PIPES

49.452 mg EGTA

128.57 μ L of 4.9 M MgCl₂ into 100 mL final volume

(b) Add small volumes of concentrated KOH solution to adjust the pH to 6.9.

3. 5X BRB80, pH 6.8

To be used in microtubule gliding assays (Chapter 2)

Materials:

PIPES

EGTA

MgCl₂

KOH

Deionized water

(a) Prepare 250 mL of 5X BRB80 by mixing:

30.237 g PIPES

0.4755 g EGTA

0.119 g MgCl₂ 100 mL final volume

(b) Add small volumes of concentrated KOH solution to adjust the pH to 6.8.

4. Wash Buffer

To be used in microtubule gliding assays (Chapter 2)

Materials:

Deionized water

5X BRB80

200 mM MgCl₂

200 mM ATP

5 mg/mL casein (Blotting Grade Blocker)

(a) Prepare by mixing:

388.125 μ L water

112.5 μ L 5X BRB80

2.8 μ L 200 mM MgCl₂

2.8 μ L 200 mM ATP

56.25 μ L 5 mg/mL casein

5. 10X Oxygen Scavenging (OS) Buffer/Mix

To be used in microtubule gliding assays (Chapter 2)

Materials:

1X BRB80

50% β -mercaptoethanol (BME) 3.5 mg/mL catalase

20 mg/mL glucose oxidase

450 mg/mL β -D-glucose

- (a) Prepare by mixing:
 - 22.5 μL 1X BRB80
 - 3.75 μL BME
 - 3.75 μL catalase
 - 3.75 μL glucose oxidase
 - 3.75 μL glucose

6. Flow Cell Buffer

To be used in microtubule gliding assays (Chapter 2)

Materials:

Deionized water
5X BRB80
200 mM MgCl_2
200 mM ATP
5 mg/mL casein (Blotting Grade Blocker)
OS mix

- (a) Prepare by mixing:
 - 177 μL water
 - 60 μL 5X BRB80
 - 1.5 μL 200 mM MgCl_2
 - 1.5 μL 200 mM ATP
 - 30 μL 5 mg/mL casein
 - 30 μL 10X OS mix

7. 0.1 M MES buffer with 0.01% tween-20, pH 4.5

To be used in the preparation of anti-DIG and anti-His beads using EDC chemistry.

Materials:

MES
Tween-20

- (a) Prepare 100 mL of buffer by mixing the following:
 - 1.95 mg MES
 - 10 μL Tween-20 deionized water up to 100 mL total volume
- (b) pH adjust the solution to 4.5.

8. 0.1 M borate buffer, pH 8.5

To be used in the preparation of anti-DIG and anti-His beads using EDC chemistry.

Materials:

Boric Acid

Deionized water

- (a) Prepare 100 mL of buffer by mixing the following:
 - 0.618 g boric acid
 - deionized water up to 100 mL total volume
- (b) pH adjust the solution to 8.5 using NaOH.

9. 1X PBST, pH 7.4

To be used in the preparation of anti-DIG and anti-His beads using EDC chemistry.

Materials:

NaCl

KCl

Na₂HPO₄

KH₂PO₄

Tween-20

Deionized water

- (a) Prepare by mixing the following:
 - 8 g NaCl
 - 0.2 g KCl
 - 1.44 g Na₂HPO₄
 - 0.24 g KH₂PO₄
 - 100 μL Tween-20
 - 800 mL water
- (b) pH adjust the solution to 7.4 using KOH.

10. 1X CRBB, pH 7.2

To be used in the preparation amyloid fibers and NM beads.

Materials:

KPO₄

NaCl

Deionized water

- (a) Prepare by mixing the following:
 - 68 mg KPO₄
 - 0.8766 g NaCl

100 mL water

(b) pH adjust the solution to 7.2 using KOH.

11. 1X CRBB + 5 mM TCEP

To be used in the preparation amyloid fibers and NM beads.

Materials:

TCEP

CRBB

(a) Prepare by mixing the following:

1.25 mg TCEP

1 mL water

12. 6 M GdnHCl

To be used in the preparation amyloid fibers and NM beads.

Materials:

GdnHCl

Deionized water

(a) Prepare by mixing the following:

0.573 g GdnHCl

1 mL water

13. Solution T

To be used in TC and FC buffer preparation.

Materials:

Tris-HCl

CaCl₂

Deionized water

(a) In a 50 mL Falcon tube, add:

3.940 g Tris-HCl

0.147 g CaCl₂

(b) Add deionized water to 50 mL total volume and mix well. (500 mM Tris-HCl and 20 mM CaCl₂)

(c) Label Solution T and store at 4°C.

14. TC Buffer

To be used in preparation of GAB buffer.

Materials:

Solution T

Deionized water

(a) Add 40 mL of deionized water and 1.5 mL of Solution T to a 50 mL Falcon tube. Mix well.

(b) Adjust the pH to 8.0 by adding small volumes of concentrated KOH. (Usually add 4-5 pellets of KOH to a 50 mL Falcon tube, fill with deionized water, and use this to adjust pH)

(c) Add water to a final volume of 50 mL and verify the pH. Adjust pH if necessary.

(d) Filter the buffer using 0.2 μm membrane filters.

(e) Label the tube TC and store at 4°C. (5 mM Tris-HCl (pH 8) and 0.2 mM CaCl_2)

15. FC Buffer

To be used in preparation of GAB buffer.

Materials:

Solution T

KCl

MgCl_2

Deionized water

(a) Mix:

85 mL of deionized water

10 mL of Solution T

3.728 g KCl

0.0406 g MgCl_2

(b) Adjust the pH to 7.5 by adding small volumes of concentrated KOH. (Usually add 4-5 pellets of KOH to a 50 mL Falcon tube, fill with deionized water, and use this to adjust pH)

- (c) Add water to a final volume of 100 mL and verify the pH. Adjust pH if necessary.
- (d) Filter the buffer using 0.2 μm membrane filters.
- (e) Label the tube FC and store at 4°C. (50 mM Tris-HCl (pH 7.6), 500 mM KCl, 2 mM MgCl₂, and 2 mM CaCl₂)

16. GAB (General Actin Buffer)

Materials:

TC buffer

ATP

DTT

- (a) Mix:
 - 485 μL of TC buffer
 - 10 μL of 10 mM ATP
 - 5 μL of 50 mM DTT
 - Final concentration: 5 mM Tris-HCl, 0.2 mM CaCl₂, 0.5 mM DTT, 0.2 mM ATP
- (b) Label as GAB and store at 4°C.

17. APB (Actin Polymerization Buffer)

Materials:

FC buffer

ATP

DTT

- (a) Mix:
 - 455 μL of FC buffer
 - 25 μL of 100 mM ATP
 - 20 μL of 50 mM DTT
 - Final concentration: 50 mM Tris-HCl, 500 mM KCl, 2 mM MgCl₂, 2 mM CaCl₂, 2 mM DTT, 5 mM ATP
- (b) Label as APB and store at 4°C.

A.2 Microtubule Preparation

This procedure is used to prepare microtubules for kinesin-based assays (Chapter 2 and 3).

Materials:

PEM80

PEM104

10 mM GTP (Cytoskeleton BST06)

65 g/L NaN₃ (Sigma S-8032)

10 mM Taxol (Cytoskeleton TXD01, originally in powder form, reconstituted in 20 μ L DMSO to make 10 mM, stable for 6 months if stored at -20°C

DMSO (comes with Taxol and Tubulin)

Tubulin (Cytoskeleton TL238 bovine, reconstitute in 25 μ L PEM80 supplemented with 1 mM GTP, 5 μ L aliquots of 10 mg/mL

1. Combine 13 μ L PEM 104, 2.2 μ L 10 mM GTP, and 2.2 μ L DMSO; vortex.
2. Add 4.8 μ L 10 mg/mL non-labeled tubulin.
3. Place solution in water bath at 37°C for 40 minutes.
4. Create STAB solution: 38.6 μ L PEM80, 0.5 μ L 100 mM GTP, 4.7 μ L 65 g/L NaN₃, 1.2 μ L 10 mM Taxol, 5 μ L DMSO. Store on ice.
5. Remove from water bath, and add 2 μ L room temperature STAB solution. Placing MTs on ice or mixing with ice cold solution will cause MT depolymerization.
6. Store MTs at room temperature.

A.3 E-hook Cleaved Microtubule Preparation by Subtilisin Digestion

This protocol makes microtubules with the negatively-charged C-terminal tail of MTs, or the E-hook, cleaved by the protease subtilisin.

Materials:

Prepared microtubules

Subtilisin (Sigma P8038-50mg)

PEM80

Nanodrop

PMSF (Sigma)

1. Dissolve 7 mg subtilisin in 700 μL PEM80.
2. Determine the concentration using UV-Vis on Nanodrop. Either measure absorption at 260 nm ($\epsilon = 33350 \text{ M}^{-1}\text{cm}^{-1}$; $c=A/\epsilon$) or 280 nm ($\epsilon = 23740 \text{ M}^{-1}\text{cm}^{-1}$; $c=A/\epsilon$).
3. Dilute this stock solution to 20 μM for SubA or 7.5 μM for SubB with PEM80.
4. Make MTs as normal.
5. To prepare dTUB (alpha and beta E-hook removed), combine 7.5 μL TUB with 0.75 μL SubA (stock concentration 20 μM). Place in water bath at 37°C for 40 minutes.
6. To prepare β -dTUB (only beta E-hook remaining, alpha is cleaved), combine 7.5 μL TUB with 0.75 μL SubB (stock concentration 7.5 μM). Place in water bath at 37°C for 40 minutes.
7. To stop digestion, prepare 20 mM PMSF: 3.5 mg PMSF in 1 mL DMSO. Add 0.8 μL PMSF at room temperature to dTUB or β -dTUB.
8. Add 2 μL of room temperature STAB to all MT solutions.
9. Store digested MTs at room temperature.

A.4 Polarity-Marked Microtubule Preparation

This protocol makes Taxol-stabilized fluorescent MTs where the minus end is denoted by a much brighter fluorescent seed, and a dimmer elongation grows from it denoting the plus end. Based off of protocol found in “Preparation of marked microtubules for the assay of the polarity of microtubule-based motors by fluorescence” by A. A. Hyman in the Journal of Cell Science (1991).

Materials:

PEM80

PEM104

STAB

Tubulin

Rhodamine tubulin (Cytoskeleton TL590M)

GMPCPP (Jena Bioscience NU405L, 10 mM)

Seed Mixture:

1. Combine 13 μL PEM 104, 2.2 μL 10 mM GMPCPP, and 2.2 μL DMSO; vortex.
2. Add 4 μL 10 mg/mL non-labeled tubulin.
3. Add 1 μL 10 mg/mL rhodamine-labeled tubulin.
4. Place solution in water bath at 37°C for 40 minutes.

Elongation Mixture (10x dimmer):

1. Combine 13 μL PEM 104, 2.2 μL 10 mM GTP, and 2.2 μL DMSO; vortex.
2. Add 1 μL 10 mg/mL non-labeled tubulin.
3. Add 1 μL 1 mg/mL rhodamine-labeled tubulin.
4. Place elongation mixture in water bath at 37°C for 1 minute (seed will depolymerize at low temperature).
5. Add 1 μL of seed mixture to the elongation mixture.
6. Incubate seed/elongation mixture at 37°C in water bath for 1 hour.
7. Add 2 μL room temperature STAB solution without GTP to polarity-marked MTs.
8. Store at room temperature.

A.5 Kinesin Optical Trap Motility Assay

This protocol uses static microtubules (Taxol stabilized) polymerized with non-labeled tubulin for kinesin motility. His-tagged kinesin is linked to 0.44 μm diameter streptavidin-coated polystyrene beads using biotinylated penta His antibody. Poly-l-lysine surface is used in this protocol but biotin-BSA as well as biotin-PEG will work.

Materials:

Biotinylated penta-His antibody (Qiagen, 34440, 125 μL , 0.2 mg/mL)

Streptavidin coated polystyrene bead (Spherotech, SVP-05-10, 0.44 μm in diameter, 1% w/v) (Calculating molarity for beads: bead density (1.05 g/cm³). The mass of a single bead, 0.44 μm in diameter is 4.68×10^{-14} g, 1% w/v = 10 mg/mL = 10 g/L = 356 pM)

PEM80

PBS

Casein (10 mg/mL, Blotting Grade Blocker, Biorad)

DTT (0.5 M in 10 mM K-acetate)

Taxol (10 mM in DMSO)

Poly-l-lysine

ATP (100 mM in PEM80)

Centrifuge

Sonicator

1. (If streptavidin-coated beads are not ready) Wash streptavidin-coated beads
 - (a) Dilute 20 μL 0.44 μm streptavidin-coated beads into 80 μL PBS
 - (b) Wash 4 times at 10,000 rpm for 6 minutes, reconstituting in 100 μL PBS
 - (c) Sonicate for 2 minutes at 40%
 - (d) Store washed beads on a rotator at 4°C
 2. Make bead coated with biotinylated penta His antibody
 - (a) Take 20 μL of cleaned beads and add 50 μL PBS and 30 μL 0.2 mg/mL biotinylated penta His antibody
 - (b) Incubate at 4°C for 1 hour on a rotator
 - (c) Add 100 μL of PBS and wash anti-His beads 4 times for 6 minutes at 10,000 rpm, reconstituting in 100 μL PBS. For last wash, reconstitute in 100 μL assay buffer (AB).
 - (d) Sonicate for 2 minutes at 30%
- *For WT kinesin-1 assay, steps 1 and 2 are not needed as streptavidin beads will be used.
3. Make PemTax (PTX) by mixing

- (a) 500 μL PEM80
 - (b) 1 μL 10 mM Taxol
 - (c) Store on ice
4. Make Assay Buffer (AB) by mixing
- (a) 1329 μL PEM80
 - (b) 3 μL DTT
 - (c) 3 μL Taxol
 - (d) 15 μL ATP
 - (e) 30 μL 10 mg/mL casein
 - (f) Final concentrations: 1 mM DTT, 20 μM Taxol, 1 mg/mL casein, 1 mM ATP
 - (g) Store on ice
5. Make C-Tax (CTX) by mixing
- (a) 72 μL PTX
 - (b) 8 μL 10 mg/mL casein
 - (c) Store on ice
6. Make kinesin dilutions
- (a) K/100: 1 μL K into 99 μL AB
 - (b) K/1000: 10 μL K/100 into 90 μL AB
 - (c) K/5000: 20 μL K/1000 into 80 μL AB
 - (d) Before adding motor to the final dilution step, add 1 μL anti-His beads from stock to the 80 μL AB and sonicate for 2 minutes at 30%. Then, add the 20 μL K/1000 so that the motor is not damaged.
 - (e) Add oxygen scavenging reagents, 1 μL each of glucose oxidase, β -D-glucose, and catalase
 - (f) Incubate bead/kinesin dilution for 1 hour under rotation at 4°C
- *For WT kinesin-1 assay,
- (a) Dilute 1 μm streptavidin beads 3 μL of stock into 57 μL AB and then take 5 μL of that dilution into 75 μL of AB
 - (b) Sonicate for 2 minutes at 40%
 - (c) Mix 20 μL kinesin dilution and 20 μL bead dilution
 - (d) Incubate for at least 1 hour on rotator at 4°C
7. Prepare poly-l-lysine coated coverslips

- (a) Dilute 100 μL poly-l-lysine into 30 mL ethanol in a 50 mL Falcon tube
 - (b) Place two KOH cleaned coverslips into the solution and let sit for at least 15 minutes
 - (c) Dry slides with air line before use
8. Prepare flow channels from KOH etched slides
- (a) Start warming PTX, CTX, and AB to room temperature
 - (b) Flow in 20 μL MT diluted 100-200 times in PTX and let bind for 10 minutes
 - (c) Wash in 20 μL PTX
 - (d) Wash in 20 μL CTX and let incubate for 5 minutes
 - (e) Wash in 50 μL PTX
 - (f) Wash in 80 μL AB
 - (g) Add 20 μL kinesin/bead dilution

A.6 Kinesin Bundle Assay for Optical Trap

This assay allows one to measure force generation by motors in MT bundles. It utilizes polarity-marked MTs, biotin seed MTs, and streptavidin beads to assemble a MT “sandwich” with motors in between them.

Materials:

1.25 μm streptavidin beads

Biotin seed MTs (biotin seed, non-labeled elongation)

Polarity-marked MTs (bright seed, dim elongation)

PTX

CTX (1 mg/mL blotting-grade blocker ? casein)

Assay buffer

FL Kif15 or other motor of interest (Note: Kif15 is a poor MT bundler and will yield fewer bundles per slide than Eg5 or HSET.)

1. Dilute rhodamine polarity MTs 200-250x into room temperature PTX (dil pMTs)
2. Assemble flow cell with poly-l-lysine slide
3. Add 20 μL of dil pMTs and allow to incubate for 10 minutes
4. Wash in 20 μL PTX
5. Add 20 μL CTX and allow to incubate for 5 minutes
6. Wash in 20 μL PTX
7. Wash in 80 μL AB
8. Add motor/MT combination
 - (a) During a previous incubation, make epp tubes for the serial dilution of the motor filled with the appropriate amount of AB
 - (b) Before adding the motor to the last tube of the serial dilution, add 1 μL of cleaned streptavidin beads and sonicate for 2 minutes at 40%
 - (c) In the final dilution tube, add 1 μL each of glucose oxidase, β -D-glucose, and catalase, 1 μL biotin seed MTs (made the same way as polarity-marked MTs, except the seed has biotinylated tubulin and the elongation is non-labeled), and the appropriate amount of motor for the correct dilution
 - (d) Add 20 μL of motor/MT/bead combination to the flow cell
9. During the assay, bead will only bind to minus end of the biotinylated MTs because of the seed. Use fluorescence to check the polarity of the bottom MT. From this, one can determine whether the bundle being measured is parallel or anti-parallel in orientation.

A.7 Microtubule Gliding Assay for Optical Trap

This assay allows one to measure force generation on a microtubule that is gliding on a motor coated surface.

Materials:

DI water
5X BRB80
MgCl₂ at 200 mM
ATP at 200 mM
Casein (blotting grade blocker) at 5 mg/mL
 β -mercaptoethanol, 50% (or 0.5 M DTT)
Catalase at 3.5 mg/mL
Glucose oxidase at 20 mg/mL
 β -D-glucose at 450 mg/mL
Wash buffer
10X OS mix
Flow cell buffer
Pluronic F-127 at 1 mg/mL
Biotinylated MTs
Streptavidin beads

1. Add 5 μ L of stock concentration biotinylated MTs to an epp tube along with 1 μ L cleaned streptavidin beads. Incubate under rotation at room temperature while the assay is prepared to facilitate binding of beads to MTs. (Note: Using stock concentration of MTs was necessary to see force generation from gliding for Kif15 and N700. However, MTs can be diluted for Eg5.)
2. Make a skinny flow cell (tape closer together than normal, holds \sim 5 μ L) using an unetched slide
3. Add 5 μ L undiluted motor to flow cell and incubate for 3 minutes
4. Wash in 60 μ L wash buffer
5. Add 20 μ L P127 and incubate for 1 minute
6. Wash in 60 μ L wash buffer
7. Dilute bead/MT solution appropriately with flow cell buffer (may have to adjust dilution depending on motor used)
8. Seal and load slide
9. Trap bead in solution, bring to surface, try to bind MTs, record force/displacement data

A.8 anti-DIG Functionalized Beads

This protocol is slightly adapted from a protocol developed by Marie Eve Aubin-Tam, a former post-doctoral researcher in the lab.

Materials:

MES buffer

Borate buffer

PBS (pH 7.4)

Carboxy polystyrene beads (1.09 μm)

anti-Dig antibody

BSA

Ethanolamine

Cup sonicator

Rotator

Microcentrifuge

1. Make MES (0.1 M with 0.01% tween-20, pH 4.5), borate (0.1 M, pH 8.5), and PBS (pH 7.4) buffers according to the recipes in section A.1.
2. Mix 100 μL of 1 μm carboxy polystyrene beads with 100 μL of MES buffer.
3. Spin down (9000 rpm for 4 minutes) and resuspend in 200 μL MES buffer (repeat 5x).
4. Sonicate using a cup sonicator for 2 minutes at 40%.
5. Add 200 μL of freshly made EDC solution 2% w/v (corresponds to 10 mg EDC in 500 μL MES buffer).
6. Incubate the bead mixture for 3 hours at room temperature on a rotator.
7. Spin down (9000 rpm for 4 minutes) and resuspend the bead mixture in 1 mL of borate buffer.
8. Spin down (9000 rpm for 4 minutes) and resuspend the bead mixture in 400 μL of borate buffer.
9. Sonicate using a cup sonicator for 2 minutes at 40%.
10. Add 80 μL of 200 $\mu\text{g mL}^{-1}$ anti-DIG and 24 μL of 5 mg mL^{-1} BSA in borate buffer (filtered).
11. Incubate the bead mixture on a rotator for 1 hour at room temperature and then overnight at 4°C.
12. Stop the reaction by adding 10 μL of 0.25 M ethanolamine (0.25 M solution of ethanolamine corresponds to 10 μL ethanolamine + 650 μL borate buffer).

13. Incubate and mix the bead mixture on a rotator for 30 minutes at 4°C.
14. Spin down the beads (9000 rpm for 4 minutes) and resuspend in 200 μL of 10 mg mL^{-1} BSA in PBS (filtered).
15. Sonicate the bead mixture in a cup sonicator for 1 minute at 25% with ice.
16. Store the beads at 4°C and rotating gently.

A.9 Conjugation of anti-His to Amine on DNA Linker

Efficiency of EDC-mediated coupling is increased in the presence of Sulfo-NHS.

Materials:

His tag antibody (GenScript, A00186-100)

EDC (Thermo Scientific)

Sulfo-NHS (Thermo Scientific)

Ethanolamine (Sigma)

Biotin-1010 base pairs-NH₂ DNA

PBS

Bio-Rad Micro Bio-Spin 30 columns (MBS 30)

Cup sonicator

Rotator

Microcentrifuge

1. Take 80 μ L of anti-His (1 mg/mL)
 - (a) For 1 mg/mL, add 0.1 mL PBS to 100 μ g 0.5 mg/mL anti-His
2. Add 10 μ L EDC (40 mM)
 - (a) For 40 mM EDC, 0.153 mg EDC in 20 μ L PBS
3. Add 10 μ L Sulfo-NHS (100 μ M)
 - (a) For 100 μ M Sulfo-NHS, 0.0217 mg in 1000 μ L PBS
4. Gently vortex reaction mixture until all of the reagent is soluble
5. Allow activation reaction to proceed at room temperature under rotation for 30 minutes
6. Add 100 μ L amine-DNA
7. Rotate for 3 hours
8. Quench the conjugation reaction by adding 10 μ L of 0.25 M ethanolamine
 - (a) For 0.25 M ethanolamine, 10 μ L ethanolamine in 650 μ L PBS
9. Purify with MBS 30 columns
 - (a) Buffer exchange the column
 - i. Invert the column sharply several times to resuspend the settled gel and remove any bubbles.
 - ii. Snap off the tip and place the column in a 2.0 mL microcentrifuge tube (included).

- iii. Remove the top cap. If the column does not begin to flow, push the cap back on the column and then remove it again to start the flow. Allow the excess packing buffer to drain by gravity to the top of the gel bed (about two minutes).
 - iv. Discard the drained buffer then place the column back into the 2.0 mL tube.
 - v. Centrifuge for 2 minutes in a microcentrifuge at 1000 x g to remove the remaining packing buffer. Discard the buffer.
 - vi. Apply the new buffer in 500 μL aliquots. After each application of new buffer, let the buffer drain out by gravity, or centrifuge the column for 1 minute to remove the buffer.
 - vii. Discard buffer from collection tube. Repeat as required. Three washes result in greater than 99% of the buffer exchanged. Four washes result in greater than 99.9% of buffer exchanged.
 - viii. Sample can now be applied to the column.
- (b) Apply sample to column
- i. Place the column in a clean 1.5 or 2.0 mL microcentrifuge tube. Carefully apply the sample (20-75 μL) directly to the center of the column. Application of more or less than the recommended sample volume may decrease column performance.
 - ii. After loading sample, centrifuge the column for 4 minutes at 1000 x g.
 - iii. Following centrifugation, the purified sample is now in the exchanged buffer. Molecules smaller than the column's exclusion limit will be retained by the column. (Bio-Gel P-30 gel: 20 base pairs or 40 kDa)

A.10 Amyloid Fiber Preparation

This protocol forms amyloid fibers from NM monomers and amyloid fiber seeds. Strong Ψ seeds will yield fibers that are mechanically less strong than weak Ψ seeds. Seeds and monomers were provided by Bill Hesse from Susan Lindquist's lab.

Materials:

6 M GdnHCl (0.573 g/mL)

CRBB buffer

5 mM TCEP-HCl (0.713 mg in 497.5 μ L)

NM stock

Seed stock

Nanodrop

Rotator

Microcentrifuge

1. Pellet NM (or Alexa555-NM) stock from the H₂O/methanol stock solution at bench top centrifuge at 13,000 rpm for 10 minutes.
2. Remove the supernatant completely and let the pellet stand at the bench top for 5-10 mins, allowing the methanol evaporation.
3. Re-dissolve and combine the pellet using 6M GdnHCl (usually using 10 μ L of GdnHCl for two aliquots of NM stock at 20 μ M).
4. Check the concentration of NM stock by O.D._{276 nm}. O.D._{276 nm} of 10 μ M NM = 0.29
5. Prepare NM fiber solution: 2.5 μ M, 0.5% seeds in 1xCRBB with 5 mM TCEP
 - (a) 2.5 μ L of NM seeds (2.5 μ M mature NM fibers, seeded by yeast cells lysates carrying pure prion elements, stored in -80°C)
 - (b) 497.5 μ L of 1xCRBB with 5 mM TCEP
 - (c) x μ L of NM GdnHCl stock to make final NM concentration at 2.5 μ M
x μ L of Alexa555-NM GdnHCl stock to make final NM concentration at 2.5 μ M

***** Add both NM GdnHCl stock to the side of the epp tube, but not directly into the solution*****

Example: 1.25×10^{-6} L (Note: alter this amount to make 2.5 μ M) $\times 1000 \times 10^{-6}$ mol/L (Note: this concentration determined from step 4) = 1.25×10^{-9} / (500×10^{-6} L + x amount) = 2.5 $\times 10^{-6}$ M

6. Briefly vortex the sample, wrap with Al foil and incubate at desired temperature for 1-2 days

- (a) Incubate at 4°C for strong Ψ (mechanically less strong)
- (b) Incubate at 37°C for weak Ψ (mechanically less strong)

A.11 Conjugation of NM monomer to SH-Core Shell Beads

According to Dong *et al.* (NSMB 2010), the N domain “is extremely rich in glutamine and asparagine residues and drives the protein into the prion amyloid”. This reaction crosslinks primary amines in the protein. There are many in the N domain which drives polymerization of the monomers into fibers. Taking up these primary amines in the reaction renders the monomer inactivated, and they will not form tethers with amyloids in a flow cell.

Therefore, this protocol links streptavidin to SH-CS via the SMCC reaction, and then, biotinylated-NM is incubated with the new STR-CS to form NM-CS beads. These beads (as well as normal STR beads incubated with biotinylated-NM) will form tethers with amyloid fibers in a flow cell. However, the forces exerted on the amyloids may exceed the STR-biotin non-covalent interaction force.

Materials:

NH₂-Streptavidin

Biotinylated-NM

DMSO

Sulfo-SMCC (Pierce 22622 in 2 mg sealed tubes)

PBS

Bio-Rad Micro Bio-Spin 6 columns (MBS 6)

1. To make maleimide-streptavidin:
 - (a) Dissolve 0.002 g of Sulfo-SMCC in 200 μ L DMSO
 - (b) Combine 100 μ L 0.5 mg/mL streptavidin in PBS with 2.5 μ L SMCC/DMSO
 - (c) Rotate at room temperature for 2 hours
 - (d) Clean the NM-SMCC mixture
 - i. Prepare 1 MBS 6 column by exchanging buffer to CRBB as described below
 - A. Invert/mix the MBS column, snap tip, and drain for 2 min into a 2 mL tube
 - B. Empty flow through, spin at 1000 g for 2 min and discard flow through
 - C. Load 500 μ L buffer, spin 1000 g for 1 min and discard flow through
 - D. Repeat buffer load and spin a total of 3 times
 - ii. Place sample on the column (70 μ L maximum)
 - iii. Spin column at 1000 g for 4 minutes, collect flow through
2. To bind maleimide-STR to SH-CS beads:
 - (a) Combine 30 μ L of maleimide-STR with 200 μ L SH-CS beads
 - (b) Incubate for at least 2 hours at RT, or overnight at 4°C
 - (c) Spin down beads, remove supernatant, and resuspend in CRBB to clarify the beads

- (d) Sonicate for 2 minutes at 40% and store on rotator at 4°C
3. To bind biotinylated-NM to STR-CS beads:
- (a) Combine 50 μL STR-CS beads with 1.5 μL biotinylated-NM (1119 μM , adjust accordingly depending on concentration)
 - (b) Incubate for 1 hour at 4°C

During the SMCC conjugation, there must not be any other primary amines present. This means any samples in a Tris buffer (TE) must undergo a buffer exchange. Best results have been obtained when samples originated in a non-NH₂ buffer.

A.12 Amyloid Pulling Assay for Optical Trap

This protocol is for pulling amyloid fibers attached to the surface and beads via monomer-fiber interactions, as adapted from Dong *et al.* (NSMB 2010) and Castro *et al.* (Biophys. J. 2011).

Materials:

6 M Gdn HCl
Nanodrop
NM monomer
CRBB
Casein
Pre-formed amyloid fibers
NM-CS beads

1. Construct a 15-20 μL flow cell with double stick tape and a glass coverslip (not etched).
2. Spin down a stock concentration of sortase labelled monomer and resuspend in 10 μL 6M Gdm-HCl.
3. Check concentration on Nanodrop A280. $E = 29000 \text{ M}^{-1}\text{cm}^{-1}$
4. Dilute concentrated sortase monomer to 0.1-0.5 μM in CRBB + 5mM TCEP. (We diluted 1,000,000x for an ending concentration of approximately 0.0015 μM)
5. Flow in 20 μL of the diluted monomer and incubate for 15 minutes.
6. Wash the flow cell with 50 μL of CRBB buffer.
7. Flow in 20 μL 5 mg/mL casein (blotting-grade blocker, BGB) and incubate for 40 minutes.
8. Wash the flow cell with 50 μL CRBB buffer.
9. Flow in 20 μL strong psi (mechanically weak) amyloid fibers and incubate for 15 minutes.
10. Wash the flow cell 3 times with 1mL CRBB buffer + 0.1 mg/mL BGB.
11. Flow in 20 μL 20-50x diluted core shell beads. (Dilution depends on the stock concentration of the core shell beads.) Incubate for 1 hour-overnight to allow for the beads to bind to the fibers. If overnight, place flow cell in humidity chamber inside 4°C refrigerator.

A.13 TiO₂ Core Shell Microsphere Synthesis

Materials:

Specimen/Environment jars 2 oz. (Fisherbrand, 02-912-309)

Titanium butoxide (Sigma, 244112-100G)

Ethylene glycol, anhydrous (Sigma, 324558-100ML)

Acetone, reagent grade

Ethanol, 200 proof

Tween 20

Lutensol (BASF, 50070655)

MPTES (Sigma, 175617)

APTES (Sigma, 741442-100ML)

Note: Ethanol used in these experiments is refrigerated, except when in the glovebox.

Preparation of Anatase Core Particles

1. **Day 1:** Chelate 0.46% (by weight) titanium butoxide solution (97%) by mixing ethylene glycol (EG) in a glovebox for 10 hours (overnight). Alternatively, create the mixture inside the glovebox and parafilm vigorously to mix overnight in open air. To make the mixture, combine 30 mL EG with 154 μ L TBT. These amounts should produce approximately 15-35 mg of cores.

*** We did the latter; we brought our own pipettes and pipette tips into the glovebox to make the mixture. We did not attach the pipette tips prior to purging them into the glovebox because the residual air in the pipette tip greatly altered the reaction. We wrapped the vial in parafilm and placed it on the stir plate to mix overnight. We also cut the recipe in half and only used 15 mL EG and 77 μ L TBT. We did this because we wanted to perfect the synthesis before making huge batches in hopes that we do not waste the reagents.

2. **Day 2:** Dissolve 226.7 μ L Tween 20 [2.03mM] in 100 mL acetone (reagent grade) with rigorous stirring for 10 minutes. Add 100 μ L of DI H₂O. The amount of water is crucial for the spherical shape of the cores.
3. Mix 19 mL TBT solution with the 100 mL acetone solution. (To use the full 30 mL we can scale up step 2 to 158 mL of the acetone solution with 158 μ L DI H₂O and 358.2 μ L Tween 20.) The amount of TBT solution added affects the size of the cores (19 mL will produce \sim 500 nm cores).
4. Stir the TBT/acetone solution for 10 minutes on the stir plate. Remove the stir bar and leave for 24 hours. The relatively transparent solution will turn into a milky white solution and form a precipitate on the bottom.

*** Because we cut the TBT solution in half, we also had to cut the acetone solution in half. We only added 8.5 mL of TBT to the acetone to try to get the core size

smaller. When using 9.5 mL (half of 19), the core size was 13 pixels. The desired size is 8-9 pixels. When we decreased the amount of TBT to 8.5 mL the core size was 9 pixels, so we continued to use 8.5 mL throughout each core synthesis.

5. **Day 3:** Clean the white precipitate by centrifugation at 7000 rpm for 5 minutes, and then redisperse in ethanol. Wash the mixture twice. (During these washes, reduce the resuspension volume to make heating easier. I.E. resuspend the 100 mL acetone solution mixture in 10-15 mL ethanol and transfer to 1.7 mL tubes.)
6. Dry the precipitate in the convection oven at 70°C for 30 minutes. Having the precipitate in a microtube during drying makes transfer to the heating vessel significantly easier.
7. Transfer dried precipitate to foil and anneal particles for 1 hour at 500°C in a furnace. The furnace takes approximately 40 minutes to heat up.

*** We then suspended a tiny bit of the cores in ethanol, sonicated and sized the cores. They were anywhere from 9-16 pixels.

8. Transfer dried core particles to a microtube for storage.

*** We reduced the 50 mL acetone solution so that the precipitate was in only one microtube. Drying and retrieving the cores was much easier with it only in one container.

NOTE: Changing TBT concentration will affect core size. (19 mL - 500 nm; 19.5 mL - 550 nm)

Addition of Amorphous Titania Shells

1. Prepare 1 mL of 0.1M Lutensol ON60 solution by adding 41.8 μ L Lutensol to 1 mL DI H₂O.
2. Take 0.5 mg cores and disperse them in 1 mL ethanol and sonicate at 80% for 2 minutes. Now add this 1 mL core dispersion to 2.3 mL ethanol to make a 3.3 mL total dispersion.
3. Add 26.6 μ L 0.1M Lutensol solution to the 3.3 mL core dispersion and vortex the solution.
4. In the glovebox in a different vial, take 3.3 mL ethanol and add (50-175) μ L TBT. The amount of TBT is vital in the sizing of core-shell particles post-mixing. 100 μ L TBT produces \sim 1350 nm core shells. The reaction is quite sensitive to small changes in TBT amounts so be sure to measure accurately. Close the vial prior to removing it from the glovebox.
5. Outside the glovebox, add the core dispersion to the TBT solution and close immediately. Parafilm vigorously.

6. Add the vial to the sonication bath and sonicate for 2 hours.

*** We added 100 μL of TBT in the core shell addition. We added ice every 15-20 minutes depending on how warm the water got while sonicating. We also removed water as the ice melted and the water level rose above the lip of the jar. We also replaced the parafilm if it began to tear while sonicating. We brought our own pipettes and pipette tips into the glovebox once again.

NOTE: The specimen jar should be tightly parafilmmed and the level of water in the sonication bath should not exceed the lip of the jar. The react is very sensitive to unwanted water. Also, be sure to monitor the temperature of the sonication bath. Keep an ice bucket nearby and add ice so that the temperature of the bath is lukewarm. Too high or too low water temperatures have negative effects on the core shells.

OPTIONAL: Add 80 μL of a 1:100 dilution of MPTES in ethanol to the reaction mixture at the one hour sonication mark to functionalize the core shells. MPTES in ethanol should be prepared in the glovebox as MPTES is hypersensitive to moisture. MPTES adds thiols to the core shells. APTES, with the same dilution, adds amines to the core shells.

7. Collect the core shell particles by centrifuging for 5 minutes at 1500 rcf. Redisperse in the same amount of ethanol. Wash three times. After the final wash, resuspend in half the amount of ethanol. This halving is important as the heating step data was collected with these concentrations. Be sure to sonicate the core shell particles at 40% for 2 minutes prior to storage and prior to any use.

*** Each time we filled four 1.7 mL microtubes after the sonication step and after each wash step. We were left with 4 half full microtubes for usage.

*** If the cores looked okay after the first half of day 3 but the shell addition looks clumpy, non-spherical, etc., it is likely that something in the glovebox is contaminated, such as the ethanol. If necessary, bring in your own bottle of anhydrous ethanol and mark "For Lang lab use only". After doing this, the CS should form nicely.

Heat Tuning of Core Shell Particles

1. Distribute the desired amount of core shell particles as 100 μL aliquots in tubes.
2. Spin down particles at 1500 rcf for 5 minutes. Then resuspend in about 10 μL ethanol. Sonicate for 2 minutes at 40%, and then spin down in the mini centrifuge for a couple of seconds and remove the supernatant.
3. Heat these particles on the heating block at 50°C for 5-30 minutes. After 30 minutes, most particles become untrappable. As a general model, particle size shrinks 20-25%

with 30 minutes of heating. Resuspend these particles in 100 μ L ethanol. Sonicate before storage.

*** We found that heating between 7-15 minutes was most successful in terms of stiffness and shape. We found that the smaller the cores the less time the core shells needed to be heated. For example, the 9 pixel cores were heated 7-8.5 minutes, while the 16 pixel cores heated for 15 minutes. The final sizes were between 19-23 pixels with stiffnesses of over 0.3 pN/nm (3x that of the streptavidin beads).

NOTE: Sonicating is crucial, as the core shells clump easily. Be sure to dilute the core shells when using them in assays so that the flow chamber is not over-crowded.

A.14 Biotinylated Actin Filaments

This protocol is modified from the dissertation of Sonia Brady (Vanderbilt, 2017) to produce actin filaments that are biotinylated.

Materials:

Actin

Biotinylated Actin

GAB buffer

APB buffer

Phalloidin

Deionized water

Ice

1. Reconstitute actin by adding 100 μL of deionized water to 1 mg vial of lyophilized actin. Mix well by pipetting up and down. Aliquot into 5 μL samples. Keep the vials to used and snap freeze the rest. The solution will have a concentration of actin of 10 mg/mL (232 μM), 5 mM Tris-HCl (pH 8.0), 0.2 mM NaATP, 0.2 mM CaCl_2 , 5% sucrose, and 1% dextran.
2. Reconstitute biotinylated actin by adding 20 μL of deionized water. Aliquot into 5 μL samples. Keep the vials to be used and flash freeze the rest. The final concentration is 1 mg/mL of biotinylated actin.
3. Thaw one vial of 10 mg/mL pure actin and 1 vial of 1 mg/mL biotinylated actin.
4. Prepare fresh GAB buffer (A.1).
5. Mix the two vials and label the mixture ABA. The ratio is 10:1 (actin:biotinylated actin) with a total actin concentration of 5.5 mg/mL (127.6 μM).
6. Add 100 μL GAB and mix well by gently pipetting up and down. Place on ice for 1 hour. The solution is 110 μL with an actin concentration of 0.5 mg/mL (11.6 μM).
7. Prepare fresh APB (A.1).
8. Polymerize actin by adding 11 μL of APB to the actin solution. Mix well by pipetting up and down in a gentle fashion. Place on ice for 20 minutes. The actin concentration is now 0.435 mg/mL (10 μM).
9. Add 5 μL phalloidin (stabilizes the actin filaments). Leave on ice in the dark for 1 hour. F-actin is stable in the dark for at least one week at 4°C.

Note: If further dilution of actin is required, mix 5 μL of polymerized actin (10 μM) with 495 μL of GAB/APB solution (10 GAB:1 APB). The final actin concentration will then be 4.35 $\mu\text{g/mL}$ (0.1 μM).

A.15 Actin Rupture Assay

This protocol is used to rupture single actin filaments using core-shell beads.

Materials:

Biotinylated actin

1.25 μm streptavidin beads

Casein

GAB buffer

APB buffer

Streptavidin coated core-shell beads

1. Dilute 1.25 μm streptavidin beads in 10:1 GAB/APB buffer (0.5 μL in 100 μL buffer). Wash by spinning down at 10,000 rpm for 4 minutes. Reconstitute in 100 μL buffer. Sonicate at 40% for 2 minutes.
2. Add diluted beads to a flow cell constructed with an etched coverslip. Incubate for 10 minutes to allow beads to become stuck.
3. Add 20 μL of 10 mg/mL casein in 10:1 GAB/APB buffer and incubate for 10 minutes to prevent non-specific binding of core-shell beads.
4. Dilute biotinylated actin 1:100 in GAB/APB buffer, and add to flow cell. Incubate 10 minutes.
5. Dilute streptavidin-coated core-shell beads in GAB/APB buffer. Sonicate at 40% for 2 minutes. Add to flow cell and incubate 10 min.
6. When on the microscope, look for self-associated tethers or form tethers actively by fishing with trapped core-shell beads near surface bound polystyrene streptavidin beads.
7. Upon tether formation, translate the piezostage in 200 nm increments at 2 $\mu\text{m}/\text{sec}$ until the tether becomes fully elongated. Look for single ruptures with a clean break to baseline.